Tomographic imaging of East African equatorial ionosphere and study of equatorial plasma bubbles

A thesis submitted in fulfilment of the
requirements for the degree of

DOCTOR OF PHILOSOPHY

of

RHODES UNIVERSITY

by

Nigussie Mezgebe Giday

7 December 2017

Abstract

In spite of the fact that the African ionospheric equatorial region has the largest ground footprint along the geomagnetic equator, it has not been well studied due to the absence of adequate ground-based instruments. This thesis presents research on both tomographic imaging of the African equatorial ionosphere and the study of the ionospheric irregularities/equatorial plasma bubbles (EPBs) under varying geomagnetic conditions. The Multi-Instrument Data Analysis System (MIDAS), an inversion algorithm, was investigated for its validity and ability as a tool to reconstruct multi-scaled ionospheric structures for different geomagnetic conditions. This was done for the narrow East African longitude sector with data from the available ground Global Positioning System (GPS) receivers. The MIDAS results were compared to the results of two models, namely the IRI and GIM. MIDAS results compared more favourably with the observation vertical total electron content (VTEC), with a computed maximum correlation coefficient (r) of 0.99 and minimum root-mean-square error (RMSE) of 2.91 TECU, than did the results of the IRI-2012 and GIM models with maximum r of 0.93 and 0.99, and minimum RMSE of 13.03 TECU and 6.52 TECU, respectively, over all the test stations and validation days. The ability of MIDAS to reconstruct storm-time TEC was also compared with the results produced by the use of a Artificial Neural Network (ANN) for the African low- and mid-latitude regions. In terms of latitude, on average, MIDAS performed 13.44 % better than ANN in the African mid-latitudes, while MIDAS under performed in low-latitudes. This thesis also reports on the effects of moderate geomagnetic conditions on the evolution of EPBs and/or ionospheric irregularities during their season of occurrence using data from (or measurements by) space- and ground-based instruments for the east African equatorial sector. The study showed that the strength of daytime equatorial electrojet (EEJ), the steepness of the TEC peak-to-trough gradient and/or the meridional/transequatorial thermospheric winds sometimes have collective/interwoven effects, while at other times one mechanism dominates. In summary, this research offered tomographic results that outperform the results of the commonly used ("standard") global models (i.e. IRI and GIM) for a longitude sector of importance to space weather, which has not been adequately studied due to a lack of sufficient instrumentation.

Publications from this thesis

The work submitted for this thesis has been published in international peer-reviewed journal.

Giday, N. M. and Katamzi-Joseph, Z. T.: Performance of MIDAS over East African longitude sector: Case study during 04-14 March 2012 quiet to disturbed geomagnetic conditions, Space Weather, doi:10.1002/2017sw001732, 2018. This paper investigated the ability and validity of the MIDAS algorithm over the region of study and the optimization procedures and methods are presented in Chapter 4 while the results based on the optimized algorithm form most part of Chapter 5.

Chapter 6 of this thesis is based on the work under review: Uwamahoro, J. C., Giday, N. M., Habarulema, J. B., and Katamzi-Joseph, Z. T.: Reconstruction of storm-time total electron content using ionospheric tomography and artificial neural networks; A comparative study over the African region., Radio Science, under review, 2017.

Acknowledgements

Firstly, I would like to express my appreciation to my supervisor Dr Zama Katamzi-Joseph for her invaluable support and contribution to this research. I would also like to thank Dr Lee-Anne, SANSA Space Science Directorate, Managing Director, for the support and care during my study.

My gratitude goes to the South African National Space Agency (SANSA) Space Science Directorate for the use of their academic facilities financial support throughout the programme. MIDAS is a property of the Invert group at the University of Bath, so I would like to give recognition for their input.

My heartfelt appreciation goes to my colleagues (Tshimangadzo Matamba, Uwamahoro Jean Claud, Tsige Atilaw, Micheal Heyns, Makhosi Dubazende, Nicola Orford, Amore and others) for making my stay at SANSA Space Science both very joyful and memorable. The time we spent together including the Soccer games will be memorable. I also thank the SANSA Space Science staff for their support and kindness throughout the study. I Special thanks goes to Juchelle Ontong for her assistance and going an extra mile to help us celebrate "Ethiopian New Year" (at work place!).

Last but not least, my sincere thanks and gratitude goes to my siblings (Gezhagn, Abeba, Azeb, Sindayo, Birhan, Netsanet, Mahlet and Kibrom), parents, 'Ato' Mezgebe Giday and Mebrat Redda and my uncle Tsegay Redda for the love and support you cherished me throughout the study. Thank you all.

Table of Contents

List of Figures

List of Tables

Chapter 1

Introduction

The ionosphere is a weakly-ionized plasma that exists at altitudes between about fifty and a thousand kilometers above the surface of the Earth. This plasma is mainly influenced by the Earth's atmosphere, the geomagnetic field and solar radiation. Depending on the governing mechanisms and levels of interaction with and penetration of solar particles of the ionosphere, the Earth's ionosphere is usually classified as polar/high-latitude, mid-latitude and low-latitude/equatorial. The plasma at high latitudes is influenced by the solar wind, i.e. the outflow of plasma from the Sun's surface into interplanetary space, and the interplanetary magnetic field. The structure of the mid-latitude ionosphere arises mainly from the ionisation of atmospheric gases by ultraviolet solar radiation, whereas the dynamic state of the ionosphere at low latitudes is predominantly controlled by electric fields originating from the dynamo action by atmospheric waves propagating from below, and the solar wind-magnetosphere interaction from above. The vertical profile of ionisation depends on the density of the neutral atmosphere and the intensity of solar radiation. It maximizes at the F-region peak, usually at an altitude of between 200 and 400 km. This will be discussed in Chapter 2.

The Earth's ionosphere has an intrinsic relationship with radio communication. This is because the free electrons in the plasma have an influence on the propagation of high-frequency (HF) electromagnetic waves. The ionosphere reduces the speed of signals passing through it by a frequency-dependent amount, i.e. the electromagnetic radio signals experience time delay (modulated codes) and advance (carrier phase) as they propagate through the ionosphere. This means a dual-frequency ground-based Global Navigation Satellite Systems (GNSS) receiver can measure the density of electrons between it and a satellite, as the delay is directly proportional to the integral number of electrons in a unit cross-sectional area along the signal path (usually referred to as total electron content, TEC), and inversely proportional to the square of the frequency of propagation (Hofmann-Wellenhof et al., 1997; Misra and Enge, 2006).

The effect of the ionosphere on satellite communication has provided both a means of probing the ionosphere and an additional motivation for doing so. Multiple techniques are used to characterize and study the ionosphere parameters during geomagnetically quiet and disturbed periods (disturbed period classified by Dst $<$ -30 nT, Loewe and Prölss (1997)) both on regional and global scales. The International Reference Ionosphere (IRI) model (Bilitza et al., 2011) is a widely used empirical global model for prediction of plasma parameters of the Earth's ionosphere. However, the model's accuracy deteriorates for regions where no or little ionospheric data is contributed to the model data base, such as Africa (Bilitza and Reinisch, 2008; Bilitza et al., 2014; Ssessanga et al., 2015). Although, the African continent is the second largest land mass in the world, it is faced with a paucity of ionospheric data compared to the rest of the world. This hinders endeavors to nowcast and/or forecast space weather parameters that are essential for, but not limited to, the communication and navigation sectors. Despite the paucity in the data sources, efforts

to study the African ionosphere have been made by, among others, Habarulema et al. (2007); Ssessanga et al. (2015); Mungufeni et al. (2016).

Tomographic techniques have also brought new solutions. Ionospheric tomography is a technique for the reconstruction of the temporal and spatial variations of ionospheric electron density, based on TEC observations along a series of transmitter-receiver signal propagation paths in the inversion region, using Global Positioning Satellite (GPS) data (see e.g. Mitchell and Spencer, 2003; Fridman et al., 2009; Chartier et al., 2012). The feasibility of ionospheric imaging techniques has been studied by Chartier et al. (2014) for the African region, Cilliers et al. (2004); Katamzi (2008); Yao et al. (2013); Giday et al. (2015) for the South African ionosphere during both geomagnetically quiet and disturbed periods, respectively, and Kassa et al. (2015) for the East African sector.

The low- and equatorial latitude ionosphere is the most dynamic region. It is characterized by a steep density gradient as a result of the ionisation troughs and crests associated with the low and high electron densities, respectively, due to the fountain effect. Although, the ionosphere may be considered a continuous layer with a fairly smooth plasma density distribution, localized ionospheric structures may occur, with the equatorial ionisation anomaly being the largest of the ionospheric structures. The presence of such ionospheric density gradients and the addition of the electrodynamics which accompany sunsets, are known to cause the development of ionospheric electron density irregularities (McNamara, 1991; Ngwira et al., 2013b; Abdu, 2016). Such ionospheric irregularities are generated within large-scale depletions in the ambient electron density over the equatorial ionosphere and are commonly referred to as equatorial plasma bubbles (EPBs). Attempts to study ionospheric irregularities over the African region include, but are not limited to, Portillo

et al. (2008), Amabayo et al. (2015), Mungufeni et al. (2015) and Kassa and Damtie (2017). However, the presence of a non-uniform and highly dynamic ionosphere, due to the electrodynamics the low and equatorial latitudes, makes ionospheric imaging of multiscale-sized structures a challenge, especially when the region of study (e.g. Africa) is not sufficiently populated with ground instruments.

1.1 Problem description and motivation

The research presented in this thesis contains both tomographic imaging of the African equatorial ionosphere and the study of the ionospheric irregularities/EPBs under varying geomagnetic conditions. Since the availability of the data sources and measurements dictated the nature of the research undertaken, the diagnosis and experimentations made to achieve the final outputs are addressed as well. The reason behind the decision to apply MIDAS as an imaging technique to the larger part of the African ionosphere, was based on the promising results obtained by its implementation for reconstructing the South African ionosphere (Giday et al., 2015). A study by Chartier et al. (2014) conducted research of the African ionosphere, using a similar algorithm. Their work was aimed at determining how much GPS receiver coverage would suffice to accurately specify the ionosphere over Africa. To this effect, the authors used a simulation approach, simulating both fictional receivers and data from the IRI model, for the inversions. They demonstrated that the operational GPS receiver coverage at the time of the study was insufficient for specifying the horizontal/longitudinal structures over Africa.

The research in this thesis investigates the validity and capability of MIDAS over the narrow East African longitude sector using data from the available ground GPS

receivers. The number of the available GPS ground receivers and their spatial distribution on the African sector is too limited to investigate the full capability of MIDAS to image small-scale structures, in particular. However, during the process of optimization of the MIDAS algorithm, the experimentations conducted produced better imaging results over selected regions of well populated longitude sectors. The validity of the imaging results were gauged with independent global and regional models and independent per station observations. The ability to and challenges of imaging ionospheric structures of different scale sizes was investigated. In addition, the effects of geomagnetic storms on the evolution and electrodynamics of equatorial ionospheric structures and/or EPBs were also investigated, using data from multi-instrument measurements such as the Communication/Navigation Outage Forecasting System (C/NOFS) satellite and ground magnetometers.

1.2 Research aims

The work described in this thesis comprises the evaluation of the performance of the MIDAS inversion for the African ionosphere, with a focus on the East African sector, by comparing it with two existing global ionospheric models, and also the study of the effects of the geomagnetic storms on ionospheric irregularities and/or EPBs. The aims of the research are as follows:

- To assess the ability of the MIDAS algorithm to image ionospheric structures of different scale sizes during both quiet and disturbed conditions and compared against independent global ionospheric models and validated with independent observations.
- To investigate the effects of geomagnetic storms on the evolution of post-sunset EPBs and/or ionospheric irregularities, using ground- and space-based

instruments and to identify the mechanism(s) responsible for either inhibiting or generating the structures in the East African ionosphere.

1.3 Thesis structure

This thesis comprises 9 chapters. The first chapter offers a description of the problem and sets the research objectives.

Chapter 2 gives background theory of the ionosphere and its constituents. In addition, different ionospheric structures and the associated electrodynamics are discussed.

Chapter 3 provides details of the available data sources and instruments that were used. These include the methods that were used to obtain TEC values from GPS signals, in situ electron density measurements from the C/NOFS satellite and magnetometer measurements of the Earth's magnetic field.

Chapter 4 gives the background theory of ionospheric tomography, in general, and MIDAS reconstruction in particular. In addition, independent global ionospheric models such as the IRI model, the Global Ionospheric Map (GIM) and others that were used to compare MIDAS reconstructions, are described in this chapter. The derivation of the proxy for equatorial electrojet (EEJ) currents from pairs of magnetometers, and rate of change of TEC (ROT) and ROTI indices are also covered in this chapter.

Chapter 5 presents the results of MIDAS imaging of the the East African ionosphere. The MIDAS results, validations and comparisons are also discussed in this

chapter.

Chapter 6 presents the analysis of the ability of MIDAS to reconstruct the ionosphere during disturbed geomagnetic conditions, in comparison with independent storm-time TEC models (i.e. an artificial neural network (ANN)).

Chapter 7 addresses the challenges of imaging medium- to small-scale ionospheric structures by means of the MIDAS inversion.

Chapter 8 presents results of the study of the evolution of EPBs and ionospheric irregularities during moderate geomagnetic storms over the East African sector. This chapter also discusses the dynamics and competing mechanisms that play a role in this evolution.

Finally, in Chapter 9, conclusions are drawn and recommendations made on the possibility of improving imaging techniques to capture ionospheric structures over Africa.

Chapter 2

Theoretical background to the ionosphere

This chapter offers essential background information on the ionosphere's general formation, vertical structure and its variabilities. Background information on various ionospheric structures, with the emphasis on low-latitudes, is also presented in this chapter.

2.1 Introduction to the ionosphere

Understanding of the ionosphere has been related to radio communications since Marconi's transatlantic experiments in 1901. These experiments motivated Heaviside and Kennelly to suggest that the upper atmosphere could reflect radio signals and thus enable long-haul communications. Terms, such as "Heaviside layer" and "Appleton layer" were used before Watson-Watt proposed the term "ionosphere" in about 1926 (Rishbeth and Garriott, 1969).

The ionosphere owes its existence to the Sun, since it is created primarily by the

photoionisation of neutral particles in the upper atmosphere. Therefore, this region of the atmosphere exhibits different characteristics during day and night times. During the sunlit hours, the ultraviolet (UV) radiation breaks up gas molecules into positively charged ions and free electrons. Solar wind particles, X-rays and cosmic rays from the Sun can also strip electrons off the gas molecules in the upper atmosphere, regardless of the hour of day. The created plasma maintains its state of equilibrium via the recombination process, which dominates during the nighttime hours. Thus depending on the presence or absence of the Sun's radiation, the thickness and nature of dominant chemical processes within the ionosphere vary between day and night. Moreover, due to the combined effects of ionisation, recombination and an exponential increase in density of the neutral atmosphere with decreasing altitude, the ionosphere has a distinct vertical profile. The vertical profile is commonly divided into the plasmasphere, the topside ionosphere and the bottomside ionosphere, as depicted in Figure 2.1.

The plasmasphere is a region of the ionosphere where hydrogen ions (H^+) becomes the dominant ion species (Prolss, 2004; Sibanda, 2010). It marks its beginning at a point called the Upper Transitional Height (UTH), where the number of Oxygen ions and Hydrogen ions is approximately equal, as shown in Figure 2.1. The region below this transition height and above the peak electron density point is referred to as the topside ionosphere, while the bottomside ionosphere lies underneath the latter (McNamara, 1991).

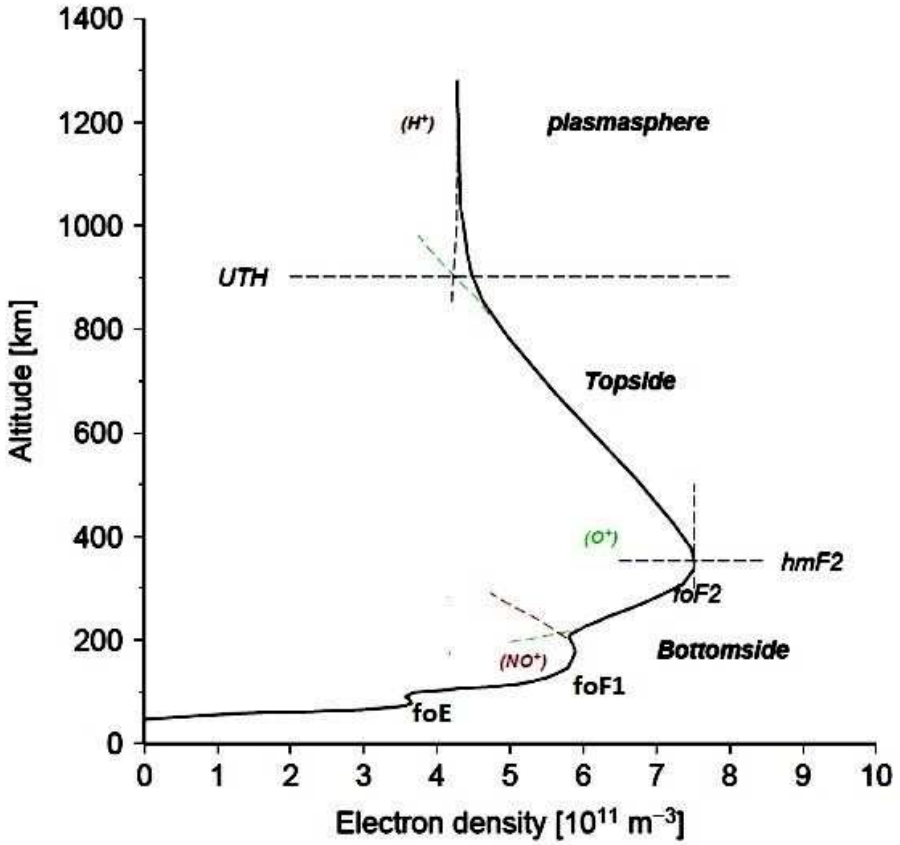

Figure 2.1: An illustration of a typical vertical ionosphere divided into three regions (i.e. E, F1 and F2 regions), along with the associated dominant species in each region. UTH is the upper transition height. The density profiles are not to scale. Source (Sibanda, 2010).

2.2 Ionospheric variations

The ionosphere is known to undergo long- and short-term variation. Since most of the ionosphere's variability is linked to the Sun, any change in the amount of radiation or the relative geometry between the Sun and Earth leads to diurnal, seasonal, solar cyclical, location (with respect to geomagnetic latitudes) and geomagnetic storm effect variation in the ionosphere. Furthermore, ionospheric variability can be broadly grouped into spatial (i.e. height and geomagnetic latitude) and temporal (i.e. diurnal, seasonal, solar cyclical and geomagnetic storm effects) variation.

2.2.1 Height

The bottomside ionosphere is subdivided into three major layers (D, E and F):

- **D layer:** This layer has an altitude range of $\sim$ 50 to $\sim$ 90 km, with less ionisation than in the E and F layers. Ionization is mostly due to X-rays and cosmic rays. It is mostly seen during the day and disappears during nighttime. The layer is weakly ionised, because the recombination rate is high, due to the high density of neutral species. The typical electron density of the D-layer is of the order of 10^9 electrons/m^3. More details can be found in Rishbeth and Garriott (1969); Davies (1990) and Moldwin (2008).
- **E layer:** The E layer falls within the altitude range of $\sim$ 90 to $\sim$ 120 km. A major source of ionization is soft X-rays. The typical E-region peak electron density is of the order of 10^{11} electrons/m^3 (Selcher, 2007; Moeketsi, 2008), relatively higher than in the D layer. A cloud of electrons a few kilometers thick and a few hundred kilometers across appears and disappears sporadically at E region altitudes, hence, called sporadic E (Es) (McNamara, 1991; Moldwin, 2008).

- **F layer:** The F layer is divided into the F1 and F2 layers during the daytime and the former disappears to form one F layer during the nighttime. It lies between altitudes of about 120 to altitudes of 400 km. The formation of the F layer is mainly due to the ionisation of oxygen atoms by solar extreme UV radiation. The F2 layer contains the highest electron density (in the order of 10^{12} electrons/m^3) within the ionosphere (McNamara, 1991; Baumjohann and Treumann, 1997). Much of the contribution to ionospheric TEC comes from this layer, since it contains the highest density free electrons compared to the other layers.

2.2.2 Latitudinal variation

The Earth's ionosphere is non-uniform, existing mainly on the Sun-illuminated side of the globe, thus displaying latitudinal variation. Over the equator the ionospheric density can be expected to be higher compared to other geographic locations, owing to the fact that the solar zenith angle is at its lowest. The incidence angle of UV radiation becomes more oblique with increase in latitude, and photo-production decreases towards the poles. With respect to the geomagnetic latitudes, the ionosphere can be characterised broadly into the low-latitude, mid-latitude and high-latitude ionospheres (Zolesi and Cander, 2014). The structures of the low and equatorial latitude ionosphere are the main focus of this research and are discussed in Section 2.4.

The high-latitude ionosphere is the region above $\sim$ 60 degrees in the northern and southern hemispheres (Hunsucker and Hargreaves, 2003; Kinrade, 2013). In general, the ionosphere is produced almost entirely from the extreme UV and X-ray radiation globally, but at high latitudes magnetospheric interaction plays a dominant role.

Due to the Earth's magnetic filed lines near vertical orientation, solar particles are trapped and accelerate downwards into the upper atmosphere. Precipitating energetic particles can penetrate a range of altitudes, adding free electron production via collisional reactions. Due to the complex nature of its production, loss and transport mechanisms, the high-latitude ionosphere can become the most dynamic and unpredictable structure of the ionosphere. However, the electron densities are considerably lower than in the lower latitudes, since the solar radiation strikes the atmosphere in this region at a more oblique angle (Sibanda, 2010).

The mid-latitude ionosphere shows the least variation, compared to the high and low latitude regions. However, according to Yizengaw (2004) seasonal anomalies and some short-term variations like the main ionospheric trough (MIT) driven by solar and geomagnetic storm inputs in the auroral ionosphere, occur in these regions. The mid-latitude ionosphere has been explored the most because most ionospheric observation instruments are located in this region. Thus, it is the best understood region (Hunsucker and Hargreaves, 2003; Kinrade, 2013; Zolesi and Cander, 2014).

The low-latitude ionosphere is host to some of the largest electron concentrations on Earth during the day. In fact, the ionospheric electron density should be at its maximum at the dayside equator during equinox, when the Sun is directly overhead and the ionisation rate is at its maximum, Kinrade (2013). Another phenomenon peculiar to this region is the fountain effect which redistributes electrons at the equator to latitudes of 10 to 20 degrees on both sides of the equator (McNamara, 1991). The equatorial and low-latitude ionosphere is characterised by small- to large-scale ionosphere structures. These include the equatorial ionization anomaly and equatorial plasma bubbles, as discussed in Sections 2.3 and 2.4.

2.2.3 Diurnal variation

The Sun's illumination on Earth varies over the 24-hour period due to Earth's rotation with respect to the Sun. Higher electron density is normally observed during the day due to photoionisation and lower electron density at night when recombination is higher (Davies, 1990). Figure 2.2 illustrates the variation between daytime and nighttime ionospheric profiles.

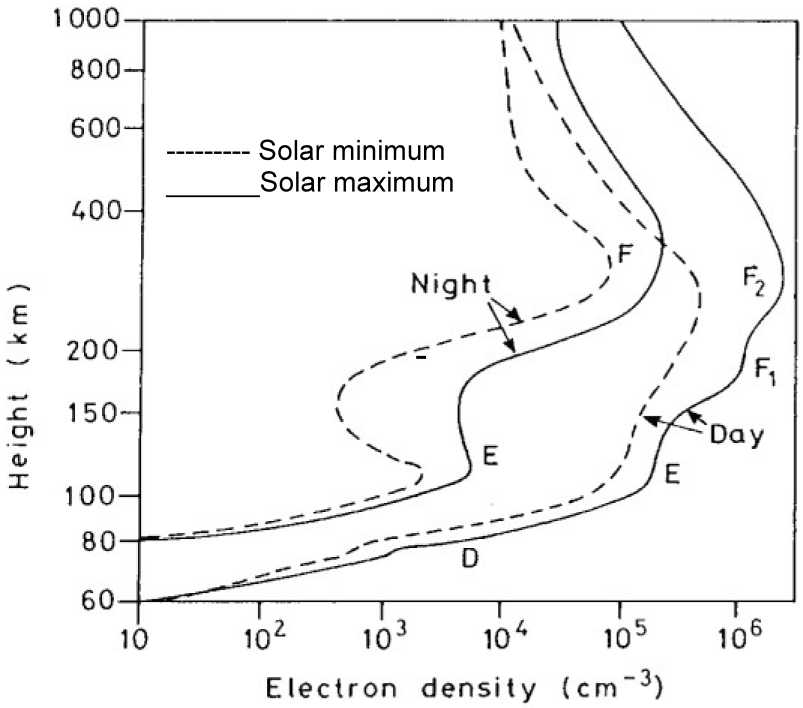

Figure 2.2: An example of the daytime and nighttime electron density profiles during different times of the solar cycle. Dashed lines indicate the profile during solar minimum and solid lines during solar maximum. (Source: Hunsucker and Hargreaves, 2003).

2.2.4 Seasonal variation

Seasonal variation of the ionosphere is related to the change in the solar zenith angle as a result of the Earth's movement around the Sun. The solar zenith angle (Z_A) is minimum when the Sun is overhead and produces maximum photoionisation. Since the zenith angle at noon is greater in winter than the corresponding angle in summer, the electron density concentration in the D, E and F1 layers are greater in the summer than in the winter season (Rishbeth and Garriott, 1969; McNamara, 1991). However, at middle latitudes the peak density of the F2 layer at noon is sometimes considerably larger in winter than in summer. This phenomenon is called the mid-latitude seasonal anomaly and occurs due to the seasonal changes in the neutral atmosphere, the composition of which also exhibits seasonal variation (Davies, 1990; McNamara, 1991) and due to transport mechanisms (Rishbeth and Garriott (1969)). Rishbeth and Müller-Wodarg (2006) also reported that the dynamical influences of the lower atmosphere (below about 30 km) are the most likely cause of the asymmetry of F2 layer. Moreover, the electron content is abnormally large at the equinoxes (in March and September), giving the semi-annual anomaly (Hargreaves, 1979).

2.2.5 Solar cycle variation

Sunspots are regions on the Sun's surface which have lower temperatures than their surroundings, hence appear as dark spots. Sunspot number is a measure of the number of sunspots and groups of sunspots. It is a direct indicator of the level of solar activity because it varies according to the progress in time of the 11-year solar cycle. The period during which the highest (lowest) number of sunspots are

observed on the Sun's surface corresponds to high (low) solar activity or solar maximum (minimum), as shown in Figure 2.3, Hargreaves (1979). Since space weather is predominantly driven by the Sun, higher ionospheric variability and an increase in the level of photoionisation due to the increased radiation, occur during periods of higher solar activity. Similarly, the ionosphere exhibits lower variability during periods of lower solar activity (McNamara, 1991), as illustrated in Figure 2.2. Moreover, solar disturbances are more frequent at solar maximum than solar minimum, and these disturbances generally initiate geomagnetic storms (Davies, 1990).

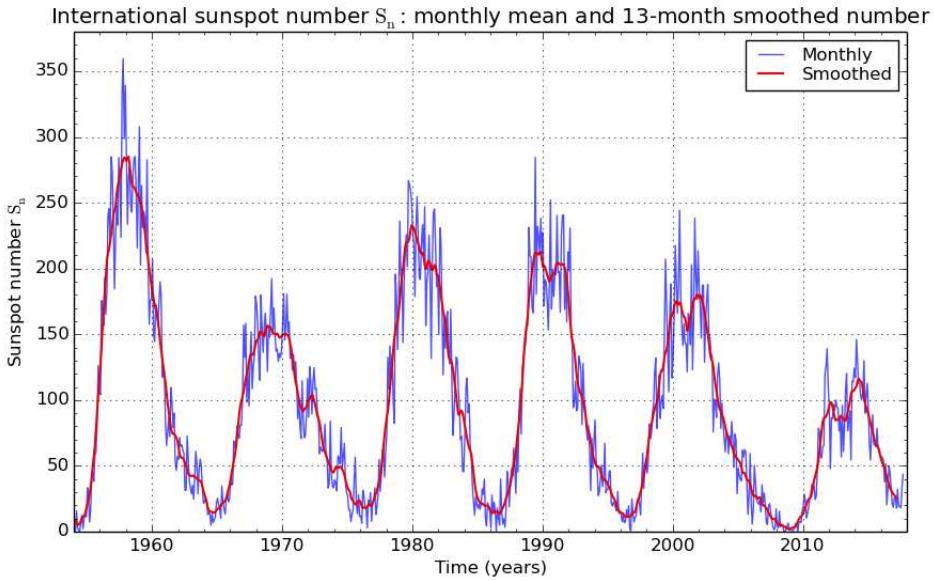

Figure 2.3: The monthly mean sunspot number (blue) and 13-month smoothed monthly sunspot number (red) for the last five solar cycles. Image courtesy http://sidc.oma.be./silso/monthlyssnplot.

2.2.6 Geomagnetic activity effects

Through the thermal convection at ionospheric heights due to the Sun's UV radiation, ions and electrons move across the geomagnetic field, thereby generating

ionospheric currents. These currents associated with magnetic perturbations in the ionosphere's environment, the variations of which are later detected as geomagnetic field fluctuations on the Earth's surface (Ondoh and Marubashi, 2001). The geomagnetic field variation varies according to local solar and lunar time and this variation is referred to as solar (Sq) and lunar (L) daily magnetic variation (see Rishbeth and Garriott, 1969). Another factor of geomagnetic activity is the occurrence of a geomagnetic storm, which is the result of the interaction between the solar wind and Earth's magnetic field.

The variation of the Sun's magnetic field approximates the 22-year solar cycle, and is characterised by a reversal of the magnetic polarity. This magnetic field is associated with a number of observable phenomena that occur on the solar surface such as sunspots, solar flares, coronal mass ejections (CMEs), coronal holes, prominences and filaments. When high speed solar winds, produced by CMEs or coronal holes, interact with the Earth's magnetic field at the Earth's magnetosphere, geomagnetic storms can be produced depending on the composition of the solar winds (Lopez et al., 2004). Part of the Sun's magnetic field, associated with the solar wind, is the interplanetary magnetic field (IMF), which travels outward in a spiral pattern due to the Sun's rotation, originating from regions of open magnetic field lines. The direction of the IMF, which is commonly described by Bx, By and Bz, is essential for the study of the coupling of the solar wind with the magnetosphere/ionosphere.

Campbell (2003) reported that, when the southward-directed IMF (i.e. -Bz) encounters the northward-directed geomagnetic field, the field lines interconnect, deforming the Earth's dipole field and allowing entry of the solar wind particles into the magnetosphere via a process called magnetic reconnection. The initiation of major magnetic disturbances on the Earth are associated with a southward Bz-component

(Campbell, 2003; Rosenqvist et al., 2005). Moreover, there is increased energy input into the magnetosphere during reconnection, which initialises the conditions for dynamic change within the magnetospheric current systems.

The occurrence of CMEs, i.e. abrupt discharges of plasma from the surface of the Sun into interplanetary space, is associated with solar magnetic field lines that open up into interplanetary space. Although the rate of CME occurrence increases with increasing solar activity, which tends to peak during solar maximum, it can take place at any time during the solar cycle (Campbell, 2003). Observation has revealed that Earth-directed CMEs that evolve into interplanetary CMEs are the major cause of intense geomagnetic storms (Richardson et al., 2000; Gopalswamy et al., 2005). However, not all Earth-directed CMEs are responsible for major geomagnetic storms.

Coronal holes are regions of abnormally low-density plasma where the magnetic field lines are of single polarity, all directed either inward or outward toward the interplanetary space. The hole is the source of fast solar wind streams which are abundant during the declining phase of the sunspot cycle Hargreaves (1979). The polarity of the magnetic fields within the stream remains the same as in the corresponding coronal hole while they co-rotate with the Sun for several rotations. Recurring geomagnetic storms are associated with the fast streams from coronal holes.

An electrodynamic process in which the electrically conducting atmosphere moves through the geomagnetic field and generates electric fields and currents is called the ionospheric wind dynamo (Richmond and Jungers, 1995). During disturbed conditions, wind generated by high-latitude Joule heating and ion-drag forcing alters the

dynamo electric fields and currents which disturbs the normal quiet time thermospheric circulation. The equatorward winds in relation to the high-latitude forcing turns westward at middle and low-latitudes with the action of Coriolis force (Rishbeth and Hanson, 1974; Yamazaki and Kosch, 2015). Equatorward currents driven by these westward winds build up positive charges near the equator, thus setting up poleward electric fields which drive Pedersen currents that balance the wind-driven equatorial currents. Another type of ionospheric current, called the Hall current, is produced by the poleward electric field. Hall currents cause positive charge build-up at the dusk terminator and negative charge accumulation at the dawn terminator. Thus, the effect of a disturbance dynamo at equatorial latitudes is manifested by the generation of a westward electric field on the dayside and an eastward electric field on the nightside. This is in opposition to the quiet time pattern.

Equatorial ionospheric electric fields and currents deviate significantly from their quiet day patterns during periods of elevated geomagnetic activity (Fejer, 2002; Abdu, 2012; Yamazaki and Kosch, 2015). Under geomagnetically disturbed conditions, the two main disturbance electric fields responsible for change in the plasma electromagnetic drifts and current perturbations are the prompt penetration electric fields and the ionospheric disturbance dynamo electric fields. While the prompt penetration electric fields are associated with the solar wind and magnetospheric convection (Fejer and Scherliess, 1997; Kelley, 2003), the ionospheric disturbance dynamo electric fields are due to the dynamic action of thermospheric winds produced by auroral heating (Blanc and Richmond, 1980). The interplanetary electric field (IEF) is believed to penetrate the low-latitude ionosphere during intense geomagnetic storms through under-shielding and/or over-shielding processes. During

the under-shielding process, i.e. related to a rapid and significant southward interplanetary magnetic field (IMF) variation, the dawn-to-dusk IEF penetrates the magnetosphere and strengthens the ionospheric zonal electric field (de Siqueira et al., 2011, and references therein). The over-shielding process, i.e. when the IMF Bz turns northward, results in eastward and westward electric fields in the nightside and dayside ionosphere, respectively.

2.3 Equatorial ionisation anomaly (EIA)

At the geomagnetic equator, the field lines are aligned horizontally in the north-south direction. In the E-region ionosphere, tidal winds drive currents during the daytime which, together with the magnetic field, cause the accumulation of positive and negative charges at the dawn and dusk terminators respectively. This conductivity gradient, results in a strong eastward electric field along the magnetic equator (Tarpley, 1970; Heelis, 2004; Alken and Maus, 2007). Thus, due to the combined effects of the electric and magnetic fields, electrons are carried aloft by electromagnetic drift ($\mathbf{E}\times\mathbf{B}$ force). However, constrained by the horizontal magnetic field lines, plasma diffuses down these lines due to pressure gradient and gravity (see Figure 2.4) and settles at about $\pm 15^{\circ}$ from the geomagnetic equator, adding to it large masses of electrons. These bands of enhanced electrons are commonly known as the equatorial ionisation anomaly (EIA) or Appleton anomaly (Hargreaves, 1979; McNamara, 1991; Yizengaw and Moldwin, 2009). The EIA region is connected to the equatorial ionosphere and the mid-latitudes due to their latitudinal locations, hence it is of importance in the study of ionospheric structures, including equatorial plasma bubbles (EPBs) (Yizengaw and Moldwin, 2009).

In relation to storm-time ionospheric perturbations, due to the prompt penetration electric field, equatorial electric fields can be enhanced either westward during the night or eastward during daytime, which subsequently leads to either suppression or enhancement of EIA peaks (Bagiya et al., 2011). Similarly, while the EIA can be well-developed during geomagnetically quiet days, it can be absent during disturbed conditions (Zolesi and Cander, 2014). The EIA can also be enhanced during storms, sometimes dramatically so (e.g. Mannucci et al., 2005).

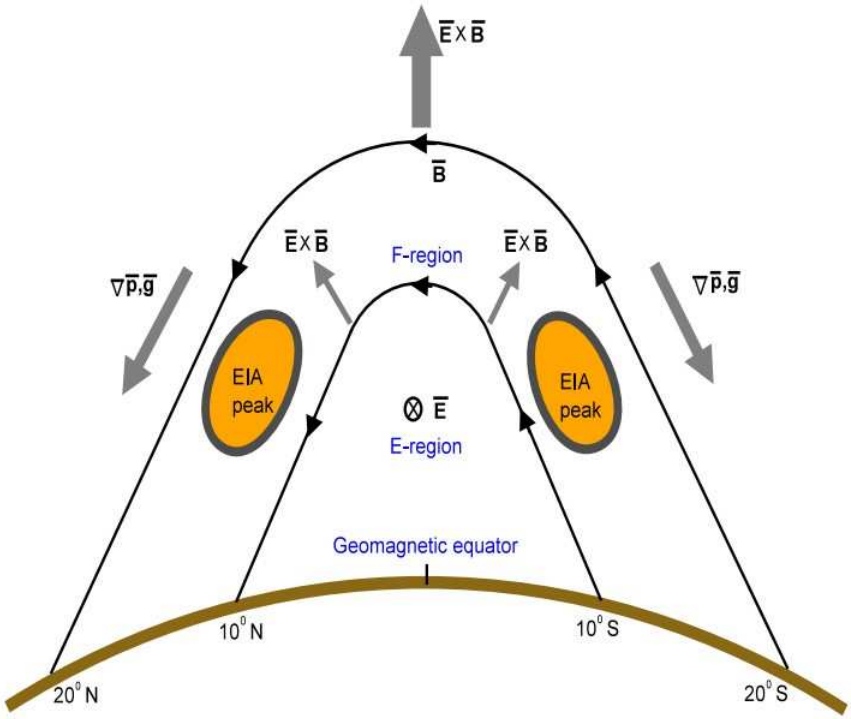

Figure 2.4: A schematic diagram illustrating the equatorial fountain effect and the development of EIA peaks (after Ngwira, 2012).

2.4 Equatorial irregularities

In the equatorial ionosphere, localised ionospheric structures can form which favour the development of ionospheric electron density irregularities (Basu et al., 1978, 1996; Ngwira et al., 2013b; Zolesi and Cander, 2014; Mungufeni et al., 2016). After sunset the plasma remains suspended along the horizontal field lines throughout the night. However, due to the low density of the neutral atmosphere at higher altitudes, the recombination process can be slow. Moreover, the daytime eastward E-region electric field intensifies near sunset. It is commonly called pre-reversal enhancement (PRE). Following the PRE after sunset, the F-layer plasma at the dip equator is uplifted to higher altitudes, while the plasma in the E-layer reduces due to the decreasing intensity of the solar radiation. As a result, a steep vertical plasma gradients is created between the depleted bottomside ionosphere and the higher density of the topside F-layer. Such a density gradient becomes unstable to density perturbations and leads to instability growth, known to be driven by the Rayleigh-Taylor (R-T) mechanism (McNamara, 1991; Fejer et al., 1999; Rezende et al., 2007; Abdu, 2012, and the references therein). These ionospheric perturbations which are generated within the large-scale depletions in the ambient electron density over the equatorial and low-latitude ionosphere, are commonly referred to as equatorial plasma bubbles (EPBs) (McNamara, 1991; Rezende et al., 2007). Studies showed that EPBs could extend to midlatitudes, for example Huang et al. (2007) reported observations of midlatitude plasma depletions during the 29 October 2003 storm which has reached magnetic latitudes of 46°S.

Under favorable ionospheric conditions, these bubbles also elongate along the magnetic field lines, and can move gradually to higher latitudes (Basu et al., 1981; Nishioka et al., 2008). Often, these ionospheric structures are nighttime phenomena

since the depletion regions are filled in when the Sun rises and increases the production rate. Equatorial irregularities can also manifest as Spread-F on high frequency (HF) radar ionograms. Spread-F occurs when the ionospheric F region becomes diffused and irregularities scatter the radio waves (McNamara, 1991; Abdu et al., 2009; Zolesi and Cander, 2014).

Geomagnetic storms are known to be a dominant factor in either suppressing or establishing favorable conditions for the R-T instability mechanism that will subsequently lead to the generation of irregularities at the equator, particularly in terms of the storm-time changes to the PRE (see e.g. Abdu, 2012). Aarons (1991) reported that during geomagnetic storms the ring current seems to play a major role directly or indirectly in establishing the conditions that lead to the equatorial F-layer irregularity generation and/or inhibition. Using equatorial ionospheric data collected from two widely separated stations (i.e. Manila and Huancayo), Aarons (1991) was able to show that when the maximum ring current energy, as inferred from the Dst index, occurred during the midnight to postmidnight time sector, irregularities were generated. Furthermore, when the peak of the storm occurred during 18:00-22:00 LT, little or no effect on the occurrence of ionospheric irregularities was observed that night. Lastly, when the minimum occurred in the early afternoon, the irregularities were inhibited. Thus, suggesting that geomagnetic activity plays a key role in the formation or inhibition of irregularities by changing the progression of events.

It has been reported that the occurrences of irregularity appears to decrease during geomagnetically active periods (Zolesi and Cander, 2014). However, in a case study of a moderate geomagnetic storm during 28-30 May 2010, de Abreu et al. (2014)

reported that there was no generation or suppression of ionospheric irregularity associated with the geomagnetic storms over the American and African sectors. Furthermore, the authors suggested the necessity for additional studies in order to fully understand the suppression or generation of ionospheric irregularity during moderate geomagnetic storms.

The primary mechanisms behind the inhibition or generation of irregularity appears to be the height of the F2-layer, with a possible contribution by the pre-reversal drift velocity and the rate of decrease of the layer. While the under-shielding eastward electric fields may generate the ESF/plasma bubbles during the post-sunset sector, the over-shielding eastward electric fields may trigger the plasma bubbles in the post-midnight sector (Abdu, 2012). On the other hand, the over-shielding westward electric field may suppress the evening PRE and the post-sunset ESF/plasma bubble development, whereas the under-shielding westward electric field may cause irregularity disruption at later hours. Under-shielding electric field is a dawn to dusk electric field, that is, eastward (westward) during the day (night) whereas the over-shielding electric field is a dusk to down electric field, that is, westward (eastward) during the day (night) (Abdu, 2012).

2.5 Summary

In this chapter the general morphology, the different regions and variability of the ionosphere was briefly discussed. The Sun-Earth interaction in relation to disturbance conditions and its effects on Earth's ionosphere in the form of geomagnetic storm effects was also mentioned. Ionospheric structures, such as the EIA, and ionospheric irregularities on equatorial and low latitudes, which will be further discussed in Chapter 6, were briefly discussed.

Chapter 3

Data sources and methodology

This chapter describes the data sources and instruments that were used to conduct the research for this thesis. In particular, the basis of the Global Positioning System (GPS), with the focus on the derivation of GPS total electron content (TEC), is discussed in Section 3.1. The Communication/Navigation Outage Forecasting System (C/NOFS) satellite and magnetometer measurements are also discussed in this chapter. GPS TEC and magnetometer derived indices are also discussed in brief in this chapter.

3.1 Introduction to the GPS

The GPS is part of the Global Navigation Satellite System (GNSS) and was developed by the United States' Department of Defense (DoD) for instantaneous determination of position and velocity (Hofmann-Wellenhof et al., 1997). The GPS is an all-weather, global coverage, satellite-based radio navigation system (NAVSTARGPS, 1996), which provides information for both the military and civilians. The GPS network also provides instantaneous global measurements of the ionosphere with high temporal resolution and near real-time data acquisition which benefits the scientific

community (Mannucci et al., 1999).

The space segment of the GPS consists of 32 satellites in orbit (including spares) shared among six semi-synchronous orbits at an altitude of approximately 20,200 kilometres (Misra and Enge, 2006; Kinrade, 2013). With this constellation a user located anywhere on the globe is in direct line of sight of at least four satellites at any given time. GPS satellites broadcast coded radio signals continuously on two separate L-band frequencies, namely L1 (1.575 GHz) and L2 (1.227 GHz) (Misra and Enge, 2006).

3.1.1 GPS signal propagation through the ionosphere

The ionosphere is a dispersive medium to radio wave signals. GPS signals experience time delays and phase advances as they propagate through the ionosphere, because the ionosphere's refractive index is frequency dependent. Therefore, with due attention to the propagation of the radio wave signals through the ionosphere, and with the assumption that the collision of electrons and neutral atoms in the ionosphere, as well as the assumption that impact of the the magnetic field on the ionosphere is negligible, simplifies the Appleton-Hartree formula to (Davies, 1990),

$$\mu^2 = 1 - X \tag{3.1}$$

where μ represents the ionospheric refractive index and X is the ratio of the squares of the angular electron plasma frequency (ω_{pe}) to the angular frequency of the propagating radio wave (ω).

At GPS frequencies, the higher order terms can be neglected and the refractive

index is approximated by (Parkinson and Spilker, 1996):

$$\mu \approx 1 - \frac{1}{2}X \tag{3.2}$$

where

$$X = \frac{\omega_{pe}^2}{\omega^2} = \frac{[2\pi f_{pe}]^2}{[2\pi f]^2}, \tag{3.3}$$

$$f_{pe} = \frac{N_e e^2}{4\pi^2 m_e \varepsilon_0}, \tag{3.4}$$

$e = 1.60 \times 10^{-19}$ C is the electron charge, $m_e = 9.11 \times 10^{-31}$ Kg is the electron mass, $\varepsilon_0 = 8.85 \times 10^{-12}$ F/m is the permittivity of free space, and N_e is the electron density.

Therefore, substitution of Equation 3.3 into 3.2 along with the constants, yields the refractive index of the ionosphere as:

$$\mu = 1 - \frac{40.31}{f^2} N_e \tag{3.5}$$

where 40.31 is a constant with units of $m^3 s^{-2}$ (Hofmann-Wellenhof et al., 1997; Misra and Enge, 2006).

Furthermore, as a result of the dispersion of the ionosphere, a group delay and a carrier phase advance are introduced. Thus, the measured code pseudoranges are too long, while the measured carrier phase pseudoranges are too short relative to the actual satellite and receiver geometric range. However, the difference in both measurements is the same (Hofmann-Wellenhof et al., 1997). Mathematically, the phase and group refractive indices of the medium can be written as:

$$\begin{aligned} \mu_p &= 1 - \frac{40.31}{f^2} N_e \\ \mu_g &= 1 + \frac{40.31}{f^2} N_e \end{aligned} \tag{3.6}$$

respectively.

The measured range ρ between satellite S and receiver R along the signal path, according to Fermat's principle (Hofmann-Wellenhof et al. (1997)), is given by the equation:

$$\rho = \int_R^S \mu d\rho. \tag{3.7}$$

Similarly, the geometric range ρ_0 along the straight line between the satellite and receiver can be derived by setting $\mu = 1$, is given by:

$$\rho_0 = \int_R^S 1 d\ell. \tag{3.8}$$

The ionospheric delay ($\Delta\rho$) is the difference between the measured and geometric range:

$$\Delta\rho = \rho - \rho_0 = \int_R^S \mu d\rho - \int_R^S 1 d\ell. \tag{3.9}$$

Substituting the value for μ from Equation 3.7 and assuming the integration in Equation 3.8 to be along the geometric path, so that dρ becomes dℓ, the group delay in Equation 3.9 reduces to:

$$\Delta\rho_g = \frac{40.31}{f^2} \int_R^S N_e d\ell. \tag{3.10}$$

Following a similar procedure, the phase advance becomes:

$$\Delta\rho_p = -\frac{40.31}{f^2} \int_R^S N_e d\ell. \tag{3.11}$$

The propagation speed of radio waves in the ionosphere is known to depend upon the integrated number of electrons along the line-of-sight path of the radio signal, extending between the satellite in space and the receiver on the ground. This forms

the definition of total electron content (TEC), which is measured in TEC units (TECU), defined as 10^{16} electrons per square meter. Mathematically, it is expressed as:

$$TEC = \int_R^S N_e(r, \theta, \phi, t) ds \tag{3.12}$$

where r is the radial distance from the centre of the Earth, θ, ϕ are the latitude and longitude, respectively, t is the time, and s is the distance along the satellite-to-receiver ray path.

Since the integral part in Equations 3.11 and 3.12 is the definition of TEC, the equations for the carrier phase advance and group delay, according to Hofmann-Wellenhof et al. (1997), may be rewritten as:

$$\Delta\rho_g = \frac{40.31}{f^2} TEC \tag{3.13}$$

$$\Delta\rho_p = -\frac{40.31}{f^2} TEC \tag{3.14}$$

A linear combination of the measured pseudorange and phase observables recorded by the receiver on the two L-band carrier frequencies is used to quantify GPS-derived TEC measurements. TEC is measured in slant TEC (sTEC), i.e. TEC measurement along the line of sight of the signal path, and converted to TEC measured in the vertical direction, namely vertical TEC (vTEC) (Chartier et al., 2012). sTEC to vTEC mapping is done with a single layer ionospheric model which applies a cosec transform, considering the geometry in Figure 3.1 (Hofmann-Wellenhof et al., 1997). Thus,

$$\text{sTEC} = \frac{\text{vTEC}}{\cos \text{z}'}, \qquad \sin \text{z}' = \frac{\text{R}_E}{\text{R}_E + \text{H}} \sin \text{z} \tag{3.15}$$

where R_E is the Earth's radius ($\sim$ 6378 km), H is the assumed single layer ionospheric shell height of 350 km, while z and z$'$ are the zenith angles at the observation site and sub-ionospheric pierce points (IPPs) respectively.

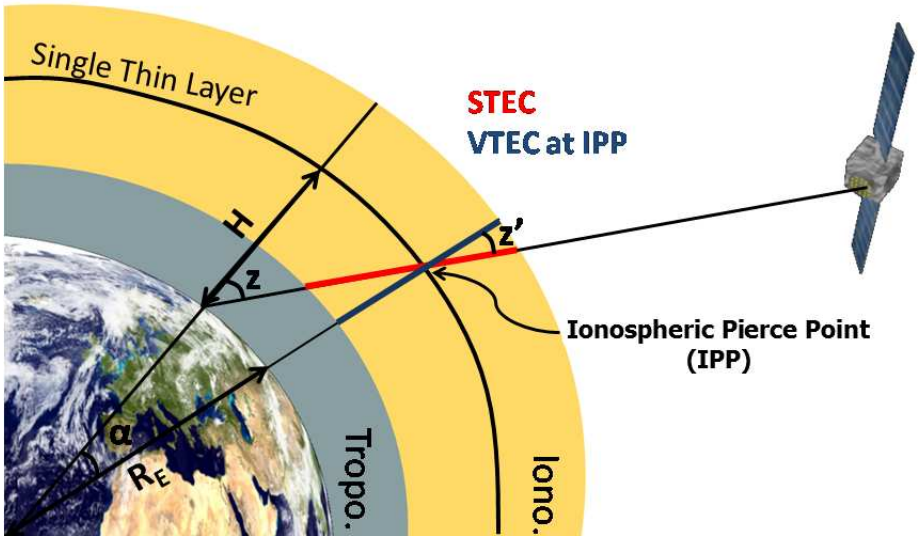

Figure 3.1: Depiction of the geometry of signal propagation through the ionosphere. Source http://gnss.be/ionosphere_tutorial.php.

GPS receivers are available in either single or dual frequency receivers, both at ground stations or on board low Earth orbit (LEO) satellites. A single frequency receiver receives signals on the L1 band only and therefore is not able to eliminate ionospheric error from the signal. However, dual frequency GPS receivers receive both the L1 and L2 signals simultaneously, which enables them to eliminate the major part of ionospheric signal error (Hofmann-Wellenhof et al., 1997; Hoque and Jakowski, 2012). Therefore, dual frequency GPS receivers provide more accurate timing and navigation information than the single frequency GPS receivers.

3.1.2 Dual-frequency TEC measurements

GPS TEC measurements contain, in addition to the errors introduced by the ionosphere, satellite and receiver biases, satellite clock error, multi-path errors and troposphere errors (Allain and Mitchell, 2009; Rose, 2011) which make direct measurement of TEC difficult. To overcome the problem, direct measurements from the differential code delay and phase advance measurements on the L1 and L2 frequencies are considered. GPS receivers record L1 and L2 data in RINEX (Receiver INdependent Exchange) format, which is the current standard format for GPS receivers (Misra and Enge (2006)). RINEX files list the L1 and L2 carrier phase and pseudocode path lengths (observables) for each satellite in view, sampled at 1 or 30 second intervals (Meggs et al., 2005; Allain and Mitchell, 2009). Since the observables ranges which are computed from measured time delays based on a comparison between received signals and receiver generated signals (Hoque and Jakowski, 2012), they are prone to biases. The biases could differ in nature, including satellite and receiver clock errors, instrumental biases and atmospheric effects (Rose, 2011; Allain and Mitchell, 2009). The RINEX files of GPS receivers contain the following observables (Hofmann-Wellenhof et al., 1997; Rose, 2011):

$$P_1 = P_0 + \frac{40.31}{f_1^2} TEC + \varepsilon_1 \tag{3.16}$$

$$P_2 = P_0 + \frac{40.31}{f_2^2} TEC + \varepsilon_2 \tag{3.17}$$

$$L_1 = P_0 - \frac{40.31}{f_1^2} TEC + n_1\lambda_1 \tag{3.18}$$

$$L_2 = P_0 - \frac{40.31}{f_2^2} TEC + n_2\lambda_2 \tag{3.19}$$

where P_1 and P_2 are the pseudoranges from the precise P code, L_1 and L_2 represent carrier phases of the signals in meters. P_0 is for an ionosphere free pseudorange while n and λ represent the integer ambiguity and the carrier wavelength, respectively. The term ε represents the dispersive component of the receiver and satellite hardware errors.

Taking the difference between the observables for both phase and code ranges, two equations for TEC can be given as:

$$P_1 - P_2 = 40.31 \times TEC(f_1^{-2} - f_2^{-2}) + \varepsilon_1 - \varepsilon_2 \tag{3.20}$$

$$L_1 - L_2 = -40.31 \times TEC(f_1^{-2} - f_2^{-2}) + n_1\lambda_1 - n_2\lambda_2 \tag{3.21}$$

Therefore, TEC may be obtained by using Equation 3.20 together with a noise term. Similarly, Equation 3.21 provides TEC together with an offset term from the integer ambiguity associated with it. The integer ambiguity is constant as long as the satellite is visible (ignoring sudden or large changes in cycle slips) (Misra and Enge, 2006; Rose, 2011). The offsets associated with large cycle slips are easily detectable (Allain and Mitchell, 2009). Therefore, TEC may be calculated by fitting Equation 3.21 into Equation 3.20. In addition, the offset between such slips is equivalent to a weighted mean of the differences between Equations 3.20 and 3.21 and the weights are correlated with the signal to noise ratio (Allain and Mitchell, 2009).

By deriving TEC from the dual-frequency measurements in the above equations,

reconstruction of the ionospheric electron density profiles and imaging of the ionospheric TEC map is possible by means of tomography, technique which will be discussed in Chapter 4.

3.2 GPS-TEC indices

Relative slant TEC (sTEC) values of 30-second interval were obtained by using the GPS-TEC software developed by Boston College (Seemala and Valladares, 2011). The software uses the phase and code values of the L1 and L2 GPS frequencies to eliminate clock and tropospheric water vapor errors (Sardón and Zarraoa, 1997). The absolute values of sTEC are then obtained by applying differential satellite code biases as published by the University of Bern, and receiver biases estimated by minimizing TEC variability between 0200 and 0600 local time. Assuming the thin shell model, the equivalent vertical TEC at an IPP altitude of 350 km is calculated (Ciraolo and Spalla, 1997).

From sTEC, we can compute the rate of change of line-of-sight TEC (ROT) in TECU/min using Equation (3.22):

$$\mathrm{ROT} = \frac{\mathrm{sTEC}^i_{j+1} - \mathrm{sTEC}^i_j}{(\mathrm{t}^i_{j+1} - \mathrm{t}^i_j) \times 60} \tag{3.22}$$

where t_j,t_{j+1} are times in hours at intervals of 30 seconds for all visible i satellites. The ROT can offer information on the spatial variation of electron density at large-scale lengths (Basu et al., 1978, 1999) and detect ionospheric irregularities in the order of kilometers (Basu et al., 1996; Pi et al., 1997; Mungufeni et al., 2015). Moreover, Pi et al. (1997) reported that the fluctuations in ROT, for high-elevation angles, are due to ionospheric irregularities with scale sizes of several hundred meters to about 2.5 km at low- and middle latitudes. However, these values depend on

the plasma velocities.

Similarly, to identify small-scale irregularities (orders of metres to few km), Pi et al. (1997) defined the rate of change of the TEC index (ROTI) by taking the standard deviation of ROT over a five-minute period. Jacobsen (2014) assessed the impacts of different sampling rates and calculation time intervals on ROTI values and found that the median level of ROTI depends strongly on sample rate and on latitude at auroral latitudes, but weakly on time interval. This is of particular relevance for statistical studies. Moreover, the author found that the correlation between ROTI using 1/30 s sampling rate and different time intervals was strongly positive. The ROTI sampling rate used in the current study has been implemented for multiple studies on the region of this study (e.g. Ngwira, 2012; Amabayo et al., 2015; Mungufeni et al., 2015, 2016). According to Zou and Wang (2009), large- and small-scale ionospheric irregularities at scale lengths of a few hundred kilometers and ∼400 m can be investigated simultaneously with the ROT and ROTI indices. Moreover, the presence of large-scale depletions of TEC or plasma bubbles are associated with large-scale irregularities, as reported by Basu et al. (1999). These indices will supplement the EPB observations from the C/NOFS satellites, which are discussed in Chapter 7.

3.3 C/NOFS observation

The C/NOFS satellite was launched into a low inclination (13°) orbit, with perigee of 400 km and apogee of 850 km, in April 2008 as a mission of the Air Force Research Laboratory. The primary purpose was to forecast ionospheric irregularities in the equatorial ionosphere that cause problems in communication and navigation systems (de La Beaujardière et al., 2004). According to de La Beaujardière et al. (2004), the

primary scientific objectives of the C/NOFS mission were to: understand physical processes active in the background ionosphere and thermosphere in which plasma instabilities grow; identify mechanisms that trigger or quench the plasma irregularities; and determine how the plasma irregularities affect the propagation of electromagnetic waves. Therefore, C/NOFS was equipped with sensors that measure multiple parameters including, ambient and fluctuating electron densities; ion and electron temperatures; AC and DC electric fields; magnetic fields; neutral winds; ionospheric scintillations; and electron content along the lines of sight between C/NOFS and the Global Positioning System (GPS) (de La Beaujardière et al., 2004).

The Planar Langmuir Probe (PLP) on board the C/NOFS satellite is an in situ dual-disk probe that measures the ambient ionospheric density and electron temperature. Abundant plasma density measurements with a time resolution of 1 Hz ($\sim$ 7.5 km in spatial units) during the day and at 512 Hz during the night can be provided by the PLP (Dao et al., 2011). The striking feature of C/NOFS observations is the detection of local plasma depletions in the ambient ionospheric density, i.e. EPB as described earlier in Section 2.4.

The Coupled Ion Neutral Dynamics Investigation (CINDI) is another instrument that flies aboard the C/NOFS satellite. It includes a planar retarding potential analyser and a planar ion drift meter that together provide a measure of the total ion concentration and the vector ion drift in the satellite reference frame (Heelis and Hanson, 1998). The Ion Velocity Meter (IVM) of the CINDI payload, measures the ion drifts every half second with the reference axes maintained approximately in the direction of the satellite motion, along the local vertical in the orbit plane and along the local horizontal perpendicular to the orbit plane (Stoneback et al., 2011). In the reference frame of the satellite, the local horizontal points generally

northward, contributing positively to the meridional direction in the northern hemisphere and negatively in the southern. Similarly, the local vertical is generally radial, contributing positively to the meridional direction in both hemispheres. With the requirement that the longitude and local time average of the meridional (vertical) ion drift be zero, the offsets in the ion drift components can be determined. Thus, after isolating the offsets in the local vertical and local horizontal components, based on the symmetry of each component in the meridional direction across the magnetic equator, corrected drifts are produced in the spacecraft frame (Burke et al., 2009; Stoneback et al., 2011, 2012). The meridional drift component of the Ion Velocity Meter (IVM) measurement (i.e. V mer(m/s)), defined as the drift perpendicular to **B** in the plane of the magnetic meridian, was used in this study. The upward **E** × **B** meridional drift corresponds to an eastward zonal electric field.

3.4 Magnetic field indices

The Earth's magnetic field and its fluctuations are measured by an instrument known as a magnetometer. The fluxgate magnetometer is the conventional instrument for low-frequency measurements at magnetic observatories, typically sampling at 1 Hz or lower (Phiri, 2013). Ground-based magnetometer measurements have been used to infer the electrodynamics of the equatorial ionosphere, because the horizontal component of the geomagnetic field at the dip-equator reflects the changes in the equatorial ionospheric current system (Anderson et al., 2004). However, the magnetic fluctuations recorded by ground-based magnetometers contain contributions from the global field fluctuations associated with the ring currents (Dst) and local magnetic field variations, which includes those from the equatorial electrojet (Rastogi and Klobuchar, 1990; Yizengaw and Moldwin, 2009). The commonly used method of isolating the local fluctuations from the magnetospheric sources, involves

taking the difference in the magnitudes of the H-component, after normalization with mean nighttime values, (i.e. ΔH) of a magnetometer positioned directly on the dip-equator and one displaced 6° - 9° away (Anderson et al., 2004; Yizengaw and Moldwin, 2009). This is done because a magnetometer at the EEJ zone measures the total magnetic field, which is the sum of the Earth's background magnetic field, the northward magnetic field due to the eastward EEJ and other sources of magnetic field in space. The magnetometer placed off the EEJ zone measures the Earth's background magnetic field and the magnetic field from other sources. The assumption is that the effect from other sources is the same on the background magnetic fields at both locations. Towards this purpose a magnetometer station located at the dip equator (Addis Ababa (AAE), 0.13° N, 111.10°E, geomagnetic coordinates) from INTERMAGNET[1] and another located at Adigrat (ADI, 5.80°N, 111.06°E, geomagnetic coordinates))from the African Meridian B-Field Education and Research (AMBER)[2] array (Yizengaw and Moldwin, 2009) were used in this study. These indices will be presented in Chapter 8.

Geomagnetic indices (e.g. Dst and Kp) are used to specify the level of geomagnetic field fluctuation. The Dst index is a measure of the reduction of the horizontal components of the Earth's magnetic field. The Kp (planetarische Kennziffer) index (Bartels et al., 1939) is a measure of variation in the Cartesian components of the Earth's magnetic field (x, y, z), for each 3-hour period of every Universal Time (UT) day. The Dst index, measured hourly, indicates the severity of a geomagnetic storm and the development of the ring current (Sugiura and Wilson, 1964). Based on their effect on the ionosphere, the strength of the geomagnetic storms are categorized as follows: Dst $\leq$ -30 nT as weak geomagnetic storm conditions, -50 nT $\geqslant Dst >$ -100 nT as moderate geomagnetic storm conditions, -100 nT $\geqslant Dst >$ -200 nT as strong

[1] http://www.intermagnet.org
[2] ftp://magnetometers.bc.edu/dat/amber/

geomagnetic storm conditions, Dst $\leq$ -200 nT as severe geomagnetic storm conditions and -200 nT $\geqslant Dst >$ -350 nT as great geomagnetic storm conditions (Loewe and Prölss, 1997). The symmetric disturbance field in the horizontal component of the Earth's magnetic field H, SYM-H, gives information similar to that of Dst about the geomagnetic storm, but at a higher resolution of 1 minute (Wanliss, 2007).

Kp values range from zero (i.e. quiet geomagnetic condition) to 9 (i.e. highly disturbed geomagnetic conditions). Therefore, Kp $<$ 3 indicates quiet geomagnetic conditions, 3$\leq$ Kp $<$ 6 indicates moderate geomagnetic conditions, while Kp $\geqslant$ 6 indicates severe storms (Richardson et al., 2001).

The auroral electrojet (AE) index is a measure of the energy deposited in the auroral regions. This index measures the total range of deviation of the horizontal magnetic field around the auroral oval at a time instant from quiet day values (Davis and Sugiura, 1966). The AE index is used as an indicator of substorm activity, which could also cause disturbances in the ionosphere.

3.5 Satellite data: solar wind and thermosphere parameters

Solar wind data gathered from various spacecrafts, such as the Advanced Composition Explorer (ACE), Solar and Heliospherical Observatory (SOHO), Wind, Geotail, etc. is publically and readily available. To provide continuous and reliable data, comprehensive databases hosted and maintained by the National Space Science Data Center (NSSDC) and the NASA Goddard Space Flight Center and its affiliations were consolidated into dataset archives, namely OMNI which evolved into OMNI 1

and the present OMNI 2 (King and Papitashvili, 2003; Habarulema, 2010).

The ACE satellite orbits around the L1-Lagrange point which is $\sim$ 1.5 million km ($230R_E$) from Earth and $\sim$ 148.5 million km from the Sun (Stone et al., 1998). L1-Lagrange is a point on the Sun-Earth gravity vector where the Sun and Earth's gravitational attraction is in equilibrium. The ACE satellite provides continuous near real-time measurements of solar wind parameters and solar energetic particle intensity. Moreover, it provides an advance warning (about one hour) of geomagnetic storms. ACE also measures the strength and orientation of the interplanetary magnetic field (IMF) embedded in the solar wind. Further details on ACE can be found in Stone et al. (1998).

The OMNI dataset comprises low and high resolution data for the IMF and solar wind plasma parameters. Several spacecraft (e.g. ACE, Wind, ISEE 3, Geotail and IMP 8) orbiting at different altitudes contribute to the OMNI dataset (King and Papitashvili, 2005). Therefore, the OMNI data is corrected for associated time delays (i.e time-shifted) and is generally considered as the observation data from the bow shock nose. In this study, time-shifted one-minute averaged solar wind condition indicators, such as the solar wind bulk velocity, Vsw (km/s), IMF Bz (nT), the dawn-to-dusk component of the interplanetary electric field, (i.e. IEF Ey (mV/m)), obtained from the OMNIWEB[3] data centre were used.

The Solar and Heliospherical Observatory (SOHO) is located at the L1-Lagrange point. SOHO images the Sun's corona in several electromagnetic frequencies, including X-ray and UV, and provides the first visual indication of solar flares and coronal mass ejections (CMEs). Therefore, observations from the SOHO mission's

[3] http://omniweb.gsfc.nasa.gov/form/omni_min.html.

Large Angle and Spectrometric Coronagraphs (LASCO)[4] are used to examine the geoeffectiveness of Halo CME events (e.g. Gopalswamy, 2009; Robbrecht et al., 2009, and references therein).

The Global Ultraviolet Imager (GUVI) on NASA's Thermosphere Ionosphere Mesosphere Energetics and Dynamics (TIMED) mission, measures the variability of thermospheric composition and its responses to auroral inputs (Paxton et al., 1999). TIMED/GUVI simultaneously recorded far-ultraviolet (FUV) dayglow intensities in five colors: H(121.6 nm), O(130.4 nm), O (135.6 nm), N_2 (141.0 - 152.8 nm) and N_2 (167.2 - 181.2 nm) (Crowley and Meier, 2013). The GUVI 135.6 nm and LBHS intensity ratios are independent of solar EUV flux, and the ratios reflect the changes in the thermospheric O/N_2 ratio (Zhang et al., 2004). Therefore, the image gallery of the GUVI[5] instrument on board the TIMED satellite was used (in Chapter 7) to establish the day-to-day variation of the O/N_2 ratio and therefore to determine the effect of composition changes during the disturbed periods under consideration.

3.6 Summary

GPS dual-frequency signals are used to observe the integrated electron density (or TEC) along the satellite-receiver ray path. This measurement technique is fundamental to the research presented in this thesis, and therefore its derivation from the GPS system was discussed in this chapter. Other GPS TEC-derived measurements such ROT and ROTI were also briefly described. Since EPBs form part of this study, and C/NOFS was designed to probe them, measurements by the C/NOFS PLP and IVM payloads were also discussed. Finally, information on magnetic field

[4] LASCO(http://cdaw.gsfc.nasa.gov)
[5] http://guvi.jhuapl.edu/site/gallery/guvi-galleryl3on2.shtml

measurements and associated indices, as well as on solar wind parameters, and the neutral composition ratio (i.e. O/N_2), was also briefly discussed.

Chapter 4

Ionospheric tomography and global models

This chapter presents an introduction to ionospheric tomography and the details and procedures of the inversion algorithm used in this study, i.e. Multi-Instrument Data Analysis System (MIDAS). Details of global models such as the International Reference Ionosphere (IRI) and Global Ionospheric Map (GIM) TEC which were used for comparison purposes, are also introduced. The storm-time reconstruction model, Artificial Neural Networks (ANN), is briefly mentioned.

4.1 Introduction to Ionospheric Tomography

Tomography refers to the process by which a two-dimensional image of a section or a slice of a three-dimensional body is obtained (Fehmers, 1996). The process is performed by externally subjecting a 3D object to penetrative electromagnetic waves, from which the resulting representation of the internal make-up of the structure can be obtained after an inversion of the line-integral measurements. Since Bracewell

(1956) first applied tomography to radio astronomy in 1956, the technique have increasingly become common in multiple fields. Its application to ionospheric imaging was first proposed by Austen et al. (1986). Then, two years later, Austen et al. (1988) demonstrated the feasibility of the use of computerized tomography to reconstruct ionospheric electron density from total electron content (TEC) measurements, simulated from ionospheric models based on Chapman profiles. Reviews of ionospheric tomography algorithms are presented in Kunitsyn and Tereshchenko (2003); Bust and Mitchell (2006).

Ionospheric tomography is the reconstruction of vertical electron density profiles of the ionosphere from a network of line integrals. The phase changes of GPS signals crossing the ionosphere may be recorded either by ground- or space-based receivers. Conventional tomography uses measurements of the line integrals made from dual-frequency trans-ionospheric signals along many intersecting ray paths between Low Earth Orbiting (LEO) satellites and a chain of ground-based receivers (Censor, 1983; Bust and Mitchell, 2006). A study by Yeh and Raymund (1991), showed that the geometry of LEO satellite-to-Earth measurements only allows observations over a limited number of viewing angles and that this imposes limitations on ionospheric tomography. The authors explain that the orientation of satellite-to-receiver ray paths is biased in a vertical direction, with no ray paths running horizontally through the ionosphere owing to the curvature of the Earth. This results in a poorly defined vertical electron concentration gradient when taken by TEC measurements alone. It indicates that tomographic images using conventional inversion algorithms alone are not straightforward and difficult to implement; therefore, tomographic problems has to consider the geometrical constraints in developing inversion algorithms. The issues pertaining to geometry still persist even with the newer satellites systems (e.g. GPS, GLONASS, etc), although to a lesser extent.

Raymund (1994) reported some theoretical limitations and pointed out that the horizontal resolution depends on the spacing between the receivers, while the vertical resolution depends on the number of receivers. The authors conducted simulation studies using the mathematical technique for least-squares fitting, known as singular value decomposition (SVD), to produce the tomographic image from a linear combination of model ionospheres. Na and Lee (1990) applied an orthogonal decomposition technique in which they generated a set of orthonormal basis functions from a priori information. The basis functions chosen were Fourier kernels, where each Kernel was derived from a different frequency component and orientation so that the final tomographic image could be formed from a combination of these basis functions. An algorithm proposed by Fremouw et al. (1992), used a set of vertical orthonormal functions created from ionospheric models to image the vertical profile and a power law spectrum to select the horizontal structures from a Fourier basis, employing linear algebraic matrix inversion. A three-dimensional time-varying ionospheric tomographic imaging algorithm, MIDAS, developed by Mitchell and Spencer (2003), was an extension of the two-dimensional static inversion algorithm developed by Fremouw et al. (1992). The third version of MIDAS, which uses a voxel-based three-dimensional spatial grid instead of spherical harmonics for the horizontal structures, was used in this study.

TEC measurements are basic parameters for ionospheric tomography. However, individual TEC measurements provide no information about the spatial variation of the electron concentration along the ray path. Yet, tomographic algorithms can ingest these linear integral data to produce two- or three-dimensional images of the electron density of the ionosphere. Furthermore, tomographic systems are advantageous over conventional in situ point measurements in that many independent data

can be obtained with relatively few instruments. This is because the amount of data may grow approximately quadratically with an increase in instruments (Howe et al., 1998). However, the quality of ionospheric tomographic images depends mainly on the density of the ray paths, which in turn depends on the number of intersecting ray paths between transmitters and receivers over a wide range of angles (Kunitsyn and Tereshchenko, 2003). In fact, studies show that the quality of the tomographic images using data from an uneven distribution of ground receivers may be equally as bad as the quality of the tomographic images when the data is sparse (Materassi and Mitchell, 2005; Zapfe et al., 2006). This is because uneven distribution of receivers leads to low information content of the dataset and the reconstruction based on such a dataset severely impacts the resolution of the images of electron density and TEC.

The development of three-dimensional, time-varying algorithms make use of the GPS constellation as a data source. Imaging in three dimensions is basically the same as in two dimensions, except that there are complications due to the sparseness of data that have to be overcome. The inversion problem requires defining a three-dimensional grid of voxels, each bounded in latitude, longitude and altitude. Moreover, the contribution of the individual straight-line elements of the signal path between satellite and receiver at each intersected voxel is computed from knowledge of the satellites and receivers locations (Mitchell and Spencer, 2003; Bust and Mitchell, 2008). The assumption is made that the unknown electron concentration within each voxel is constant and contained in the column vector $\mathbf{x}$. Then the nature of the problem can be defined as:

$$A\mathbf{x} = \mathbf{b} \tag{4.1}$$

where the matrix A transforms the electron density to the form and location of the

observations and **b** is the set of observed TEC values (Bust and Mitchell, 2008; Chartier et al., 2012). This approach of solving the tomographic problem is used by MIDAS.

4.1.1 MIDAS algorithm

MIDAS solves time-varying 3D electron density distributions at multiple times by using differential phase measurements of slant TEC. The first version of MIDAS was created by Mitchell and Spencer (2003). It balances a series of spherical harmonics and empirical orthonormal functions derived from Chapman profiles and assumes the ionosphere varies linearly with time. The second version developed by Spencer and Mitchell (2007) was based on a Kalman filter approach, which incorporates physics-based models into the inversion, in the sense of data assimilation approach. The third version of MIDAS, which was used in the present study, relies on a vertical basis function decomposition and a horizontal smoothing function to compensate for a lack of observations (Chartier, 2013).

The goal of MIDAS, in common with any tomographic imaging algorithm, is to invert Equation 4.1, where A is the observation operator (i.e. A is a matrix of GPS ray-path intersections with grid voxels), $\mathbf{x}$ is a vector of electron densities across the grid and $\mathbf{b}$ is a vector of observations. When Equation 4.1 is inverted to solve for the electron density distribution, $\mathbf{x}$, it becomes:

$$\mathbf{x} = A^{-1}\mathbf{b}. \tag{4.2}$$

Since the number of independent observations is unlikely to match the number of grid-points, the problem is underdetermined. This means there are fewer observations than grid voxels (i.e. unknowns). Consequently, the observation vector, A, will

not be a square matrix and therefore it will have no inverse. Moreover, Equation 4.2 cannot be solved if A^{-1} is not known, so Equation 4.1 is multiplied by the transpose of the observation operator, A^T, and rearranged to give (Chartier, 2013):

$$\mathbf{x} = (A^T A)^{-1} A^T \mathbf{b}. \tag{4.3}$$

Now, Equation 4.3 can always be solved, whether the problem is underdetermined, overdetermined, or exactly determined (Chartier, 2013). However, solving the equation directly can be difficult. In MIDAS, the user can choose to use either the least-squares approach (using the minimum residual method) or non-linear optimisation approach (using the quadratic programming method) to do the inversion. The latter method was used in this study. In MIDAS the inversion problem is defined such that the grid is in three spatial dimensions at multiple discrete times so that observations that span multiple times can be ingested. However, in cases where there are insufficient observations, Equation 4.3 can yield multiple solutions. To restrict the possible solutions of the inversion to be physically realistic, MIDAS applies mathematical constraints that will be explained in the next paragraph. The constraints can be either strong or weak.

A strong constraint is one that prevents any solution being returned that is outside of the favoured set (Chartier, 2013; Kinrade, 2013). With MIDAS, a mapping function is applied such that each vertical column of electron density is the sum total of several orthogonal basis functions. These functions are designed to reproduce a series of modelled ionospheric vertical profiles. These profiles can be produced either from the Chapman's equations or from the IRI-95 model. With this the problem is simply mapped from grid space to basis functions space, solved and then mapped back to the grid space for analysis. However, this approach has two limitations. The first limitation is that the basis functions do not force the solutions to be positive as electron densities should be. The second limitation is that it prevents the

inversion algorithm from reproducing unusual ionospheric structures that are not present in the original models. Although the problem of negative electron densities can be negated by good observation coverage, it can be avoided entirely by enforcing a non-negativity constraint in a computationally intensive non-linear optimisation approach. The latter approach was used in this study, because the data coverage in the region of study is scarce.

A weak constraint is applied horizontally (i.e in the latitudinal and longitudinal directions) and across the different times in the solution. MIDAS uses a form of the well-known Tikhonov regularisation that favours solutions with zero second derivatives in these directions (Chartier, 2013; Kinrade, 2013). The overall effect is to promote smooth solutions in regions lacking observations. Although regularisation allows MIDAS to produce accurate images in data-sparse regions if the ionosphere is considered smooth, it can cause artefacts when the ionosphere is not smooth.

MIDAS does not use a background model estimate of the solution in the data assimilation sense, i.e. no weight is given to a modelled estimate of the state in the inversion, although the algorithm is capable of using a modelled starting estimate of the solution to aid the minimization process. However, where a background model is used, the aim is to begin optimisation with an initial guess that is likely to be close to the true solution in order to improve performance. Within MIDAS there is provision to make use of the IRI model (i.e. IRI-95) to provide a starting estimate at the beginning of a series of MIDAS images, after which the solution for the previous time-step is used. However, this option was switched off for this study as the results were compared with the later versions of IRI.

For the MIDAS inversion in this study (presented in Chapters 5 and 6), GPS ground

data over the eastern African longitude sector were gathered from UNAVCO and/or the International Global Navigation Satellite System Service (IGS) and the AFREF networks. The spatial range of the reconstruction covers 30°S to 36°N in latitude and 30°E to 44°E in longitude in steps of 2° each respectively and 100 km to 1200 km in steps of 40 km in altitude.

4.1.2 MIDAS optimisation procedures

Usable observation data from 20 out of the 26 GPS ground stations available during this period were used in the inversion and the remaining six were left for validation. Their geographical locations are shown in Figure 4.1[a].

MIDAS uses observation data from a user-defined time window centered at the time of the inversion. Depending on the choice of the length of the time window, which translates to the amount of observation data ingested in each time step of the inversion process, the final outputs may vary. In the study, MIDAS uses the time windows worth of GPS observation data as the initial guess at the beginning of the run and for all the subsequent runs. Figures 4.1[b], [c] and [d], show the GPS tracks of ionospheric piercing points (IPPs) at an altitude of 350 km for time windows of 3.75h, 5.5h and 7.5h respectively. Also, the MIDAS tests (MIDAS-test1 and MIDAS-test2 in Figure 4.2[a]) are based on the shorter time window, which is evident from the sparse GPS ray paths in Figure 4.1[b]. MIDAS tests (MIDAS-test 3-5) are based on observation data from the 7.5h time window, while MIDAS-test6 was based on the 5.5h time window. Moreover, MIDAS test6 was conducted using the computationally intensive non-linear optimisation approach, an optional feature within MIDAS, that negates the problem of negative electron densities, which all the other MIDAS tests were subjected to, which could be negated

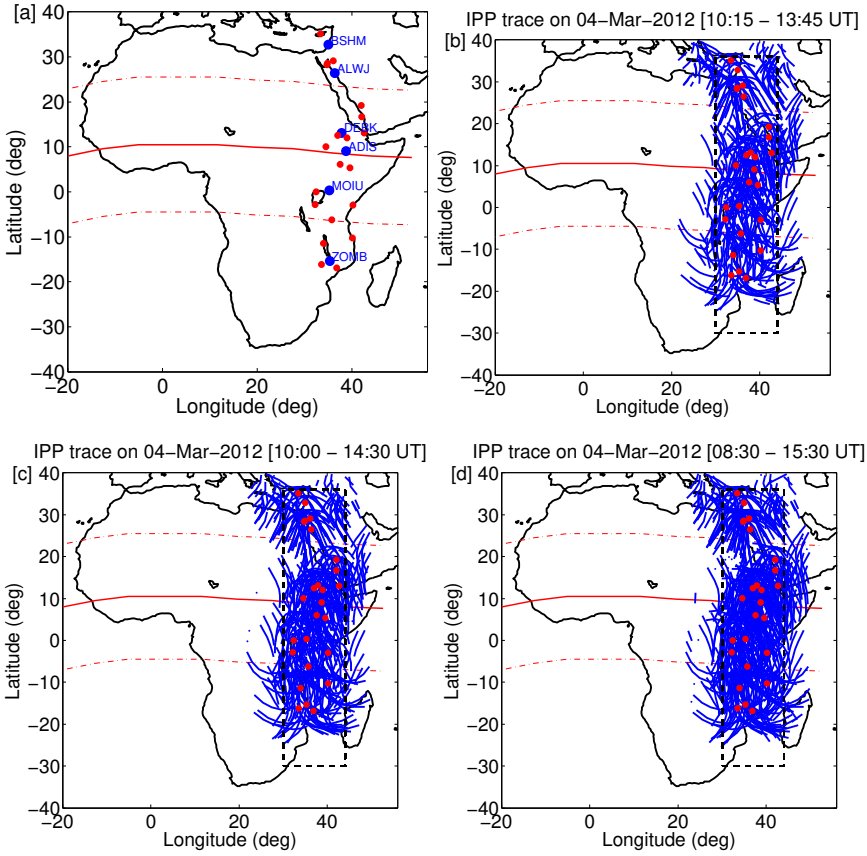

Figure 4.1: [a] GPS stations used in the inversion and validation (station codes marked) and the GPS ray paths at IPP altitudes for time windows of [b] 3.75h, [c] 5.5h and [d] 7.5h worth of data on 04 March 2012. The central time window of these inversions is 12:00 UT.

by good observation coverage (see e.g. Chartier, 2013; Giday, 2014). A summary of the MIDAS optimisation methods that were used for the MIDAS test runs shown in Figure 4.2, is given in Table 4.1.

In order to get the optimum conditions, multiple runs were undertaken in which different options within MIDAS, such as the number of empirical orthogonal functions

Table 4.1: Summary of the MIDAS optimisation methods used to reconstruct the MIDAS test runs shown in Figures 4.2[a].

Test Runs	Time window (hours)	Time steps (minutes)	Number of EOFs	Inversion methods
MIDAS-test1	3.75	15	2	LSM
MIDAS-test2	3.75	15	3	LSM
MIDAS-test3	7.5	30	3	LSM
MIDAS-test4	7.5	30	2	LSM
MIDAS-test5	7.5	30	4	LSM
MIDAS-test6	5.5	30	3	non-linear approach

(EOFs) and the length of the sliding time windows of the inversion process, were varied. Instances of the various MIDAS test runs (test1-test6) are shown for BSHM test station in Figure 4.2[a]. The first two MIDAS test runs (MIDAS-test1 and MIDAS-test2) were conducted in time steps of fifteen minutes, using EOFs derived from two and three Chapman functions, respectively. EOFs were derived from Chapman functions instead of from the IRI model, because the inversion results would be compared with the standalone IRI-2012 model results. MIDAS test runs (MIDAS-test 3-6) were conducted in time steps of 30 minutes and used three, two, four and three EOFs, respectively. Although increasing the number of EOFs for the same time windows, brought some improvement in the outputs, it became computationally expensive. Moreover, despite the improvement, the least-squares minimization (LSM) method within MIDAS which was used for the test runs (MIDAS tests 1-5) produced negative electron-densities, particularly during the nighttimes, which could be negated with adequate observation coverage. Therefore, of all the MIDAS test runs, the test run that produced non-negative electron densities was considered the optimum solution. Consequently, the results of MIDAS-test6 are considered as the

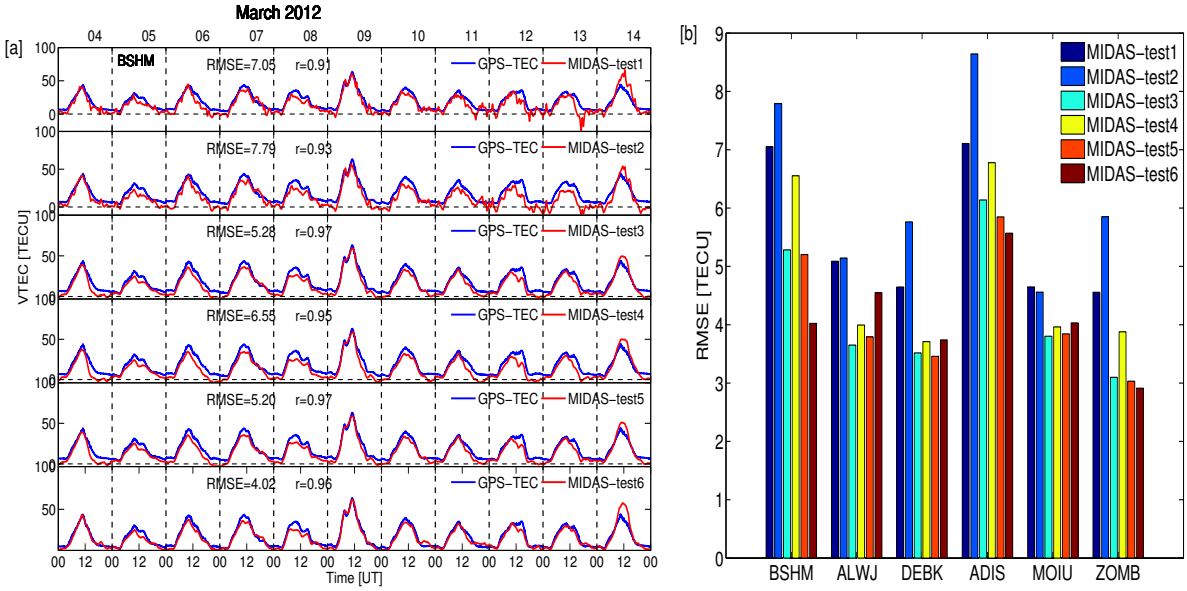

Figure 4.2: [a] An example of how MIDAS outcomes differ when changing the constraint variables within MIDAS and varying the length of time windows of the inversions in the process of optimisation over BSHM station during 04-14 March 2012. The observed VTECs are also over plotted for purposes of comparison. RMSEs computed for all the MIDAS tests (test 1-6) VTEC and the observed VTECs for all the test stations is also shown [b]. The outputs of the MIDAS tests with non-negative values (i.e. MIDAS-test6) were considered for final analysis.

final output for use in this study. The MIDAS VTEC is integrated from the electron density reconstructed. These results were then compared with and validated against the models and observations of TEC.

The MIDAS results based on the methods and specifications mentioned above, are presented in Chapter 5. In Chapter 6 the aforementioned optimised MIDAS methods were used, but with varying input observation data from different GPS stations.

4.2 IRI-2012 model

IRI provides monthly averages of the electron density for any point in the ionosphere at altitude ranges from 50 km to 2000 km (Bilitza and Reinisch, 2008). It was established in 1960 as a joint model of the URSI (Union Radio Scientifique International) and COSPAR (Committee On Space Research) task groups, with the intention of creating a standalone model that could predict the global and temporal mean behaviour of the undisturbed ionospheric parameters (Bilitza, 1986). Since the accuracy of the model in a specific region and/or time period depends on availability of reliable data for that region and time, model predictions may deviate significantly from the real observations in regions and time periods that are not properly represented in its database (Bilitza et al., 2014). Being a data-based model, its accuracy in a specific region or time period depends on the availability of reliable data for the specific region and time; therefore, it is being continually improved with new data and improved modelling techniques by a group of experts over the globe (Bilitza and Reinisch, 2008).

Generally the model's inputs can be classified as either "required inputs" or "optional inputs", depending on the required outputs. In this study the required outputs are the electron densities and TEC. The required inputs include: geographical latitude, geographical longitude, year, day number (day of the year), hour, the solar indices, ionospheric index and magnetic index (Bilitza and Reinisch, 2008; Allain and Mitchell, 2009). Ionospheric index, labelled as "IG12" is calculated using both solar and ionospheric information over a 12-month running mean. The index offers a better estimation of the foF2 parameter than the R12 index. Magnetic index indicates the relationship between magnetic perturbations and magnetospheric phenomena. The perturbations are regarded as regular, or irregular depending on the

scale (Kp-index) developed by Bartels et al. (1939). IRI uses the the 12-month running mean of the F10.7, which indicates the power flux of the radio solar noise measured at a wavelength of 10.7 cm and R12 index, which is an indicator of the solar cycle (Bilitza, 2001). The recent versions of the IRI model, i.e. the Matlab executable of the IRI-2012 Fortran code and the online run IRI-2016[1] were used in this study.

In order to compare IRI with the MIDAS reconstruction results (in Chapter 5), 3D electron density profiles were produced from the Matlab executable of the IRI-2012 run for the same spatial grid (i.e. MIDAS inversion resolution) and temporal resolution used in the inversion. TEC maps were similarly produced for comparisons with the inversion results. In addition, thirty minute resolution of the VTEC values were extracted near the six selected validation GPS stations, the code names of which are marked in Figure 4.1[a]. Moreover, for the stations considered for validation (in Chapter 6), storm-time IRI TEC data was obtained from the online IRI-2016 model run with the aforementioned grid and temporal specifications and the NeQuick as topside option and the STORM option on. TEC values integrated over an altitude range of 50 to 2000 km were produced from the IRI-2016 model (Chartier et al., 2012; Habarulema and Ssessanga, 2017), for comparison with the MIDAS results in Chapter 6.

Significant proportions of the input parameters that have been hitherto ingested into the model are from the mid- and high latitudes, particularly, from the northern hemisphere. Therefore, the model performs better in these regions compared to the low-latitudes and the southern hemisphere, in general (Bilitza and Reinisch, 2008). Moreover, even within the low-latitudes, Africa is highly underrepresented in the

[1] https://omniweb.gsfc.nasa.gov/vitmo/iri2016_vitmo.html

IRI model because of the sparse distribution of ionospheric sensors in Africa over the past years. Despite this, it is the best option available for the region with which to assess new regional models or even tomographic results, such as in this study.

4.3 Global Ionospheric Map (GIM)

The Center for Orbit Determination in Europe (CODE) provides global ionospheric maps (GIMs) obtained by using spherical harmonics functions to model the global vertical TEC (VTEC), using data from about 200 GNSS stations worldwide, at an interval of 2 hours (Liu et al., 2005). The daily GIMs are provided in Ionospheric Exchange (IONEX)[2] format (Schaer et al., 1998). The TEC processing assumes that the ionosphere is an evenly distributed thin shell at an altitude of 450 km and generate global TEC data with the resolution of 2.5° by 5° in latitude and longitude at two-hour intervals (refer to Garcia-Fernandez et al., 2013, and the references therein). Yin et al. (2017) recently used CODE TEC estimates to validate tomographic imaging results. Similarly in this study, GIM VTEC data, set to the same spatial and temporal resolution of MIDAS reconstructions through linear interpolation, were compared to reconstruction results (in Chapter 5) for validation purposes.

4.4 Artificial neural network (ANN)

An artificial neural network (ANN) is a flexible mathematical structure which is capable of identifying complex nonlinear relationships between input and output

[2] ftp://cddis.gsfc.nasa.gov/pub/gps/products/ionex/

datasets (Hsu et al., 1995). In the context of modelling, presentation of known inputs and outputs to an ANN allows it to learn the underlying relationship between the two datasets and to later generalize to estimate the desired output (McKinnell and Poole, 2004; Oyeyemi et al., 2006). The information process is performed within computational units called neurons or nodes and flows from one neuron to another through connection links (Fausett, 1994). For each connection link, there is an associated weight which strengthens inputs in such a way that the higher the weight multiplied by a given input is, the stronger that input will be (Fausett, 1994). Each neuron is characterized by its internal state, also known as its activation or activity level, defined as a function of inputs received by that same neuron (Fausett, 1994). The main task of the activation function is to limit the amplitudes of the output signals of neurons (Haykin, 1994). When neurons are regarded as grouped in different layers, an ANN can have input, hidden and output layers (Fausett, 1994; Haykin, 1994). Depending on the number of layers of connection links available in an ANN, the latter is termed single-layer (one layer) or multilayer (several layers) (Fausett, 1994; Haykin, 1994). When there are no loops in an ANN, the information flow is performed in a forward direction and thus the output from one layer does not affect that same layer. Such a network is called a feed-forward neural network (FFNN) (Fausett, 1994; Haykin, 1994). The FFNN was used in the current TEC modelling.

Details of the ANN technique employed in this study is similar to previous studies (Poole and McKinnell, 2000; McKinnell and Poole, 2004; Oyeyemi et al., 2006; Habarulema et al., 2007; Uwamahoro and Habarulema, 2015). The storm-time TEC results which were reconstructed with this method are described in detail by Uwamahoro et al. (2017), and are presented in Chapter 6. Note that the ANN TEC model used in this study is only capable of reconstructing per station TEC. Hence 1D VTEC in time steps of 30 minutes, extracted for the selected validation stations,

were compared with the MIDAS results in Chapter 6. Also, the validation dataset for ANN modeling were also withheld when reconstructing TEC during the test periods.

4.5 Summary

In this chapter a brief review of ionospheric tomography, with emphasis on the MIDAS algorithm and its optimisation procedure, was given. In addition, this chapter provided general details of the two global models, i.e. IRI and GIM, against which the performance of the MIDAS reconstructions were compared. The last section of this chapter contains a brief description of the ANN-based technique for storm-time TEC reconstruction, that was also used to compare with the MIDAS results.

Chapter 5

Imaging the African equatorial ionosphere

The MIDAS algorithm has been tested over the mid-latitudes of the northern hemisphere (see e.g. Chartier et al., 2012; Spencer and Mitchell, 2007), over Antarctica (Kinrade et al., 2012), the South American equatorial and low-latitude ionosphere (Muella et al., 2011), and the equatorial anomaly (Materassi and Mitchell, 2005). Chartier et al. (2014) conducted a comparison of MIDAS imaging based on African GPS data from the scarcely-populated IGS network alone, and MIDAS imaging based on additional input data from the African Geodetic Reference Frame (AFREF) campaign. The authors reported improvements in imaging when the IGS network data was augmented with data from the campaigned networks, which ultimately reduced the RMS errors by a factor of two for a large part of Africa. Similarly, Giday et al. (2015) conducted MIDAS optimization over South Africa and validated the results with three local ionosondes in terms of maximum electron density of the F2 (NmF2) and peak height of the F2 layer (hmF2) profiles. That study showed that the NmF2 and hmF2 values obtained from MIDAS reconstruction using data from GPS receivers within South Africa, compared well with the ionosonde measurements.

In other parts of the globe, where GPS distribution is better and relatively evenly spaced, imaging multiscale ionospheric structures is possible. For instance, Zheng et al. (2015) developed a multiscale ionospheric tomographic algorithm that allows simultaneous application of multiple overlapping single-scale tomographic images with different pixels sizes to obtain the final reconstructed outputs. Panicciari et al. (2015) also developed a new technique for computerized ionospheric tomography that allows sparsity in the reconstruction coefficients by using wavelet basis functions.

On the African continent, the distribution of GNSS receivers is too sparse and rather uneven, which makes it difficult, if at all possible, to image structures other than large-scale ionospheric structures. Although unevenly distributed and with only sporadic recordings, a fair number of GNSS receivers is available on the East African longitude sector, extending from the north to the south of the equatorial ionosphere. Kassa et al. (2015) studied the temporal and spatial characteristics and the storm time responses of the equatorial ionospheric anomaly and the variations on the NmF2 of the EIA in the East African region, employing 2D computerized ionospheric tomography. However, the authors' results were focussed on the study of the EIA phenomenon and no comparisons were made with other global and/or regional models such as IRI.

This chapter describes the performance of MIDAS for calculating TEC for a narrow East African longitude sector for the period 04-14 March 2012, a period of varying geomagnetic conditions. The results are then compared with TEC from Boston College software (see Section 3.2) as well as TEC from the IRI-2012 model and the Global Ionospheric Maps (GIMs).

5.1 Results and discussions

Figure 5.1 presents geomagnetic indices Dst and Kp during the period of study, i.e. 04-14 March 2012. The study period spans days of quiet and varying magnitudes of disturbed geomagnetic conditions, as shown in Figure 5.1. The biggest storm during this period was a strong storm on 09 March 2012 (minimum Dst= -143 nT at about 0800 UT). Its recovery phase lasted until the next day (i.e. 10 March 2012). During the storm main phase, on 09 March 2012, the Kp index reached a value of 8. In addition, weak geomagnetic disturbances occurred on 04, 06, 08, and 13-14 March, while disturbances of moderate magnitude occurred on 07 and 10-12 March. Detailed discussion on the interplanetary causes of these geomagnetic storm events can be found in Tsurutani et al. (2014). The storm period between 07-11 March 2012 has previously been studied, reporting on different ionospheric aspects on both a regional and global scale (see. e.g. Habarulema et al., 2017, 2015).

For this study, TEC for a specific day was obtained by averaging vertical TEC for all visible satellites on that day. However, in order to retain only useful data, only TEC values corresponding to elevation angles greater than 20° were considered, thus minimizing the contribution by multipath effects. For convenience, qualitative comparisons of the TEC maps constructed by means of MIDAS and the IRI-2012 and GIM models were done for all the validation days at 12:00 UT (LT = UT + 3 on the longitude sector of study). Then, the diurnal VTECs obtained from the MIDAS reconstruction, IRI-2012 and GIM models were compared statistically and validated with the observed VTEC values at the selected six out of twenty-six GPS stations (shown in blue and labeled in Figure 4.1[a]). These stations represent of the middle and low latitudes in both hemispheres, and the equatorial ionosphere along the East African longitude sector, as shown in Figure 4.1[a].

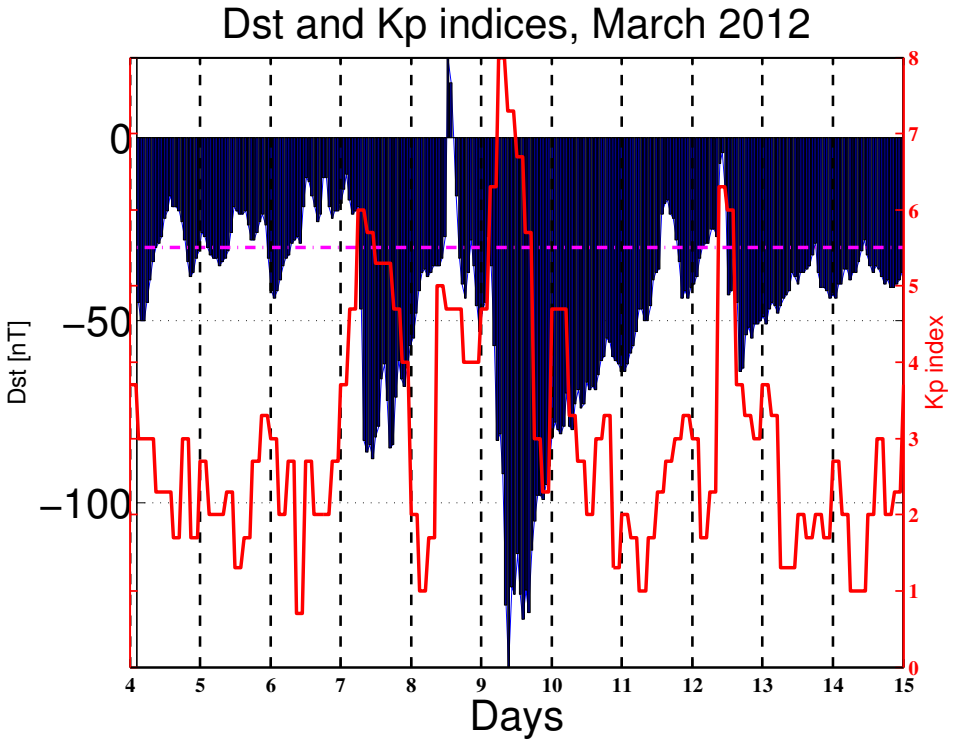

Figure 5.1: Dst and Kp indices during 04-14 March 2012. The dashed magenta horizontal line marks the Dst value of -30 nT.

5.1.1 MIDAS, IRI-2012 and GIM TEC maps

Figure 5.2 presents IRI-2012 (left), GIM (center) and MIDAS (right) TEC maps during 04-09 March 2012 at 12:00 UT, while Figure 5.3 shows the same but for 10-14 March 2012. The TEC maps derived from the IRI-2012 model at 12:00 UT do not seem to vary over the duration of study period of 11 days. This may be attributed to the fact that the IRI-2012 TEC estimates are based on monthly median averages, thus making it impossible to track day-to-day variation accurately (Bilitza et al., 2011). On the other hand, the TEC maps computed from the MIDAS reconstruction and the GIM model displayed significant variation in the TEC evolution throughout the 11 validation days. The TEC enhancement during the 09 March 2012 storm

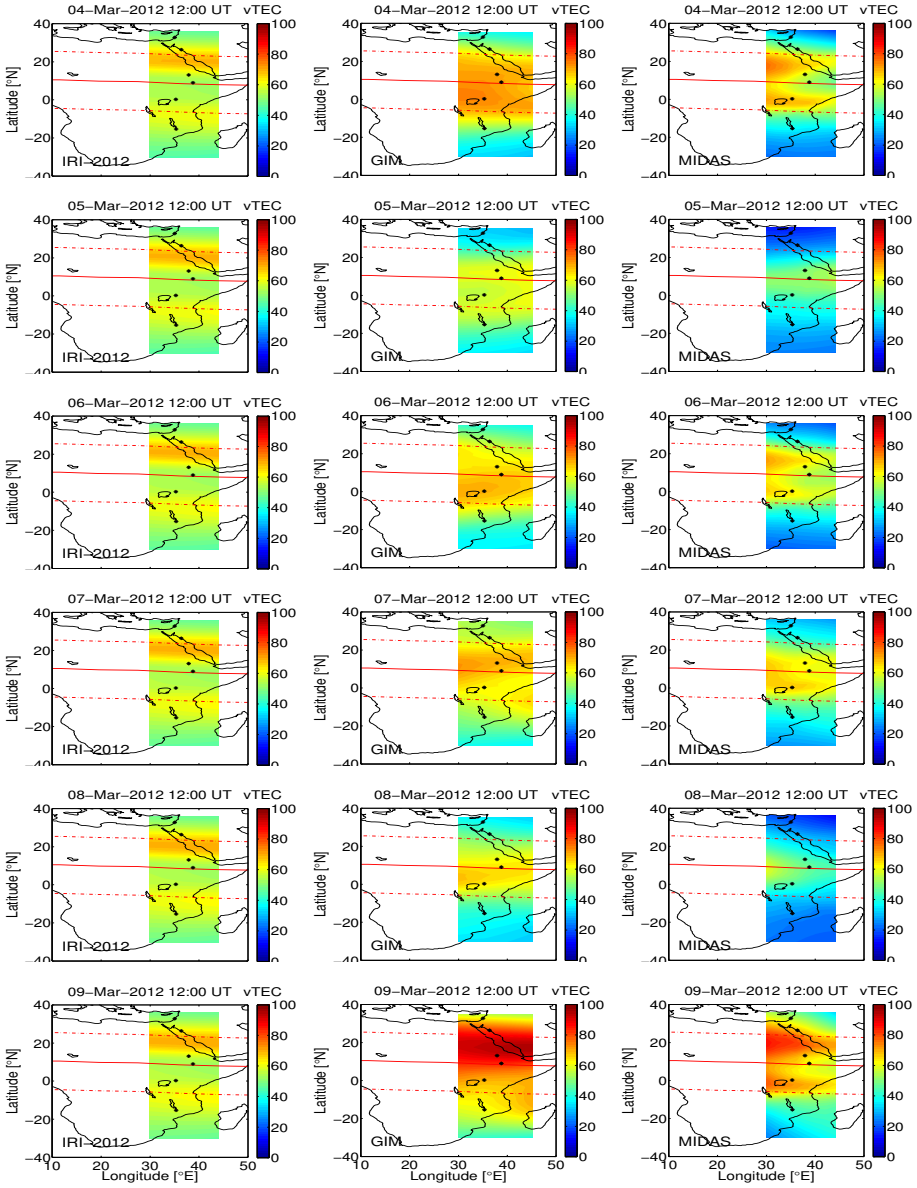

Figure 5.2: TEC maps as computed by IRI-2012 (left) and GIM (center) and MIDAS (right) for 04 - 09 March 2012 at 12:00 UT. The black dots mark the geographical positions of the selected validation GPS stations. The red horizontal line represents the geomagnetic equator, while the dashed red horizontal lines mark ± 15° north and south of it.

reported by Habarulema et al. (2015), was captured by both MIDAS and GIM, although it was more pronounced on the latter. It is also evident from the MIDAS TEC maps that the TEC magnitudes on the far north and south edges of the reconstructed regions are lower than those calculated by the IRI-2012 and GIM models. The TEC maps of the MIDAS reconstruction and GIM model, showed lower TEC values observed on 05, 08 and 13 March 2012 compared to the TEC values of the day(s) before and after at this hour, over the low and mid-latitude regions in particular. This claim will be further ascertained by comparing the 1D VTECs extracted from the inversion and the two models with the observation VTECs for the test GPS stations.

5.1.2 MIDAS, IRI-2012 and GIM VTEC diurnal variation

GPS VTEC observations derived at stations distributed over the northern mid-latitude (BSHM, ALWJ), and low-latitude (DEBK), southern mid-latitude (ZOMB), low-latitude (MOIU) and near the dip equator (ADIS) were compared with those from MIDAS reconstruction, and the IRI-2012 and GIM models. VTEC values derived by means of the Boston College GPS TEC software were sampled at 30 minutes to meet the temporal resolution of MIDAS output for statistical analysis purposes.

Figures 5.4[a]- 5.6[b] display the diurnal VTEC variation of the observed TEC, referred to as GPS-TEC in the figures, and VTEC variation computed by means of (i) MIDAS reconstruction and the (ii) IRI-2012 and (iii) GIM models for the period 04-14 March 2012. For purposes of statistical comparison, the root-mean-square errors (RMSEs) were computed on a daily basis and are presented in the bar graphs (Figures 5.4[a](iv) - 5.6[b](iv)). Moreover, the RMSEs and correlation coefficients

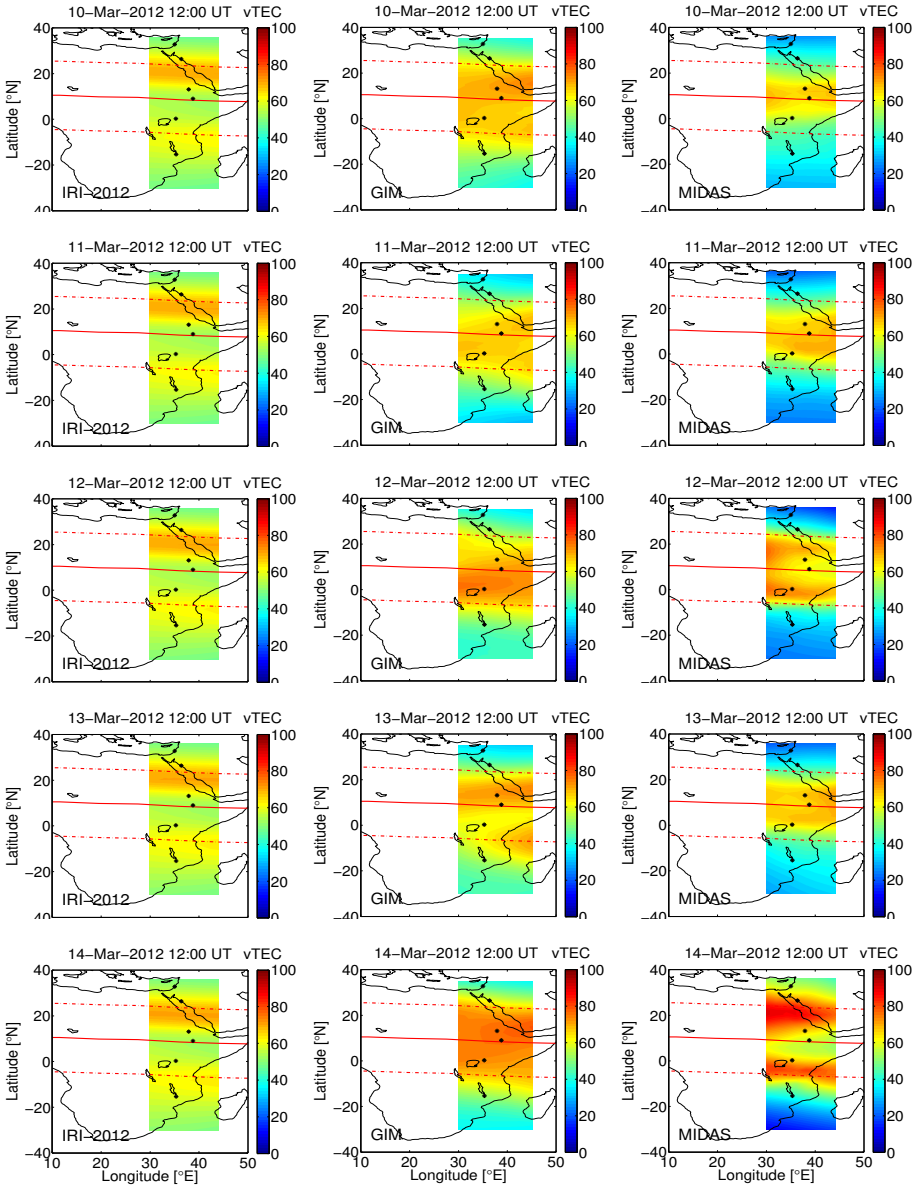

Figure 5.3: TEC maps as computed by IRI-2012 (left) and GIM (center) and MIDAS (right) for 10-14 March 2012 at at 12:00 UT. The black dots mark the geographical positions of the selected validation GPS stations. The red horizontal line represents the geomagnetic equator, while the dashed red horizontal lines mark ± 15° north and south of it.

were computed for the observed and the (left panel) MIDAS inversion, (middle panel) IRI-2012 model and (right panel) GIM model TEC estimates for the entire duration of the validation days and for all the validations stations (Figures 5.4[a](v)-5.6[b](v)).

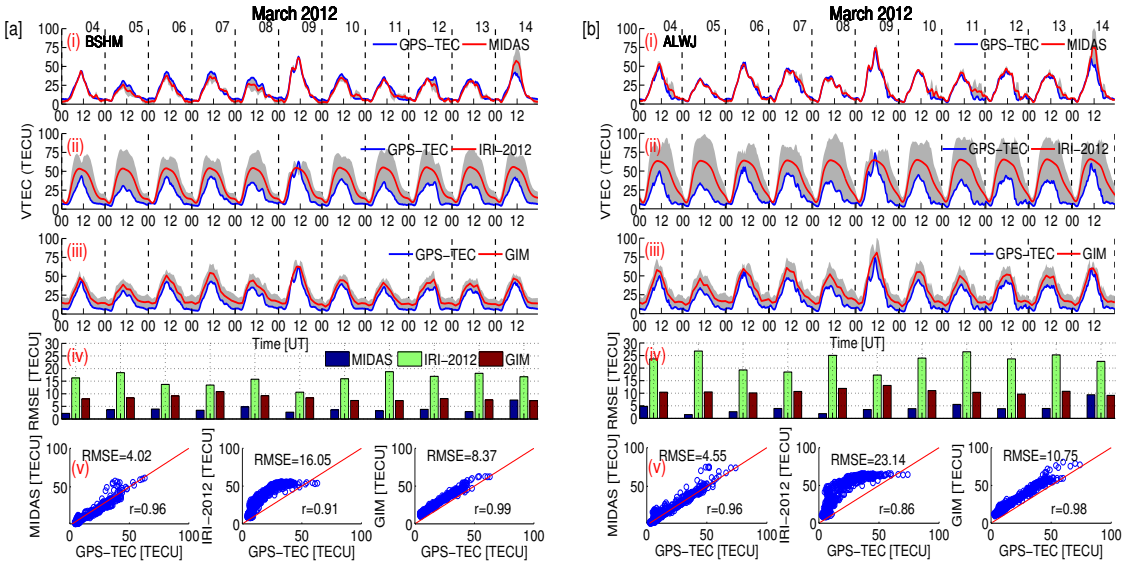

Figure 5.4: VTEC values derived from (i) MIDAS reconstruction , (ii) IRI-2012 model and (iii) GIM model over plotted with GPS-TEC near [a] BSHM and [b] ALWJ stations during 04-14 March 2012. The bar graphs depict the computed daily RMS errors for the GPS-TEC and MIDAS, IRI-2012 and GIM VTECs. The bottom panels (from left to right) show scatter plots with the computed RMSEs and correlation coefficients (r) of observation VTEC (GPS-TEC) and MIDAS, IRI-2012 model and GIM model estimates respectively. The gray patches show $\pm 2\sigma$ error bars around the MIDAS reconstruction, IRI-2012 and GIM diurnal VTECs.

Moreover, to analyze the performance on daily basis, ± 2 standard deviations ($\pm 2\sigma$, i.e. 95% confidence interval) were computed for the observed VTEC values and

the (i) MIDAS reconstruction, (ii) IRI-2012 model and (iii) GIM model VTEC estimates (Figures 5.4[a] - 5.6[b]). The standard deviation is calculated between the GPS values and the corresponding MIDAS, IRI-2012 and GIM VTEC values. This is a standard deviation between the modeled and the observed (GPS TEC) value considering the two data points at each instant for the length of the data. Hence, the gray patches in these figures depict the $\pm 2\sigma$ around the MIDAS reconstruction, IRI-2012 model and GIM model VTECs. Clearly, the error ranges, i.e. the thickness of the gray patches, for the daily values are huge for the IRI-2012 model estimates for all the validation days and all test stations (Figures 5.4[a](ii)- 5.6[b](ii)). These discrepancies are also evident in the RMS errors computed for the daily values, as shown on the bar graphs in Figures 5.4[a](iv)- 5.6[b](iv). The overall performance of the MIDAS reconstruction, in terms of capturing the diurnal trend, was better than the performances of the IRI-2012 and the GIM models for all validation stations during the period studied, except for ADIS where the latter for the most part, seems to have captured the daily peak values well as well (see Figure 5.5[b]), for instance on daily basis, the computed RMSEs was small (i.e. RMSEs of $\sim$3.8 TECU and $\sim$3.5 TECU) on 5 and 14 March for GIM compared to MIDAS (i.e. RMSEs of $\sim$6 TECU and $\sim$7 TECU).

As shown in Figures 5.4[a](i,iv) - 5.6[b](i,iv), the MIDAS reconstruction did not display significant differences with the varying strength of the geomagnetic disturbances during the period 04-14 March 2012. Moreover, the performance of the MIDAS reconstruction did not vary across the different latitudes of the study region for this period, for the most part. However, although not consistent, relatively larger RMSEs were computed near ADIS station (e.g. 6.77 TECU on 10 March), whilst lesser RMSEs were computed near ZOMB station (e.g. 1.46 TECU on 08 March) for

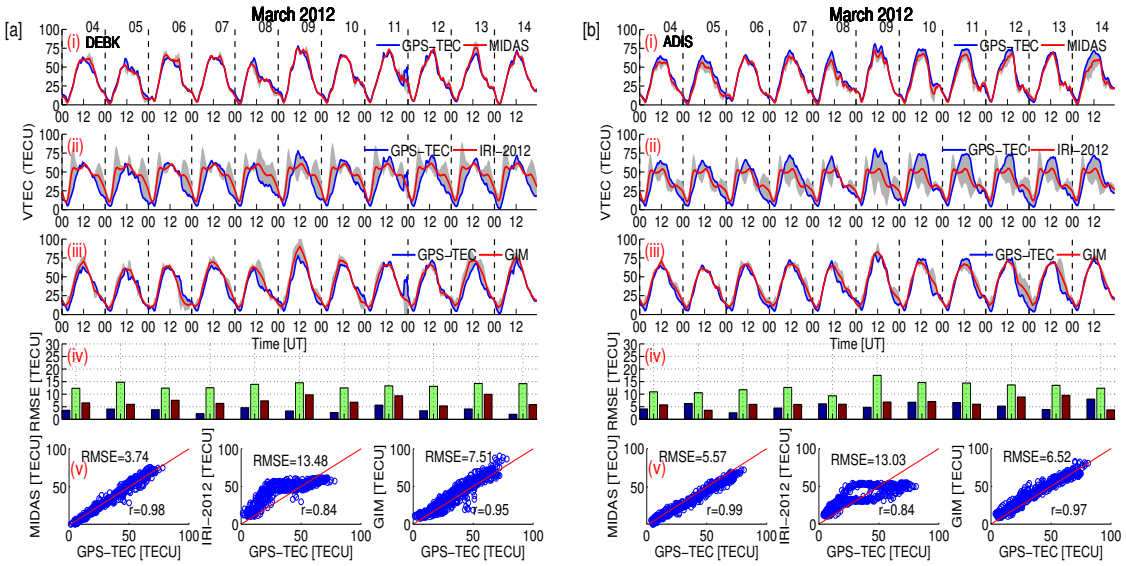

Figure 5.5: VTEC values derived from (i) MIDAS reconstruction , (ii) IRI-2012 model and (iii) GIM model over plotted with GPS-TEC near [a] DEBK and [b] ADIS stations during 04-14 March 2012. The bar graphs depict the computed daily RMS errors for the GPS-TEC and MIDAS, IRI-2012 and GIM VTECs. The bottom panels (from left to right) show scatter plots with the computed RMSEs and correlation coefficients (r) of observation VTEC (GPS-TEC) and MIDAS, IRI-2012 model and GIM model estimates respectively. The gray patches show $\pm 2\sigma$ error bars around the MIDAS reconstruction, IRI-2012 and GIM diurnal VTECs.

this period. An overall better performance of MIDAS imaging was observed for the mid-latitude stations, near ZOMB in particular. This may be attributed to the lower density gradient ionosphere over these latitudes. On the other hand, the relatively larger RMSEs computed for the low-latitude stations reveal the difficulty of imaging the dynamic ionosphere in the region. Conforming to this, a study conducted over the Brazilian equatorial region by Muella et al. (2011) who reported that the

performance of tomographic imaging becomes more inaccurate/problematic in regions of highly dynamic ionosphere such as the equatorial anomaly regions where the ionospheric electron density gradients are steep. Therefore, the large discrepancies between the MIDAS outputs and the GPS-derived TEC for ADIS (and sometimes ALWJ, DEBK and MOIU) may be related to this. Moreover, it has also been reported that the imaging results for areas close to the edges of the reconstruction area, such as BSHM in this case, could be adversely affected (see for example Muella et al., 2011, and the references therein). Conversely, the overall performance of the IRI-2012 model deteriorated with distance from the equatorial ionosphere towards the north and south mid-latitudes ionosphere, except on 09 March 2012, when the ADIS station estimate was equally bad (Figures 5.4[a](ii,iv)- 5.6[b](ii,iv)). It should be noted that the maximum discrepancy was near ALWJ for the duration of observation period with a RMSE of 26.77 TECU on 05 March 2012 (see Figure 5.4[b](ii,iv)). However, there was no noticeable pattern in the IRI-2012 TEC predictions with increasing strength of the geomagnetic conditions. The TEC2F2 model developed by Ssessanga (2014) to study the southern African mid-latitude ionosphere (South Africa in particular) and later the African equatorial ionosphere (Ssessanga et al., 2015) also predicted foF2 values with better accuracy than the IRI-2012 predictions. Similarly, the GIM TEC estimates displayed smaller discrepancies near ADIS and DEBK, while the discrepancies were large for the mid- and low-latitude stations for the observation period, in general. It is worth mentioning that the ability of GIM to estimate the diurnal TEC seemed to deteriorate when the background ionosphere was depleted near the mid-latitude regions (Figures 5.4[a], [b] and 5.6[b]).

Overall, the GPS tomographic results were better than those of the independent global models (IRI-2012 and GIM), even though the inversion used low density and unevenly distributed GPS data. Figures 5.4[a](v)- 5.6[b](v) depict scatter plots of

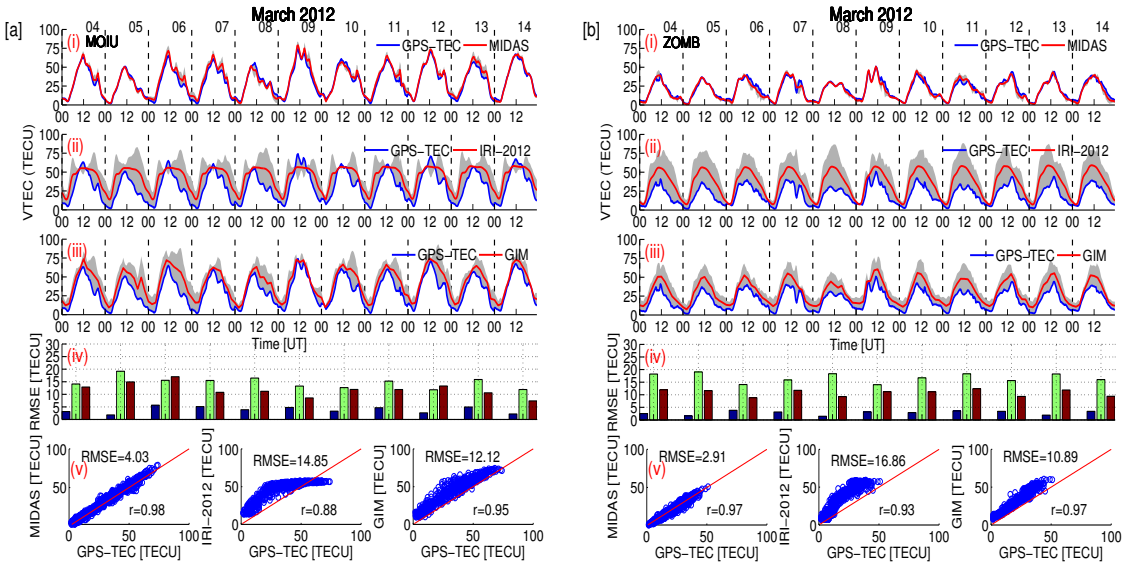

Figure 5.6: VTEC values derived from (i) MIDAS reconstruction , (ii) IRI-2012 model and (iii) GIM model over plotted with GPS-TEC near [a] MOIU and [b] ZOMB stations during 04-14 March 2012. The bar graphs depict the computed daily RMS errors for the GPS-TEC and MIDAS, IRI-2012 and GIM VTECs. The bottom panels (from left to right) show scatter plots with the computed RMSEs and correlation coefficients (r) of observation VTEC (GPS-TEC) and MIDAS, IRI-2012 model and GIM model estimates respectively. The gray patches show $\pm 2\sigma$ error bars around the MIDAS reconstruction, IRI-2012 and GIM diurnal VTECs.

the computed correlation coefficients and RMSEs for the validation period, of the observation VTEC (GPS-TEC) and (left panel) MIDAS, (middle panel) IRI-2012 model and (right panel) GIM model estimate respectively. MIDAS reconstructed TECs tracked the diurnal trends better than those of the models. This is evident from the higher correlation coefficients and least daily (shown in bar graphs) and cumulative RMSEs computed for the duration of the validation period. For the

duration of the validation period, the minimum r values computed for MIDAS, IRI-2012 and GIM TECs were 0.96 (at BSHM and ALWJ), 0.84 (at DEBK and ADIS) and 0.95 (at DEBK and MOIU) respectively. Similarly, the maximum r values computed for all the validation periods were 0.99 (at ADIS), 0.93 (at ZOMB) and 0.99 (at BSHM) for MIDAS, IRI-2012 and GIM TECs respectively. Moreover, the minimum cumulative RMSEs computed were 2.91 TECU (at ZOMB), 13.03 TECU (at ADIS) and 6.52 TECU (at ADIS), while the maximum cumulative RMSEs were 5.57 TECU (at ADIS), 23.14 TECU (at ALWJ) and 12.12 TECU (at MOIU) for MIDAS, IRI-2012 and GIM TEC estimates respectively. Similarly, Kassa et al. (2015) did 2D tomographic imaging with data from 10 GPS stations over the East African longitudes, bounded around the EIA region, and reported that the results showed good agreements with the GPS-derived TEC at a single station. However, the author's results were focused on the study of EIA phenomenon and no comparisons were made with other global and/or regional models such as IRI.

It has been shown that tomographic imaging captures the ionosphere better when an "adequate" and even distribution of GPS rays traverses the voxels of the reconstruction grids radially (Chartier et al., 2014; Spencer and Mitchell, 2007). Tomographic imaging results based on observations from a clustered network of ground stations could as equally capture "unrealistic" ionospheric structures as results based on a scarce distribution of ground stations (Yin et al., 2017; Chartier et al., 2014). Yin et al. (2017) recently reported the impact of the density of ground stations on tomographic imaging results and revealed that improvements could only be offered when receivers are within 150 km to 200 km distance from each other. Furthermore, the authors pointed out that more improvement could be achieved by the inclusion of multiple constellations besides the GPS constellation. In line with this, Chartier et al. (2014) noted that better imaging accuracy could be attained by the addition

of satellites rather than the addition of receivers, because the former would create additional ray paths. However, in Africa, the number of ground GPS receivers are still too small in number and too unevenly distributed to apply the suggestion. Moreover, data outages are common, adding to the unreliability of GNNS networks in the region.

Despite that, the tomographic results presented in this study suggest that the diurnal variation of TECs is captured with better accuracy during geomagnetically quiet and disturbed conditions over a region that is deprived of ground-based sounding instruments. It was shown that the short-time scale ionospheric structures in the diurnal TEC variations are better represented by MIDAS reconstruction than by the IRI-2012 and GIM TEC estimates of the mid-, low and equatorial ionosphere in the region of study. Also, although the region may gradually be populated by ground-based sensors in the near future for better and reliable characterization and monitoring of the ionosphere, this study offers a reliable technique to monitor the near real-time ionosphere over a wider part of the East African region, extending far to the mid-latitudes of both hemispheres.

5.1.3 Summary

This study investigated the performance of a tomographic reconstruction (MIDAS), over the understudied and data-scarce East African longitude sector for the period 04-14 March 2012. Moderate and strong geomagnetic storms occurred during this period which gave us the opportunity to evaluate the ability of the MIDAS reconstruction to reflect these conditions. The choice of the narrow longitude range between 30°E and 44°E and latitude range of 30°S and 36°N was mainly due to the presence of relatively better distribution of GPS stations in the region which is

spanned by the ionosphere of the mid- and low latitudes (both northern and southern hemispheres) and equator on the East African longitude sector. In order to determine the optimum conditions, multiple runs were undertaken in which options within MIDAS, such as the number of empirical orthogonal functions (EOFs) and the length of the sliding time windows of the inversion process, were varied. The outputs of the MIDAS test runs with the least RMSEs (Figure 4.2) with respect to the observation VTEC (GPS-TEC) and non-negative values (i.e. MIDAS-test6) were considered for final analysis. Then the tomographic results were compared with two global models: IRI-2012 and GIM. Furthermore, the VTEC derived from MIDAS, IRI-2012 and GIM were compared and validated against GPS-derived TEC (GPS-TEC) at selected validation GPS stations in different latitude regions.

In summary, MIDAS performed better than the IRI-2012 and GIM models in terms of capturing the diurnal trends, as well as the short temporal TEC structures which formed during both geomagnetically quiet and disturbed conditions over large latitudinal ranges. Moreover, MIDAS imaging showed no significant patterns with varying strength of geomagnetic storms (Figures 5.4[a](i,iv)- 5.6[b](i,iv)). Results showed that at worst the MIDAS VTEC errors amounted to RMSE of 5.57 TECU as opposed to the IRI-2012 VTEC (RMSE of 13.03 TECU) and GIM VTEC (RMSE of 6.52 TECU) at ADIS station over the duration of the validation period. On daily basis, the RMSEs computed for MIDAS ranged between 1.46 TECU and 9.41 TECU, whilst for the IRI-2012 and GIM models the computed RMSEs ranged between 9.37 TECU and 26.77 TECU and 3.58 TECU and 17.0 TECU respectively. Thus MIDAS performed better than the two models. Also, MIDAS performed best at the southern mid-latitude station of ZOMB, where the computed RMSE was 2.91 TECU, as opposed to the RMSEs of 16.86 TECU and 10.89 TECU for the IRI-2012 and GIM models respectively. Overall, the MIDAS results were more in line with

the observation VTEC, which had a minimum and maximum r of 0.96 and 0.99 and RMSE of 2.91 TECU and 5.57 TECU over all the test stations for the validation days (see Figures 5.4[a](v)- 5.6[b](v). Statistically, the results show a relatively better performance by GIM as compared to the IRI-2012 model, in terms of capturing the ionosphere diurnal variations over the mid-, low and equatorial latitudes of the region under study.

Chapter 6

Storm-time TEC reconstruction for eastern Africa: a comparative study

The complex nature of electrodynamic mechanisms in the low latitudes region makes it difficult to image the ionosphere over this region by means of inversion methods (Materassi and Mitchell, 2005). On the other hand, the Artificial Neural Network (ANN) technique (discussed in Section 4.4) has been intensively applied to modelling of some ionospheric parameters such as TEC (e.g., Tulunay et al., 2004; Leandro and Santos, 2007; Maruyama, 2008; Acharya et al., 2011; Ratnam et al., 2012) and ionospheric critical frequency of the F2 layer, foF_2 (e.g., Cander, 1998; Poole and McKinnell, 2000; McKinnell and Poole, 2004; Oyeyemi et al., 2006). In most of these works, the ANN predictions were to a great degree validated by the actual data. In addition, in comparison with IRI TEC predictions, results show that ANN is a more accurate predictor than IRI (e.g., Habarulema et al., 2010; Watthanasangmechai et al., 2012; Uwamahoro and Habarulema, 2015; Okoh et al., 2016).

Therefore, the aim of the work presented in this chapter was to statistically evaluate the capability of MIDAS to reconstruct the storm-time TEC over the African low

and mid-latitude regions, in comparison with ANN and IRI. The four geomagnetic storms selected for this evaluation are: 06 - 13 March 2012 and 18 - 24 February 2014 a high solar activity period; 16 - 22 March 2015, a descending phase of the solar cycle (moderate solar activity period); and 24 - 30 October 2016, a period of low solar activity. Table 6.1 shows the maximum K_p and minimum Dst values reached during the selected storm periods with storm classification based on the National Oceanic and Atmospheric Administration (NOAA) Space Weather Scales[1], and the classification by (Loewe and Prölss, 1997). MIDAS and the models were validated against observation GPS TEC, hereafter referred to as observations, which was derived using GPS TEC software discussed in Section 3.2.

Figure 6.1[a]-[d] shows the positions of the GPS ground receiver stations used for the inversion (shown in small red dots) and GPS ray traces at the ionospheric pierce point (IPP) altitude of 350 km. Also listed for each storm period, are the code names of the GPS receiver stations used for the inversion (magenta) and validation (blue). should be noted that data from GPS stations that were used for validation (listed in blue and shown with large magenta dots, Figure 6.1[a]-[d]) were not used for the inversion so as to make validation data independent.

For TEC modelling, individual ANN models were developed based on historical storm-time TEC derived from GPS measurements over TETE, MOIU, NAZR and SHEB stations representing low- and mid-latitudes; the geographic coordinates of these stations are shown in Table 6.2. Note that in cases where NAZR, TETE and SHEB stations had no data, the data from the closest stations to them were used instead (i.e. ADIS, ZOMB and DEBK, respectively) and their coordinates are also shown in Table 6.2. Due to the lack of data specifically for ANN model development,

[1]http://www.swpc.noaa.gov/noaa-scales-explanation

the African mid-latitude in the northern hemisphere was not part of this study. The coverage period of the data that was used to develop the ANN model is included in Table 6.2. More details on the ANN model can be found in Uwamahoro et al. (2017).

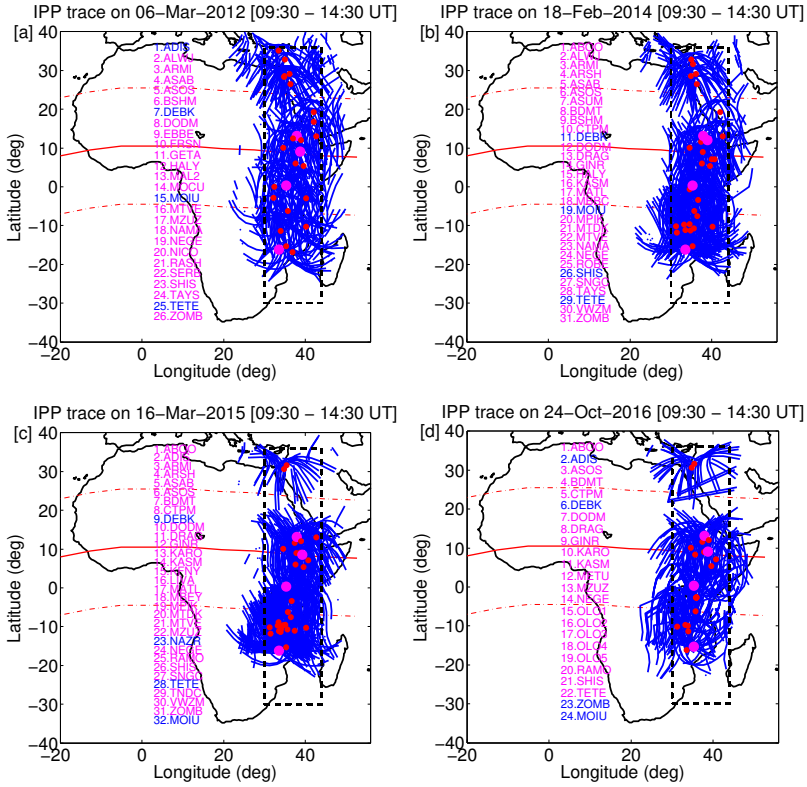

Figure 6.1: GPS ray traces at IPP altitudes for 5.5 hours' worth of observation data, on (a) 06 March 2012, (b) 18 February 2014, (c) 16 March 2015 and (d) 24 October 2016. The GPS ground station code names (written in magenta and marked with smaller red dots) from which usable observation data for the inversion was obtained are listed along with the IPPs. The stations of which the code names are written in blue and marked as bigger dots (magenta) were used for validation only. The central time window is 12:00 UT.

Table 6.1: Classification of the selected storm periods based on K_p (NOAA Space Weather Scales) and Dst (Loewe and Prölss, 1997).

Storm period	Highest K_p index	Lowest Dst index (nT)	Storm classification (Prolss)
06 - 13 Mar 2012	8	-145	Strong
18 - 24 Feb 2014	6	-116	Strong
16 - 22 Mar 2015	8	-223	Severe
24 - 30 Oct 2016	6	-64	Moderate

Table 6.2: Geographic (GLat & GLon) coordinates of the ground receiver stations used for the development of ANN models (shown with *) and validation. The data coverage period used for the ANN training are specified.

Station	Station ID	Country	GLat (°)	GLon (°)	Data coverage period
Debarek	DEBK	Ethiopia	13.15	37.89	2012 - 2016
Sheb*	SHEB	Eritrea	15.85	39.05	2004 - 2016
Nazret*	NAZR	Ethiopia	8.57	39.29	2007 - 2016
Addis Ababa	ADIS	Ethiopia	9.04	38.77	2010 - 2016
Moiu*	MOIU	Kenya	0.29	35.29	2008 - 2016
Tete*	TETE	Mozambique	-16.15	33.58	2011 - 2016
Zomba	ZOMB	Malawi	-15.38	35.33	2010 - 2015

6.1 Results and discussion

Figure 6.2 shows TEC results from MIDAS, and the ANN and IRI-2016 models, as well as observations for DEBK, ADIS, MOIU and TETE stations for the storm period of 06-13 March 2012. The last panel of Figure 6.2 shows the Dst and Kp indices which indicate a succession of storms with different intensities. For the entire storm period and for all stations, MIDAS reconstructed the storm-time TEC well and captured the short term features accurately, and better than the ANN and IRI models. The ANN model reconstructed TEC well for almost the entire storm period except, for some overestimations during daytime on 08 March 2012 for DEBK, ADIS and MOIU. However, the IRI model showed large daytime underestimations of GPS TEC for the entire storm period, specifically for DEBK and ADIS, while it estimated the TEC quite well, despite some discrepancies dominated by underestimations and overestimations for MOIU and TETE, respectively.

Figure 6.3 illustrates comparisons of the reconstructed TEC by MIDAS, ANN and IRI techniques with the observed TEC during the storm period of 18 - 24 February 2014, for DEBK, NAZR, MOIU and TETE. The 18 - 24 February 2014 storm period consisted of a sequence of storms, as indicated by $Kp \geqslant 4$ or $Dst \leqslant -50$ nT. It can be seen from Figure 6.3 shows that MIDAS TEC agrees quite well with observations for NAZR and TETE. However, noticeable discrepancies, mainly dominated by daytime overestimations, were seen for DEBK and MOIU. The capability of MIDAS to reproduce short-term variations of the observed TEC and following the TEC depletion observed over MOIU on 20 February 2014 is visible. The accuracy with which ANN estimated the observed TEC was high in spite of some clear deviations on 19 February 2014 for DEBK, NAZR and MOIU and on 23 February 2014 for DEBK. Except for TETE and MOIU on 20 February 2014 where the IRI model estimated

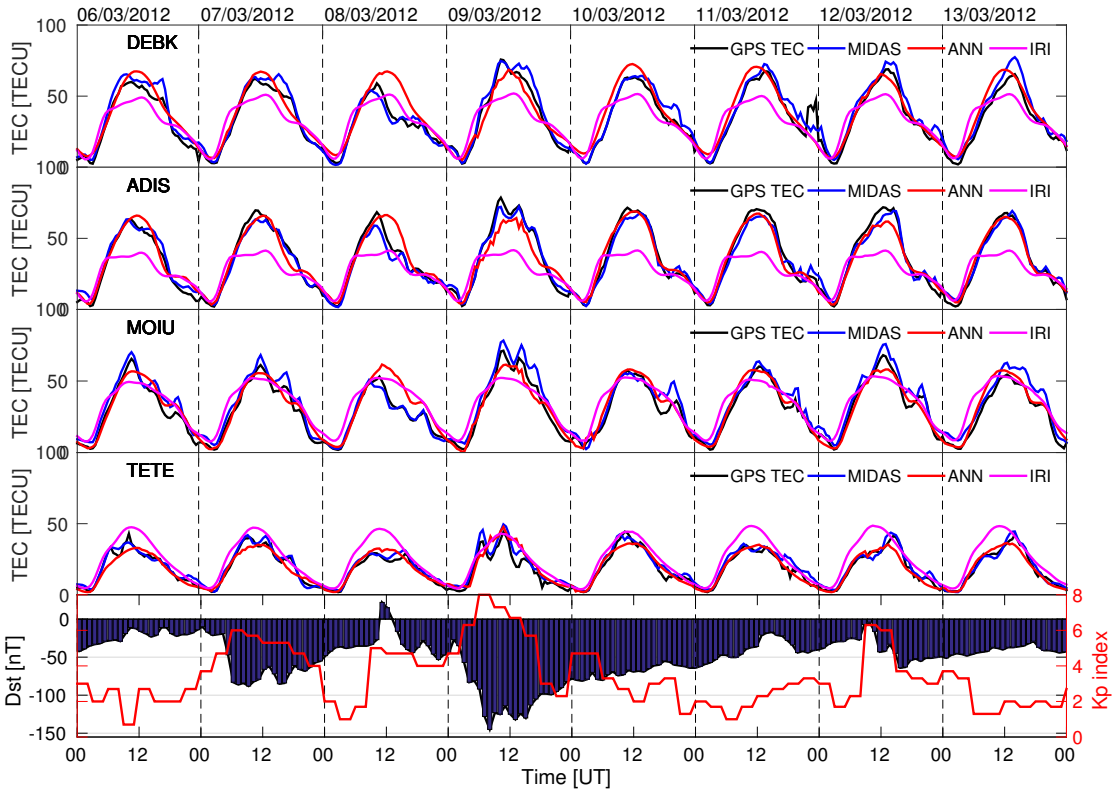

Figure 6.2: Comparison of the observed and reconstructed TEC for the storm period of 06 - 13 Mar 2012.

the storm-time TEC magnitude well, the IRI model underestimated the daytime TEC magnitude for the entire storm period.

Figure 6.4 presents the TEC estimates by MIDAS, ANN and IRI for DEBK, NAZR, MOIU and TETE, along with observations for the storm period of 16 - 22 March 2015. As indicated by Dst and Kp indices, the 16 - 22 March 2015 storm period consisted of one severe storm characterized by maximum Kp and minimum Dst values of about 8 and -223 nT respectively, observed during the main phase of the storm. The storm had a very long recovery phase that lasted about 5 days as shown by a Dst index below -50 nT for a prolonged time. Both MIDAS and

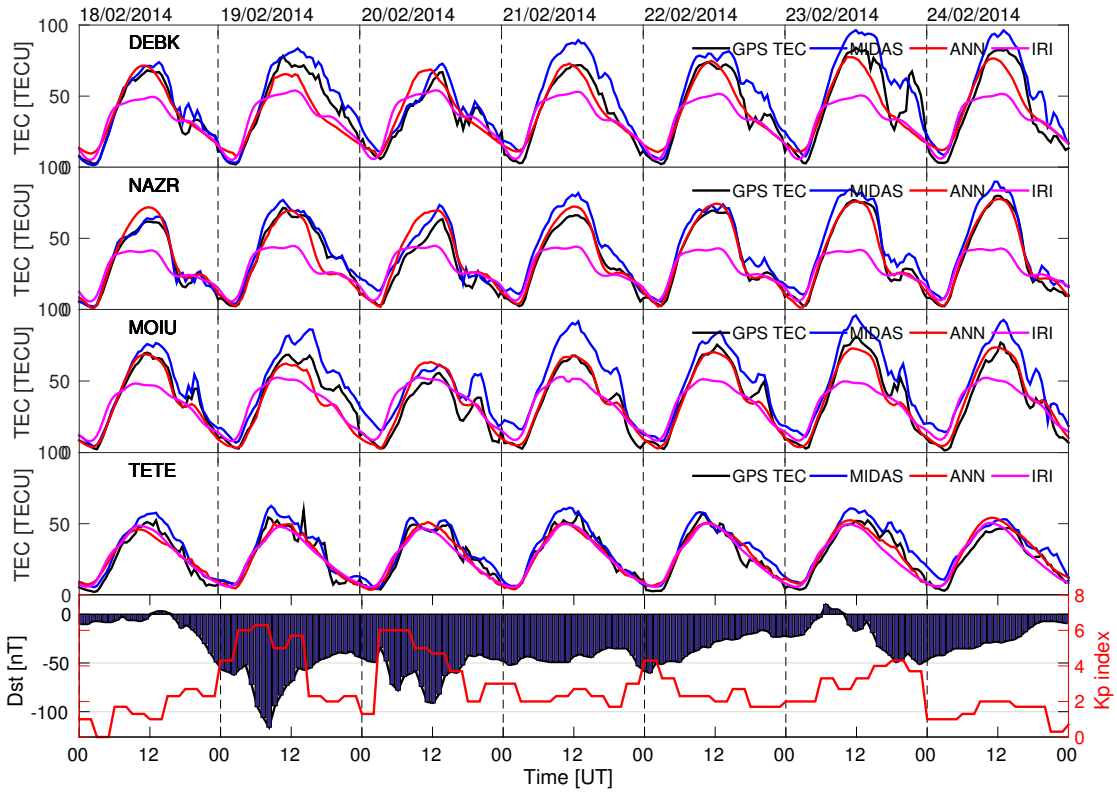

Figure 6.3: Comparison of the observed and reconstructed TEC for the storm period of 18 - 24 February 2014.

ANN reconstructed TEC quite well for all stations, although for some days, there were daytime overestimations and underestimations for DEBK and MOIU. TEC enhancement and double peak structures over TETE on 17 March 2015 were better captured by MIDAS than by ANN and IRI. The IRI model underestimated TEC during the daytime for the entire storm period for DEBK and NAZR and some days for MOIU, while for TETE, there were relatively small overestimations for some days.

Figure 6.5 presents TEC as reconstructed by the MIDAS, ANN and IRI techniques,

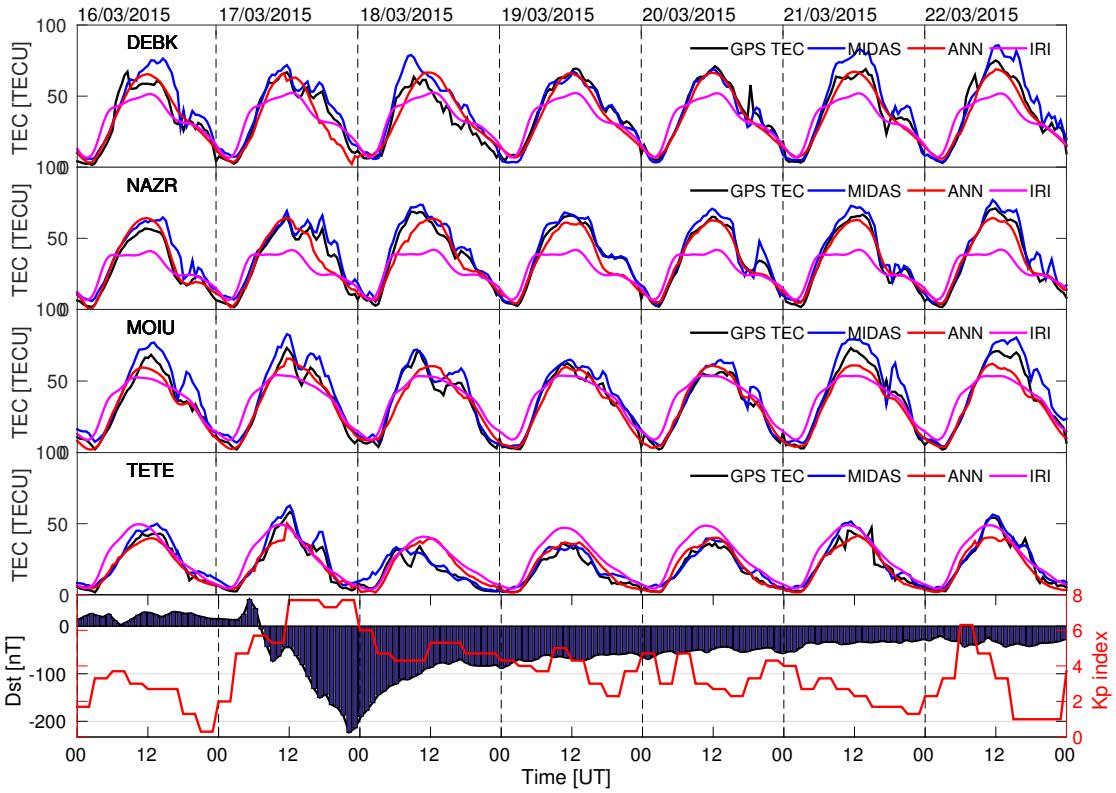

Figure 6.4: Comparison of the observed and reconstructed TEC for the storm period of 16 - 22 March 2015.

along with observations, for a sequence of moderate geomagnetic storms that occurred within the storm period of 24 - 30 October 2016. The presented results are for DEBK, ADIS, MOIU and ZOMB stations. For this storm period MIDAS makes accurate estimations of TEC for DEBK, MOIU and ZOMB, except for 30 October 2016 where daytime overestimation is observed. The TEC depletion on 26 October 2016 over DEBK, MOIU and ZOMB was also well captured by MIDAS. However, for ADIS, MIDAS underestimated daytime TEC for almost the entire storm period. In comparison, ANN also estimated the magnitude of TEC quiet well for DEBK and MOIU, but failed to capture the depletion on 26 October 2016. For ADIS and ZOMB, ANN also underestimated daytime TEC for almost the entire storm

period, however, it performed better in ADIS and worse in ZOMB than MIDAS. Except for the TEC depletion not seen by the IRI model over the four stations on 26 October 2016, for other days, the IRI predictions were in good agreement with observations specifically for DEBK and MOIU. However, for ADIS, daytime TEC magnitude was underestimated for some days, while for ZOMB the TEC magnitude was overestimated for the whole storm period. The common characteristics of the three methods used for storm-time TEC reconstructions/predictions are their high accuracy in early morning and sometimes around mid-night hours, and where over- or underestimations exist, these are generally observed during daytime.

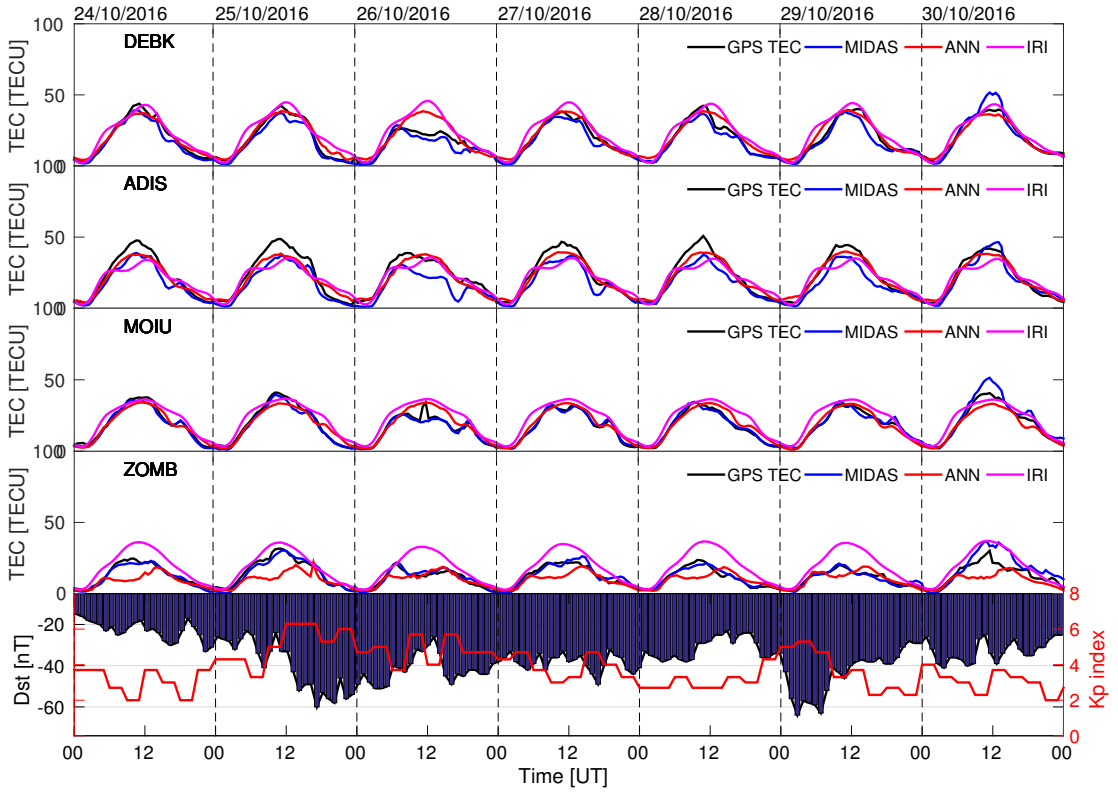

Figure 6.5: Comparison of the observed and reconstructed TEC for the storm period of 24 - 30 October 2016.

In order to determine which of the three techniques/models performs best in reconstructing/predicting the storm-time TEC over the different African latitude regions, a statistical analysis was done based on the calculation of the mean absolute error (MAE) and the calculation of Pearson's correlation coefficient for the observed and reconstructed TEC. Starting with the definition of the absolute error (AE) (Habarulema et al., 2007; Leandro and Santos, 2007):

$$AE = |TEC_{rec} - TEC_{obs}|, \tag{6.1}$$

MAE is given by (Mitchell and Spencer, 2003; Willmott and Matsuura, 2005)

$$MAE = \frac{1}{N}\sum_{i=1}^{N}|TEC_{rec} - TEC_{obs}| \tag{6.2}$$

where N is the number of observations. MAE represents the average of the vertical distances between the observed and predicted quantities and has been proven to be a good parameter to use over the RMSE in assessing the performance of a model (Willmott and Matsuura, 2005). Figure 6.6 shows the calculated MAE and correlation coefficient values for all validation storm periods. For the storm periods of 06 - 13 March 2012 and 24 - 30 October 2016, generally smaller values of MAE for MIDAS reveal that, on average, MIDAS reconstructed storm-time TEC better than the ANN and IRI models. By contrast, for the 18 - 24 February 2014 and 16 - 22 March 2015 storm periods, ANN was more accurate, on average. Except for TETE where MAE values for the IRI model are comparable with the values obtained for ANN, specifically for the storm period of 18 - 24 February 2014, MAE values for the IRI model are higher for all other cases. This indicates that IRI model is not as accurate as the MIDAS and ANN techniques in making storm-time TEC reconstructions. A similar conclusion was drawn in previous works that compared MIDAS

reconstructions with IRI predictions (e.g., Chartier et al., 2012; Giday et al., 2015), and ANN estimations with IRI predictions (e.g., Habarulema et al., 2007, 2009; Watthanasangmechai et al., 2012; Okoh et al., 2016).

The underestimation of TEC by the IRI model can be attributed to the difference in altitude ranges over which the TEC is estimated (Kenpankho et al., 2011; Chartier et al., 2012; Habarulema and Ssessanga, 2017). Since the IRI model generates TEC for the altitude range of 60 - 2000 km (while ANN and GPS TEC calculate TEC up to the height of GPS satellites, i.e. ∼20200 km), the model does not fully include the contribution of the plasmasphere. Due to systematic limitations of MIDAS (including the version used in this study) reconstruction grid does not extend to plasmaspheric altitudes, having a maximum altitude of ∼ 2000 km. Hence, MIDAS works on the basis that all the measured GPS slant TEC is accumulated within the reconstruction grid, and so it is likely that an unknown amount of plasmaspheric TEC is redistributed at ionospheric altitudes in the reconstructions Kinrade (2013). However, Jayawardena et al. (2016) adapted MIDAS to image features/trends of the topside ionosphere-plasmasphere by using GPS phase-based TEC measurements. The amount of data used for training and the choice of the number of hidden nodes also influenced the modelling results of the ANN model. The performance of MIDAS could be improved by ingesting more even and dense observation data into the inversion. However, with the available input data, it was observed that MIDAS captured short-term features and followed TEC enhancements and depletions during geomagnetic storms better than IRI models but comparable to ANN.

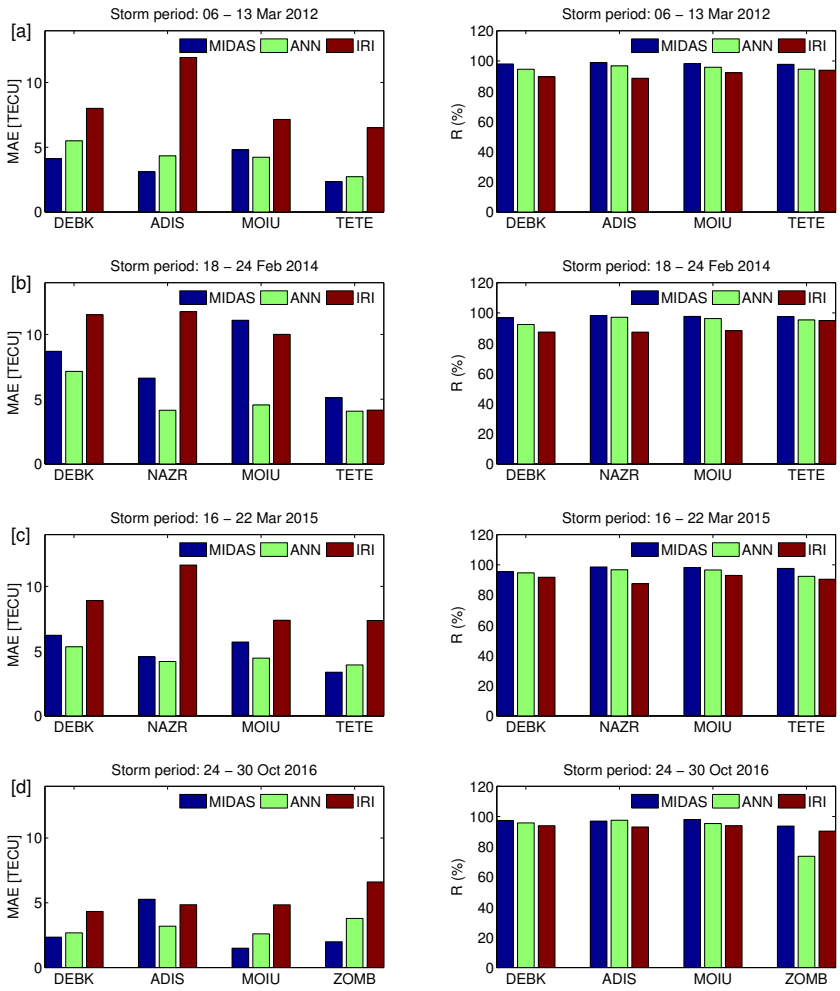

Figure 6.6: MAE and correlation between the observed and reconstructed/predicted TEC by MIDAS, ANN and IRI.

Figure 6.6 shows that values of MAE were generally relatively high for the low-latitude stations (DEBK, NAZR, ADIS, MOIU) compared to the mid-latitude stations (TETE, ZOMB), except for the 24-30 October 2016 storm period (ANN and IRI). Table 6.3 shows the average MAE values for the four storm periods over each location, indicating high values for low latitudes. The reconstruction techniques used in this work estimated TEC better for the mid-latitudes than the low latitudes. This agrees well with what was previously reported about the performance

of IRI (e.g., Kumar et al., 2015) and MIDAS (e.g., Chartier et al., 2014) in the low and mid-latitudes. The difficulty in reconstructing/modelling the low latitude ionosphere has been frequently reported (e.g., Materassi and Mitchell, 2005; Adewale et al., 2011; Kenpankho et al., 2011; Panda et al., 2015). Table 6.3 also shows that while MIDAS performs much better than IRI, it performs worse than ANN, since generally ANN's average MAE is less than that of MIDAS for all stations except the mid-latitude stations (TETE/ZOMB). Overall, high values of MAE for the low latitudes compared to the mid-latitude are likely due to higher TEC gradients caused by the equatorial ionisation anomaly as a result of the fountain effect. The influence of high TEC variability due to the fountain effect on TEC modelling/reconstruction has been reported as the major cause of the difficulties in modelling the low latitude ionosphere. This observation was made by Chartier et al. (2014) in his efforts to tomographically image the African ionosphere during geomagnetically quiet conditions, and by Panda et al. (2015) for TEC reconstruction of the low latitudes of the Indian sector by means of the IRI model. It can thus be concluded that TEC reconstruction is more difficult for the low than middle latitudes, and this agrees with what has been previously reported (e.g. Chartier et al., 2014; Kumar et al., 2015).

Table 6.3: Average MAE computed over the four storm period predictions considered for validation.

	DEBK	NAZR/ADIS	MOIU	TETE/ZOMB
MIDAS	5.35	4.89	5.78	3.20
ANN	5.16	3.96	3.96	3.63
IRI	8.19	10.05	7.35	6.16

To evaluate how accurately one model performs with respect to another, the Percentage Improvement (PI) was computed according to the Equation 6.3(Muslim et al., 2015)

$$PI = \frac{MAE_1^{av} - MAE_2^{av}}{MAE_2^{av}} \times 100\% \tag{6.3}$$

where MAE_1^{av} and MAE_2^{av} are the average of MAE values for model 1 (in this case MIDAS) and model 2 (in this case ANN), respectively, as presented in Table 6.3. Equation 6.3 indicates by what percentage model 2 (ANN) performs better than model 1 (MIDAS) or vice-versa. This comparison was made only for MIDAS and ANN, since the former was compared with IRI in Chapter 5. For the storm period predictions considered for validation, it was found that, on average, the ANN model performs 3.69 %, 23.48 %, 45.96% better than MIDAS for DEBK, NAZR/ADIS, MOIU, respectively. The average PI of 24.37 % for the three locations showed that ANN predicts more accurately in the low latitude than MIDAS. On other hand, MIDAS performed better for the mid-latitude station TETE/ZOMB by 13.44 % compared to the ANN model. The high accuracy of ANN model in TEC modelling has previously been reported for both low (e.g., Acharya et al., 2011; Watthanasangmechai et al., 2012) and mid-latitude regions (e.g., Huang and Yuan, 2014). For all stations of which the data was used for validation, the average MAE values for MIDAS, ANN and IRI, were 4.81, 4.18 and 7.94 TECU respectively. This confirms that overall, MIDAS and ANN provides comparable results, and are both better than the IRI model for storm-time TEC reconstruction.

For the three techniques used to reconstruct storm-time TEC, high correlation coefficients (between 73 - 99 %) were found. In the context of this study, high correlation

coefficients confirm good performance of MIDAS, ANN and IRI in capturing the general trend of the observed TEC. Over all stations, the highest correlation coefficients found for MIDAS indicate that there is a stronger positive linear relationship between observations and MIDAS estimations, compared to the other techniques. It can therefore be concluded that MIDAS reconstructs the short-term features and follows the storm-time TEC dynamics more accurately than the IRI and ANN models. The good performance of MIDAS during disturbed conditions was noticed and reported by (Yin et al., 2004) for reconstruction of the electron density over the USA.

The performance of MIDAS, ANN and IRI did not seem to depend on the storm intensity, as can be seen in Figure 6.6. For example, MIDAS reconstructs the storm-time TEC for the storm period 16 - 22 Mar 2015 (minimum Dst of -223 nT) better than it does for the 18 - 24 February 2014 storm period (minimum Dst of -116 nT).

6.2 Summary

The presented work in this section evaluated the capability of MIDAS, ANN and IRI to reconstruct storm-time TEC for low and mid-latitude regions of the eastern African sector. Based on geomagnetically disturbed conditions only, this study compared MIDAS, ANN and IRI-2016 TEC reconstructions, and validated the results with the real GPS TEC observations. The main findings of this study are summarized below:

- MIDAS and ANN provided comparable results in reconstructing the storm-time TEC over different latitudes of Africa, with MAE values of 4.81 and 4.18 TECU, respectively.

- On average, ANN performed 24.37 % better than MIDAS in estimating storm-time TEC for the low-latitude ionosphere, while the accuracy of MIDAS was 13.44 % higher than than that of ANN for the mid-latitudes.
- MIDAS captured short-term variations of TEC very well and followed enhancements and depletions during geomagnetic storms comparatively better than ANN.
- Both MIDAS and the ANN model provide more accurate storm-time TEC reconstruction results than the IRI model in the African low- and mid-latitude regions.

On the basis of MAE, storm-time TEC reconstruction is more difficult for the low-latitude than mid-latitude ionosphere. The fountain effect and the resulting higher TEC gradients over the low-latitude ionosphere are likely to be the cause of the difficulty in reconstructing TEC over this region.

MIDAS, ANN and IRI accuracies did not depend on the storm intensity. Although based on a few storm cases, MIDAS reconstructed storm-time TEC more accurately for severe storms (e.g., 16 - 22 March 2015) than it did for strong storms (e.g., 18 - 24 February 2014).

Chapter 7

Challenges of imaging small-scale ionospheric structures

Most ionospheric tomography techniques, including MIDAS, use regularisation factors which apply a smoothing in time and space. MIDAS's initial estimates of electron density are iteratively refined by least squares minimisation of a regularised cost function, which promotes linear gradients in space (horizontally) and time Chartier (2013). Therefore, by adjusting the rate of change of the horizontal gradient by means of the manipulation of the regularisation parameter (λ), users can either force a smooth ionospheric reconstruction (large λ) or relax the horizontal conditions in order to better extract finer spatial structuring. In line with this, Kinrade (2013) demonstrated that by varying the values of the levels of the horizontal regularisation constraint (λ), different ionospheric structures can be captured. That is, a strongly constrained reconstruction (e.g. $\lambda = 10.0$) renders a smooth ionosphere. The default MIDAS regularisation setting (i.e. $\lambda = 1.0$), which was also used to produce the results in Chapters 5 and 6, allows a stable reconstruction with good resolution of TEC, when good data coverage is available. Similarly, when the reconstruction is loosely constrained (e.g. $\lambda = 0.1$), the regularisation effect becomes weaker. It was observed that, while relaxing the horizontal conditions (i.e. loosely

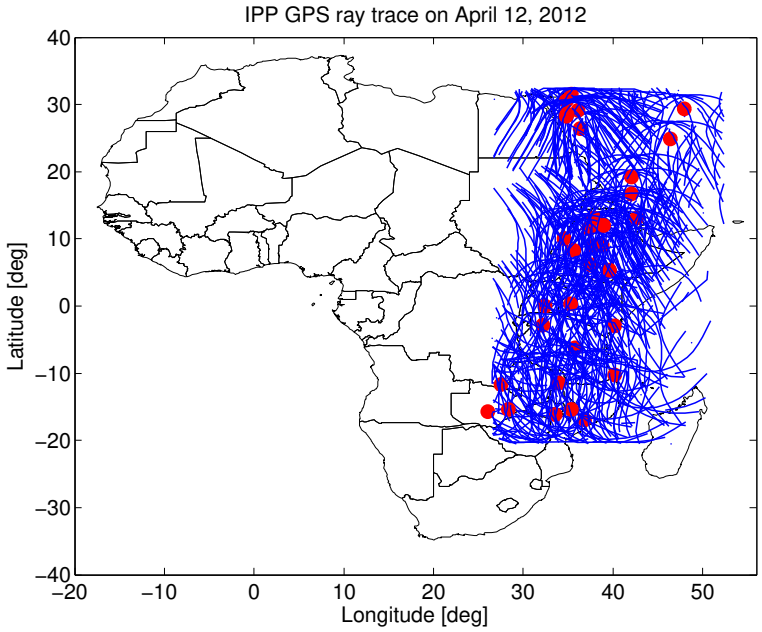

Figure 7.1: GPS stations used (red dots) in the inversion and the GPS ray paths at IPP altitudes on 12 April 2012.

constrained) may allow for extraction of finer spatial structures, the solution might eventually become unstable, leading to potential false artefacts. However, when using this method data coverage and geomagnetic conditions should be taken into account.

Although a cautiously implemented regularisation can produce reasonable results, it can also appear smooth and less defined thereby, loosing the desired information about the finer structures in the ionosphere. These effects are even aggravated in regions of sharp TEC gradients such as in the low- and equatorial latitude ionosphere (Muella et al., 2011; Kinrade, 2013). High-resolution and loosely constrained MIDAS reconstruction (i.e. $\lambda = 0.1$) was performed in an attempt to capture small-scale structures (such as EPBs) and irregularities on 12 April 2012, as observed from C/NOFS and computed in ROT/ROTI. The inversion was made using data as shown

in Figure 7.1. Figure 7.2 presents MIDAS VTEC (shown in dashed black lines) and GPS-TEC derived observations (colour-coded for all pseudo random noises (PRN's)) at four GPS stations (ALWJ, DEBK, ADIS and MOIU) during the period of intense EPB activity as observed by the C/NOFS satellite (Figure 7.3). The MIDAS VTEC displayed significant discrepancies compared to the observation VTEC, which was not the case when a proper regularisation parameter was used to produce the results as discussed in Chapters 5 and 6.

High-resolution reconstruction results in more erroneous solutions, because the tomographic problem becomes highly underdetermined. Although the smoothness due to the regularization is an important parameter in regions where data are not available, it is not capable of imaging ionospheric structures which occur in different positions and with different scales or sizes. Therefore, recent studies such as one by Panicciari et al. (2015), focused on developing computerized ionospheric tomography algorithms that could potentially resolve small-scale structures in regions with good data coverage. That study tried to incorporate wavelet basis functions, because wavelets are able to represent structures of different scale and position efficiently, by means of a method known as Multi Resolution Analysis (MRA). The theory of sparse regularisation in wavelet analysis allows the usage of a small number of basis functions with minimum loss of information which makes it preferable in regions of unevenly distributed ground instruments.

While current GPS tomographic imaging methods can provide useful estimates of electron density in regions inherently sparse in wide-area observations, they are incapable to image directly the small-scale ionospheric structures, such as ionospheric irregularities (Kinrade, 2013), as shown in Figure 7.2. Although tomography cannot directly provide the spatial resolution required to view the small-scale structures,

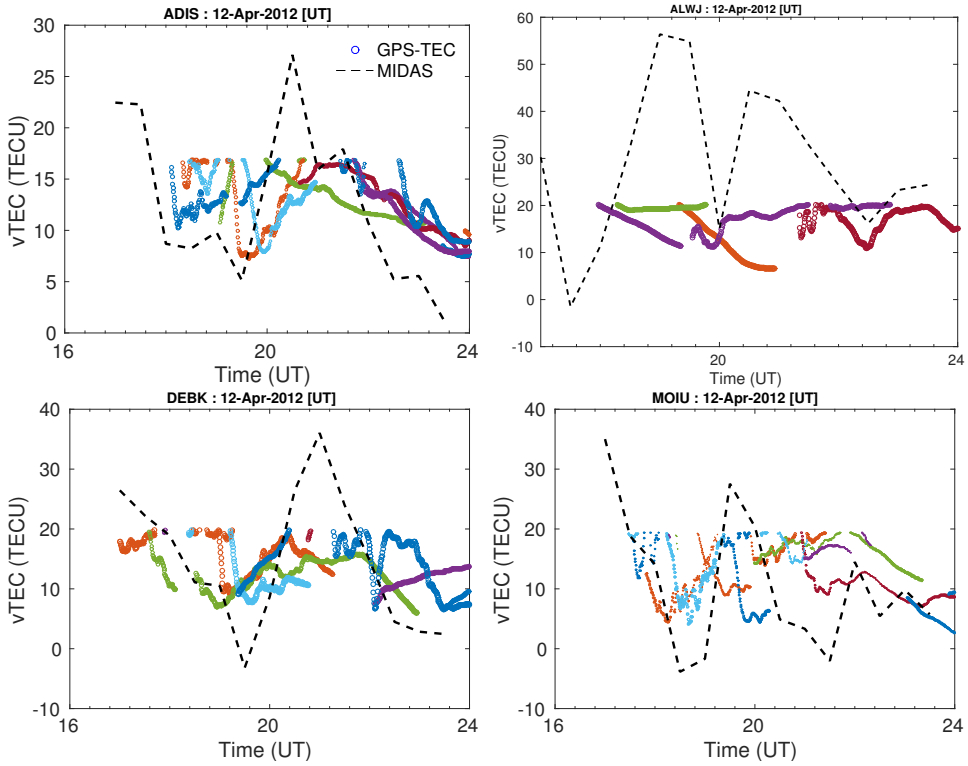

Figure 7.2: VTEC of MIDAS reconstructed data (shown in dashed black lines) and GPS-TEC observation (colour-coded for PRN's) for 12 April 2012 at ADIS, ALWJ, DEBK, and MOIU stations. The MIDAS inversion was done by means of the relaxed (loose) regularisation factor as it allows the inversion to capture unusual ionospheric structures (Kinrade, 2013).

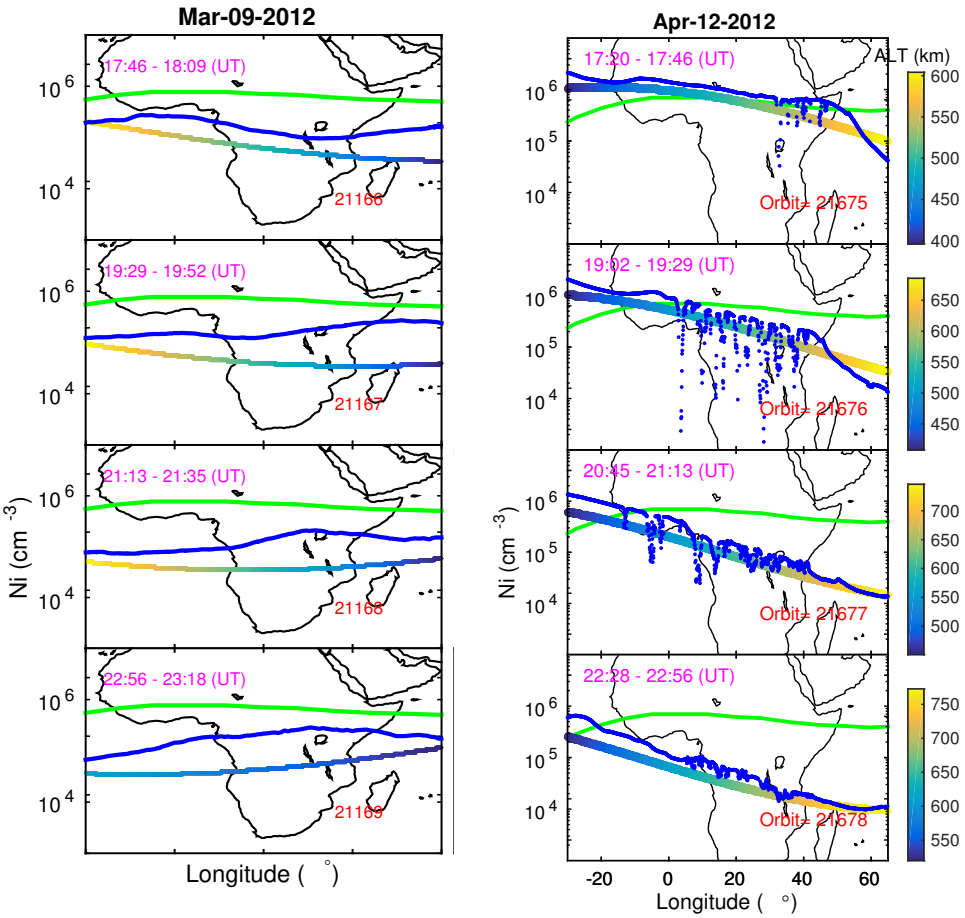

Figure 7.3: Plasma density measurements by the C/NOFS satellite on 9 March 2012 (left panel) and on 12 April 2012 (right panel). Intense EPB activity was observed for 12 April 2012.

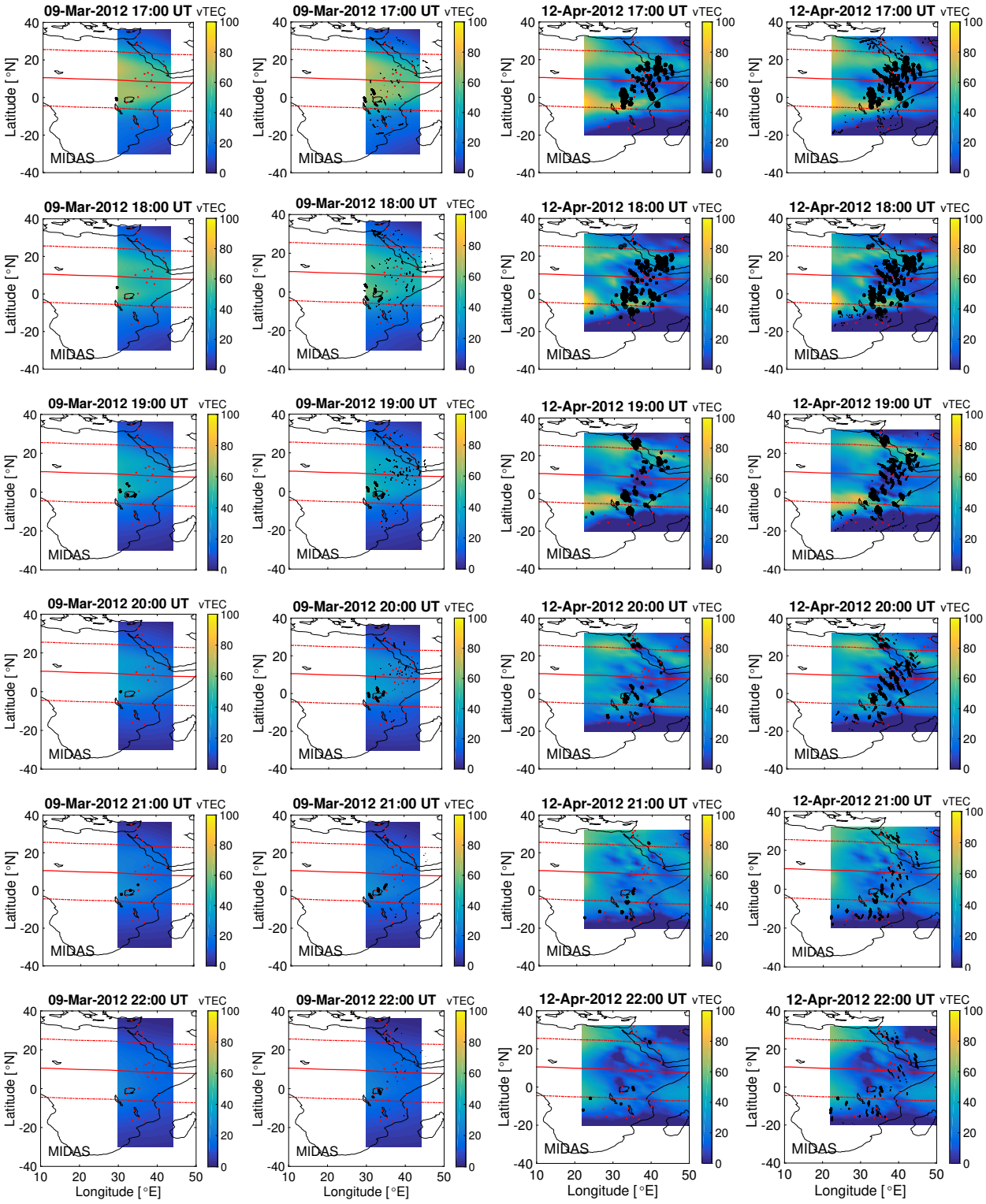

Figure 7.4: Caption found on next page.

Figure 7.4: ROTI values (black dots) embedded over MIDAS TEC maps during periods of high EPB activity for 12 April 2012 and on 09 March 2012 when EPBs were absent. ROTI values $\geqslant$ 0.5 TECU/min, considered to be scintillation causing irregularities (first and third column panels) and with the background ionospheric irregularities included (i.e. ROTI $<$ 0.5 TEC/min shown in the second and fourth column panels), Mungufeni et al. (2016) are displayed as well. The sizes of the black dots are scaled with the magnitude of the ROTI values (i.e. larger dots indicate higher ROTI values).

the images are useful to identify instances of ionospheric storm features and scintillation structures. Figure 7.4 displays MIDAS TEC maps along with the embedded computed ROTI indices during the storms of 09 March and 12 April 2012. This figure shows that, while the background ionospheric irregularities seem to be persistent on both storm days (black dots on the second and fourth column panels), the severe ionospheric irregularities were mainly observed on 12 April 2012 (first and third column panels), in agreement with C/NOFS observations shown in Figure 7.3. Note that ROTI values $\geqslant$ 0.5 TEC/min embedded on TEC maps of the first and third panels are considered to be scintillation causing ionospheric irregularities, while the values less than that (shown in second and fourth panels) are background ionospheric irregularities (Tanna et al., 2013; Mungufeni et al., 2016).

In the African sector, the spatial distribution of GPS receivers is too limiting to investigate the capability of MIDAS to image such small-scale structures. Therefore, the current version MIDAS was not able to reconstruct EPBs and irregularities seen in C/NOFS and GPS measurements. In fact, Panicciari et al. (2015) recently

upgraded/re-engineered the current MIDAS version in an attempt to capture small-scale ionospheric structures. However, a similar upgrade to improve MIDAS' performance in capturing small-scale structures was not within the scope of this study. Therefore, in order to study the evolution and electrodynamics of EPBs and irregularities during geomagnetic storms, ground- and space-based instruments will be used instead of MIDAS.

Chapter 8

Study of EPBs over east African longitude sector

The wide range of ionospheric irregularities (from 10 cm to 1000 km) within the depletions of plasma disrupts communications and navigation systems in a broad latitudinal band (±20 degrees) surrounding the geomagnetic equator by scattering radio wave signals that pass through them (Portillo et al., 2008; Paznukhov et al., 2012), thus are still the subject of space weather study. In spite of the fact that the African equatorial region has the largest ground footprint along the geomagnetic equator, it has not been well studied due to the absence of adequate ground-based instruments. (Paznukhov et al., 2012; Ngwira et al., 2013a). Nevertheless, studies on this region, both statistical, such as by Yizengaw et al. (2013) and Mungufeni et al. (2016) and/or case studies, such as by Paznukhov et al. (2012), Ngwira et al. (2013b,a) and Olwendo et al. (2013), have pointed out that the ionosphere over the African equatorial region displays unique irregularity patterns when compared to the other sections of the globe and hence needs more exploration. For instance, it is noted that the two major factors for the presence of Spread-F (EPB activity) occurrence are the variations in the linear growth rate of the generalized R-T instability and the presence of seed perturbations (Paznukhov et al., 2012, and the

references therein). The seed perturbations are attributed to the presence of medium scale gravity waves. However, in the equatorial region the seeding conditions for the gravity waves are determined by the position of the intercontinental convergence zone (ITCZ) as suggested by Tsunoda (2010). Moreover, it has been reported that it is unlikely that there is a significant difference in the ICTZ location in a relatively small region (e.g. between west and east Africa), thus seeding conditions could not significantly differ on such a scale (Paznukhov et al., 2012). Therefore, the differences in observed EPB activity between the west and the east African longitude sectors could be attributed to the potential differences in the ionospheric electrodynamic processes as suggested by Yizengaw and Moldwin (2009) and Paznukhov et al. (2012). It has also been reported that, in Africa, especially in the east African region, the shallower EPBs are observed practically all year long, because it is located near the boundary of the 4-cell non-migrating tidal structures (refer to Anderson et al. (2009) and Paznukhov et al. (2012) for more details).

This chapter aims to investigate the effects of three moderate geomagnetic conditions on 5 and 13 April, and 09 July 2012 on the evolution of equatorial plasma bubbles (EPBs) and/or ionospheric irregularities during their occurrence over the eastern African equatorial sector, by means of observation by space- and ground-based instruments. Where possible the quiet day(s) before and after these geomagnetic storms were used for comparison; alternatively the nearest quiet day was used. Although the MIDAS technique and ANN model provide good results for large scale density structures as shown in Chapters 5 and 6, respectively, they produce very smoothed EIA. This is not ideal in this study since it is important to obtain a detailed EIA and extract the peak-to-trough ratios to assess the link between the EIA and plasma bubbles. Therefore for this purpose, in this chapter GPS-TEC from 44 GPS receivers in the relatively well-populated east African region (red dots in

Figure 8.1) were used instead to analyze the latitudinal and temporal variations in 2D TEC maps for the periods of study. Note that a few stations in the middle east were used to supplement the rather sparse GPS receivers on the northern side of the equator compared to the south. ROT in TECU/min computed for NAMA and MAL2 (marked as magenta diamonds in Figure 8.1) using Equation 3.22 (see Section 3.2 was used as a measure of TEC fluctuation associated with ionospheric irregularities observed in C/NOFS data. An elevation cut-off of 30° was considered to minimize the multi-path effects in the computed GPS TEC data used for this study. All three storms in this study were driven by either full or partial halo CME events, the speeds of which ranged from 244 km/s to 1828 km/s.

8.1 Results

Figures 8.2- 8.3 and 8.5 which show results for the storm under consideration are arranged as follows: (a) (i) OMNI solar wind bulk speed (Vsw), (ii) IMF Bz, (iii) the AE index and (iv) the geomagnetic SYM-H; (b)(i) TEC maps and (ii) the ΔH values; (c) TEC values extracted for around 18:00 UT from TEC maps; (d) PLP plasma density; and (e) and (f) ROT (i.e. TEC fluctuations) at NAMA and MAL2 stations respectively. Note that LT = UT + 3 in the East African region under study.

8.1.1 Moderate geomagnetic storm on 5 April 2012

Figure 8.2(a)(ii) shows a sudden IMF Bz southward turning at around 21:00 UT on 4 April 2012 which persisted until about 14:20 UT on 5 April 2012. This sudden Bz southward turning led to a moderate storm, reaching a minimum SYM-H of -67 nT

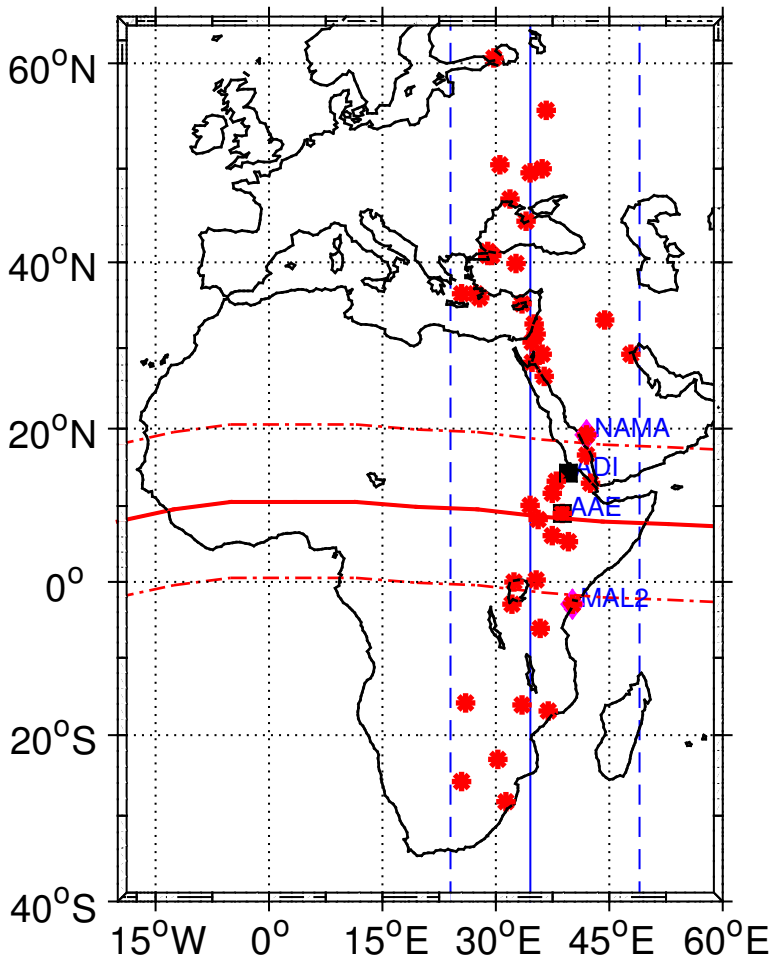

Figure 8.1: Geographical locations of the selected GPS receiver stations (marked as red dots and NAMA and MAL2 in magenta diamonds) and intermagnet magnetometer station (AAE) and AMBER station (ADI), in black boxes, from which the data used in this study were obtained. The two dashed vertical lines indicate longitude boundaries at 24° E and 49° E and the solid line is the mean longitude (∼35°) of the stations used. The red horizontal lines indicate the dip equator (solid) and ±10 degrees north and south of the dip equator (dashed).

around 08:00 UT before it recovered fully on 6 April 2012. The AE index showed an increase well above 1000 nT, whereas the solar wind speed did not show any

enhancement during this period.

Figure 8.2(d) shows the PLP plasma density on 3, 5 and 6 April 2012 during the post-sunset period (no C/NOFS data for 4 April 2012). Compared to the quiet days prior to and post the moderate geomagnetic storm (i.e. 3 and 6 April respectively), the plasma density measurements show that the EPBs were fully suppressed on the evening of 5 April 2012, which falls within the recovery phase of the storm and the IMF Bz turned northward approximately between 14:20-21:30 UT. It should also be noted that EPB activity was very low on 3 April 2012. However, more intense EPBs were observed during the geomagnetic quiet day on 6 April 2012, when the geomagnetic storm had fully recovered and the IMF Bz was northward for most of this day.

Figures 8.2(e) and 8.2(f) present the TEC fluctuations (i.e. ROT values) as computed for both NAMA and MAL2 stations for the same days and time periods (i.e. post-sunset) as for the C/NOFS observations in Figure 8.2(d). Both NAMA and MAL2 stations did not observe ionospheric irregularities during 3-5 April 2012. However, both stations showed significant TEC fluctuation for 6 April, and which was more pronounced at MAL2. In this case, the ground measurements supported the satellite observations, on the eastern side in particular, in that there were no irregularities on the day of the storm and the quiet days prior.

Figure 8.2(b)(i) presents the latitudinal and temporal variations of TEC over a narrow longitude sector over the east African equatorial ionosphere (marked by blue vertical dashed lines in Figure 8.1). The red vertical dashed lines in Figure 8.2(b)(i) correspond to the periods of IMF Bz southward turnings indicated in Figure 8.2(a). The northern and southern crests of EIA were distinct on 4 and 6 April, while they

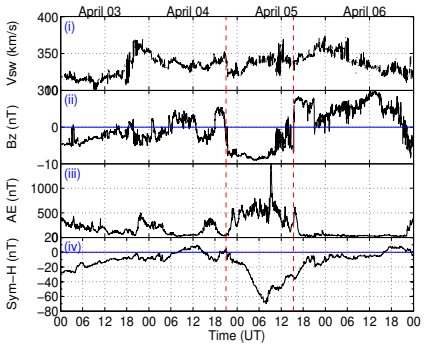

(a) Solar wind and geomagnetic indices indicators

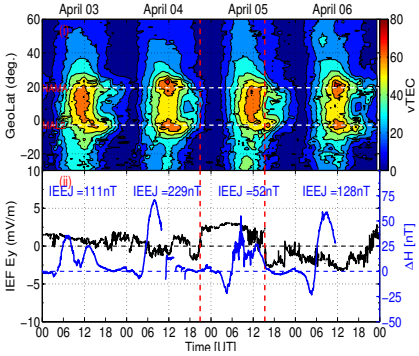

(b) TEC map, ΔH and IEF Ey values

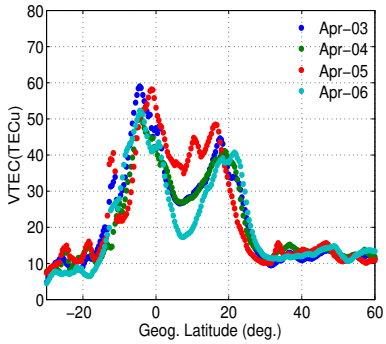

(c) VTEC values

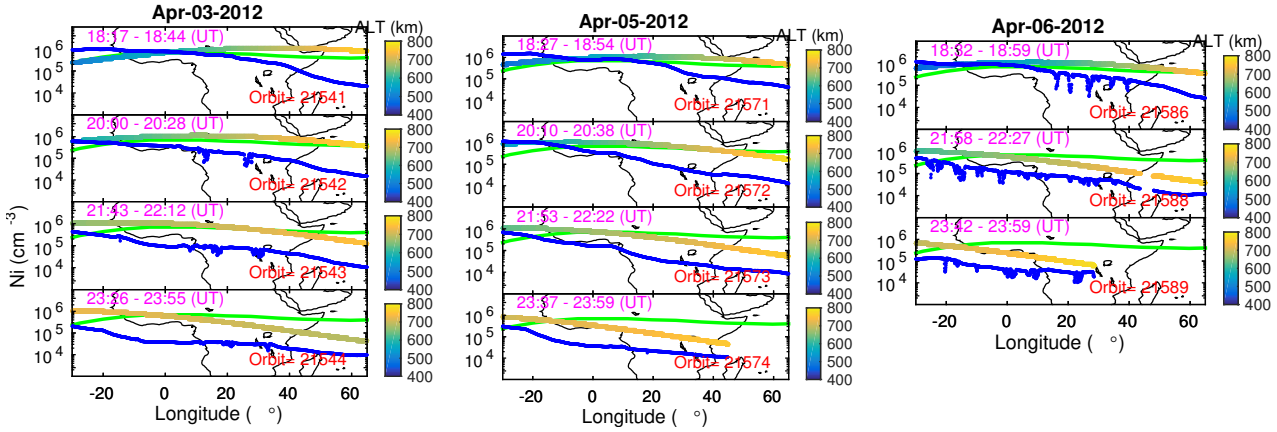

(d) C/NOFS EPBs observations

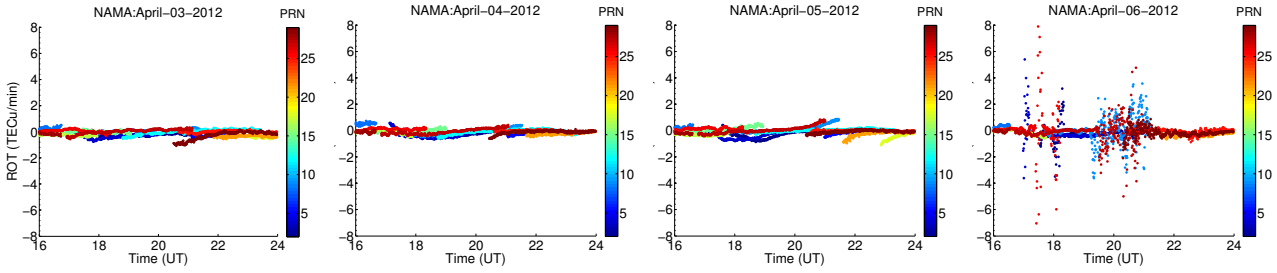

(e) ROT fluctuations at NAMA station

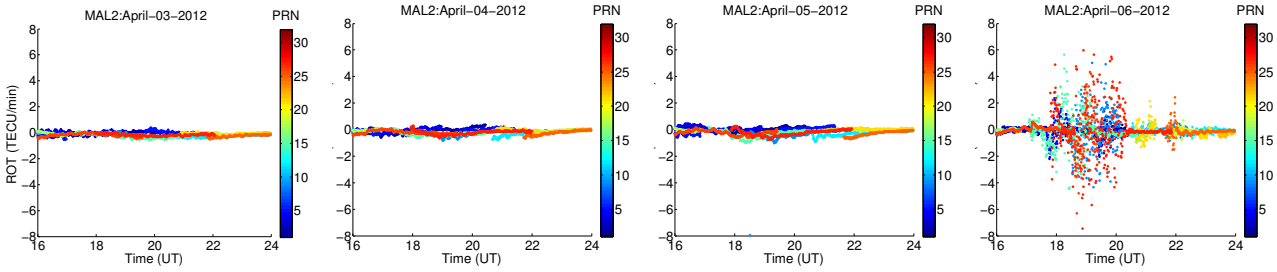

(f) ROT fluctuations at MAL2 station

Figure 8.2: Caption found on next page.

Figure 8.2: Presented in these figures are: (a) one-minute averaged solar wind conditions and geomagnetic indices, (b) (i) diurnal and latitudinal vTEC variations and (ii) Δ H values along with the IEEJ values (scaled on the right hand side of Y axis in blue line) as well as IEF Ey (scaled on the left hand side of Y axis in black line), (c) VTEC cross-section around 18:00 UT for each day smoothed with Savitzky-Golay filter of one degree, (d) PLP plasma density (blue), the satellite path (colour coded as a function of ascending flight altitude) and the geomagnetic dip equator (green) on the African map background, and (e) and (f) the computed ROT fluctuations for NAMA and MAL2 GPS stations, respectively, during 3-6 April 2012. The two red vertical dashed lines in (a) and (b) show the period of IMF Bz southward turnings. The two white horizontal dashed lines in panel (b) depict the geographical locations of NAMA (north) and MAL2 (south) GPS stations on the TEC maps (EIA profiles).

were absent on 5 April 2012 (i.e. a geomagnetically moderate day) as well as during the geomagnetic quiet day on 3 April 2012. The 5 April corresponds to the period when there were less EPB activity and ionospheric irregularities.

It has been reported (e.g. Basu et al., 1996; Mungufeni et al., 2015, 2016) that ROT values could be higher where the ionospheric density gradient is larger. To examine this, TEC values for around 18:00 UT (TEC data was binned in 70-minute resolution) were extracted from the TEC maps in Figure 8.2(b)(i), in order to compare the steepness of the ionization gradient and to infer the strength of the electrodynamic drift around this time (Mendillo et al., 2001). This is shown in Figure 8.2(c). It is evident from Figure 8.2(c) that there is a correlation between the steepness of the TEC

gradient and the ROT values: the less steep the TEC gradient, the closer the ROT values to zero, as during 3-5 April. On 6 April the steeper TEC gradient comes with larger ROT values (see Figures 8.2(c), 8.2(e) and 8.2(f)). Relative comparisons of the strength of TEC gradients was made by computing the TEC peak-to-trough gradient in Figure 8.2(c), i.e. the difference between the minimum VTEC values at the troughs and the maximum VTEC values at both sides of the crests (i.e. north and south) over a latitude range of ∼10 degree (approximate range between the troughs and the crests) for consecutive days during this geomagnetic storm period. Similar analyses were made for the other storm periods. The TEC peak-to-trough gradient on 5 April was ∼1.0 TECU/deg (north) and ∼ 2.0 TECU/deg (south), while it was ∼ 2.3 TECU/deg (north) and ∼3.5 TECU/deg (south) on 6 April. Thus, there was an increase of ∼ 1.3 TECU/deg (north) and ∼ 1.5 TECU/deg (south) on the quiet day when the EPB activity recovered, compared to the day of the storm when EPB activity was suppressed. Similarly, TEC fluctuations were also higher on 6 April (maximum ROT is ∼6 TECU/min) compared to 3 and 5 April (maximum ROT is ∼1 and ∼1.5, respectively) when these TEC peak-to-trough increases were observed.

Figure 8.2(b)(ii) shows that the ΔH values varied significantly during 3-6 April 2012. On 5 April 2012, the EEJ strength was small compared to the EEJ strength on 6 April. Moreover, EEJ strength had enhanced negative values for a few hours before 06:00 UT (08:35 LT) on 5 April (day of the storm). Note that sunrise and sunset at Addis Ababa (AAE) station are around 03:10 UT and 15:40 UT respectively (http://www.esrl.noaa.gov/gmd/grad/solcalc/). The diminished daytime EEJ during the geomagnetically quiet day on 3 April could be related to the absence of EIA crests on 3 April 2012 and insignificant EPBs observed by C/NOFS (refer to Figure 8.2(d)). The daytime ΔH measurement was significantly enhanced (increased

to around 50 nT) during 6 April 2012, which also supports the presence of fully developed EIA peaks, during which well-developed ionospheric irregularity (i.e. TEC fluctuations) and post-sunset EPBs activity were observed. However the fact that there were no TEC irregularities during 4 April even though daytime ΔH measurements were also significantly enhanced suggest that there may have been another mechanisms that dominated that day. For example, the near sunset TEC gradient on 4 April was smaller compared to the TEC gradient on 6 April and may explain why little or no TEC fluctuations are observed on 4 April. This competing roles has also been reported by Muella et al. (2010) over the South American longitude sector.

8.1.2 Moderate geomagnetic storm on 13 April 2012

Figure 8.3(a) (i)-(iv) displays the solar wind conditions and geomagnetic indices during 11-15 April 2012. Although the solar wind speed, panel (i), progressively increased starting around 05:00 UT on 12 April 2012, the sudden increase at around 16:20 UT on the same day led to a moderate geomagnetic disturbance that reached a minimum SYM-H, panel (iv), of -54 nT around 05:00 UT on 13 April 2012. The IMF Bz, panel (ii), showed fluctuation and remained predominantly southward during the main phase of the geomagnetic storm. This is marked between the two red vertical dashed lines in Figure 8.3(a). The AE index, panel (v), also increased to around 1300 nT during this period.

Figure 8.3(d) and Figure 8.4 show observations of equatorial plasma densities and the corresponding meridional drift velocities respectively for successive orbit passes during 11-13 and 15 April 2012. Note that only one case of meridional drift velocities is presented, since the IVM velocities in all the other cases also correlated with the

plasma density depletions observed. It is evident that there was a lot of EPB activity on 11 and 12 April 2012, but more pronounced on 12 April, which coincidently was the main phase of the moderate geomagnetic storm (see orbits 21676 - 21677 in particular). The corresponding drift velocities reached 300 m/s (refer to Figure 8.4). However, they were partially suppressed on 13 April during the recovery phase of the moderate geomagnetic storm activity, as well as on 15 April 2012 when geomagnetic conditions were quiet. There were no C/NOFS data for 14 April 2012.

Presented in Figures 8.3(e) and 8.3(f) are the computed TEC fluctuations for the ground stations during 11-15 April 2012. Both NAMA and MAL2 stations observed signatures of intense ionospheric irregularity on 11 and 12 April, whereas they decayed during 13-15 April, although slightly pronounced on the former station, supporting the C/NOFS observations (see Figure 8.3(d)); for example on 11-12 April the TEC fluctuations observed by NAMA have higher ROT values and observed over a longer time interval than on 13-15 April. This trend is also observed with the TEC peak-to-trough ratios, for e.g. these ratios were ∼0.7 TECU/deg (north) and ∼2 TECU/deg (south) on 13 April, ∼0.4 TECU/deg (north) and ∼2 TECU/deg (south) on 14 April , and ∼1.0 TECU/deg (north) and ∼1.6 TECU/deg (south) on 15 April compared to ∼1.1 TECU/deg (north) and ∼2.5 TECU/deg (south) on 11 April as well as 2.5 TECU/deg (north) and 3.5 TECU/deg (south) on 12 April. The discrepancy between the NAMA and MAL2 observations displays differences of ionospheric irregularity in the northern (NAMA) and southern (MAL2) hemispheres of the dip equator. The TEC gradient (Figure 8.3(c)) is relatively steeper in the southern hemisphere than in the northern hemisphere, corresponding to the higher TEC fluctuation at MAL2 than at NAMA, more so during 13-15 April. For example TEC peak-to-trough gradient decreased from ∼ 2.5 TECU/deg (north), and ∼3.5 TECU/deg (south) on 12 April to ∼ 0.7 TECU/deg (north) and ∼2 TECU/deg

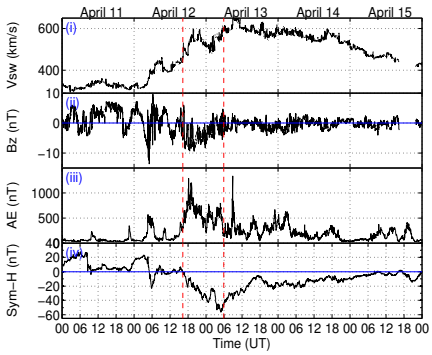

(a) Solar wind and geomagnetic indices indicators

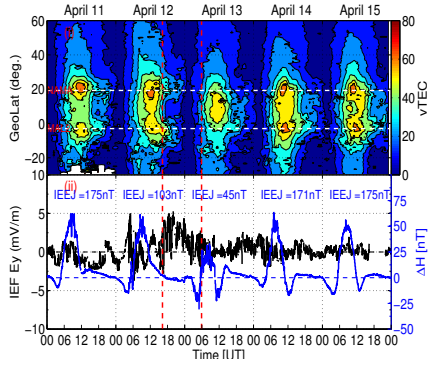

(b) TEC map, ΔH and IEF Ey values

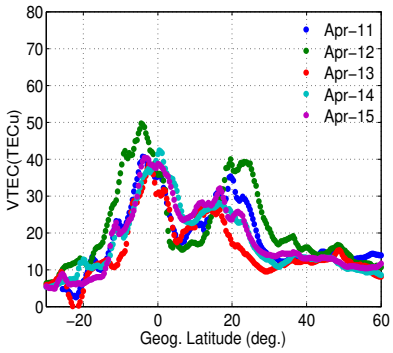

(c) VTEC values

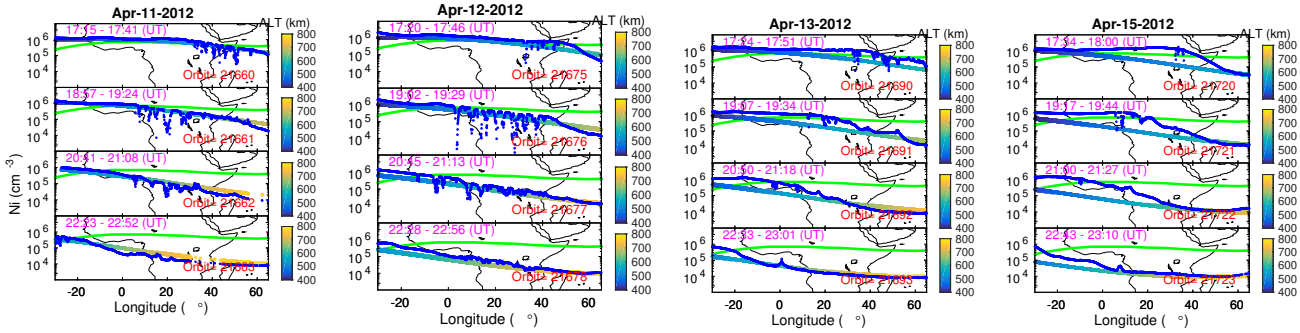

(d) C/NOFS EPBs observations

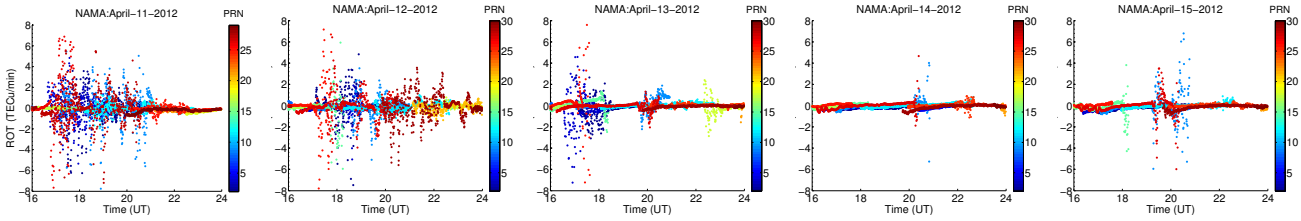

(e) ROT fluctuations at NAMA station

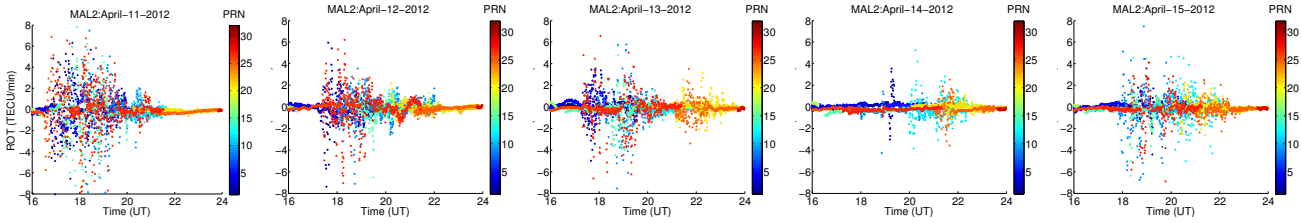

(f) ROT fluctuations at MAL2 station

Figure 8.3: Caption found on next page.

Figure 8.3: Presented in these figures are: (a) one-minute averaged solar wind conditions and geomagnetic indices, (b) (i) diurnal and latitudinal vTEC variations and (ii) Δ H values along with the IEEJ values (scaled on the right hand side of Y axis in blue line) as well as IEF Ey (scaled on the left hand side of Y axis in black line), (c) VTEC cross-section around 18:00 UT for each day smoothed with Savitzky-Golay filter of one degree, (d) PLP plasma density (blue), the satellite path (colour coded as a function of ascending flight altitude) and the geomagnetic dip equator (green) on the African map background, and (e) and (f) the computed ROT fluctuations for NAMA and MAL2 GPS stations, respectively, during 11-15 April 2012. The two red vertical dashed lines in (a) and (b) show the period of IMF Bz southward turnings. The two white horizontal dashed lines in panel (b) depict the geographical locations of NAMA (north) and MAL2 (south) GPS stations on the TEC maps (EIA profiles).

(south) on 13 April.

The variation of the drifts in Figure 8.4 indicates that C/NOFS was close to plasma bubbles on 13 and 15 April (it sees the fields from below) though they were not as developed in density as the previous nights. Thus, the disparity between C/NOFS observations and the MAL2 ROTs might be related to this. Huang (2011) reported that there was a chance that a satellite could miss the plasma bubbles, unless it went through them. This is not the case with stationary ground GPS receivers which receive signals from all visible GPS satellites (i.e PRN's). Moreover, relatively steeper TEC gradient was observed on 11 and 12 April associated with higher ROTs, in comparison with the less steep TEC gradient and small ROTs during 13-15 April

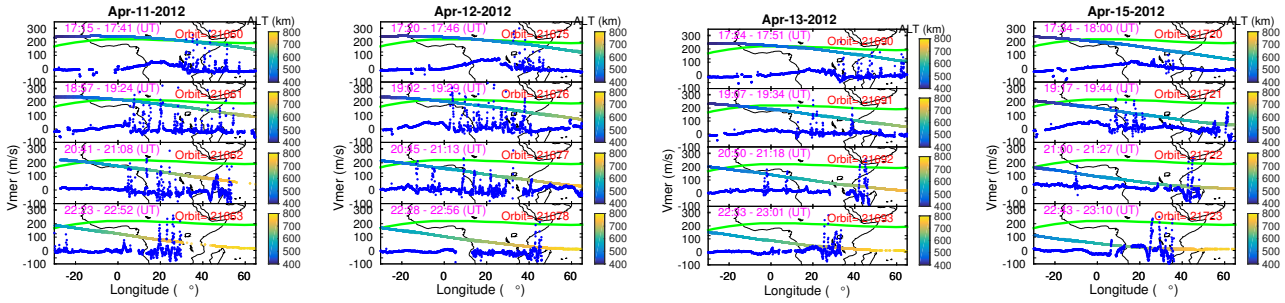

Figure 8.4: Shows IVM meridional drift velocities, the satellite path (colour coded with magnitude of ascending flight altitude), the geomagnetic dip equator (green) and the African map background for the period 11-13, and 15 April 2012. Note that there was no C/NOFS observation data for 14 April 2012.

at NAMA station.

The latitudinal and temporal variations of TEC during 11-15 April 2012 in Figure 8.3(b)(i) reveals the poorly formed EIA crests on 13 April 2012 compared to the days before and after. Figure 8.3(b)(ii) shows a diminished daytime ΔH values on 13 April 2012 during which EPB activity was significantly disrupted/interrupted, in comparison with daytime ΔH values on 11, 12, 14 and 15 April 2012. It decreased from $\sim$ 60 nT, around 08:00 UT (i.e $\sim$ 11:00 LT), on 12 April (and 11 April) to slightly less than 30 nT on 13 April, then it recovered to the pre-storm conditions on the following days. In addition, the polarity of the current was westward for a few hours before 06:00 UT (i.e. 08:30 LT) and another few hours around 12:00 UT (14:30 LT) on this day. It should be noted that despite the recovery of the ΔH and EIA crests on 15 April to pre-storm conditions, the EPB activity did not recover. Also ΔH is lower on 13 April than on 14 April, yet ROT is higher on 13 April than on 14 April. This may be related to the weaker TEC gradients during 14 and 15 April, compared to the pre-storm days in particular.

8.1.3 Moderate geomagnetic storm on 9 July 2012

Figure 8.5(a)(ii) shows a sudden IMF Bz southward turning around 21:00 UT on 8 July 2012 from around 10 nT to -9 nT and an increase of the IEF Ey from -4 to 4 mV/m (refer to Figure 8.5(b)(ii)) that persisted until around 22:00 UT on 9 July 2012. Shortly after a small enhancement, SYM-H began to decrease as the storm started to intensify until it attained a minimum of -79 nT around 21:00 UT. It shortly began to recover on 9 July 2012, and continued to recover on 10 July 2012 (see panel (iv)). The AE index, panel (iii), showed enhancement (reaching around 1800 nT) during the main phase of the storm despite a delayed start.

Figure 8.5(d) displays the plasma density measurements for the period 7-10 July 2012 during which another moderate geomagnetic storm was observed on 9 July. As is evident from this figure (second left panel), the plasma density depletions (i.e. plasma bubbles) were more pronounced for most of the post-sunset hours during the main phase on 8 July 2012. Although not shown here, EPBs were also observed on days prior to 7 July. On the contrary, during part of the main and recovery phases of the storm on 9 July 2012 the plasma bubble formation was partially inhibited (fewer bubbles compared to 08 July for example) and fully inhibited on 10 July, the recovery phase, and the days thereafter (although not shown here). Note that the satellite altitude was mostly below 500 km during this period, unlike the April cases where the satellite ascended to altitudes much higher than 600 km (i.e. topside ionosphere). In support of these C/NOFS observations, ROT measurements in Figures 8.5(e) and 8.5(f) show a strong presence of TEC fluctuations on 7 and 8 July 2012, while they are near absent or diminished on 9 and 10 July 2012.

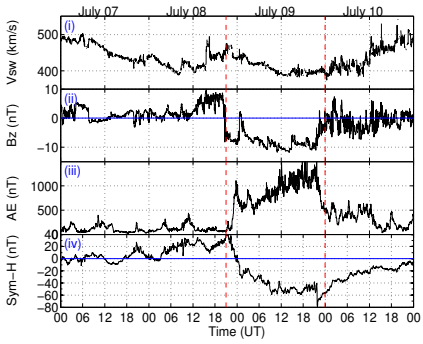

(a) Solar wind and geomagnetic indices indicators

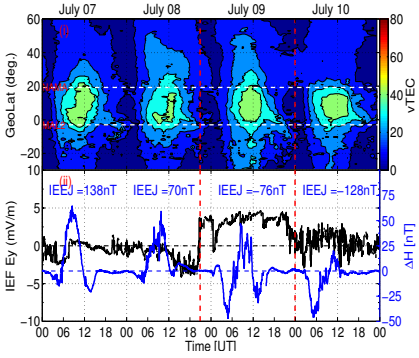

(b) TEC map, ΔH and IEF Ey values

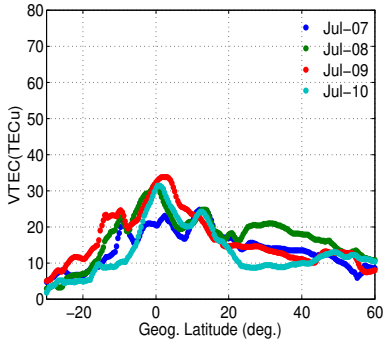

(c) VTEC values

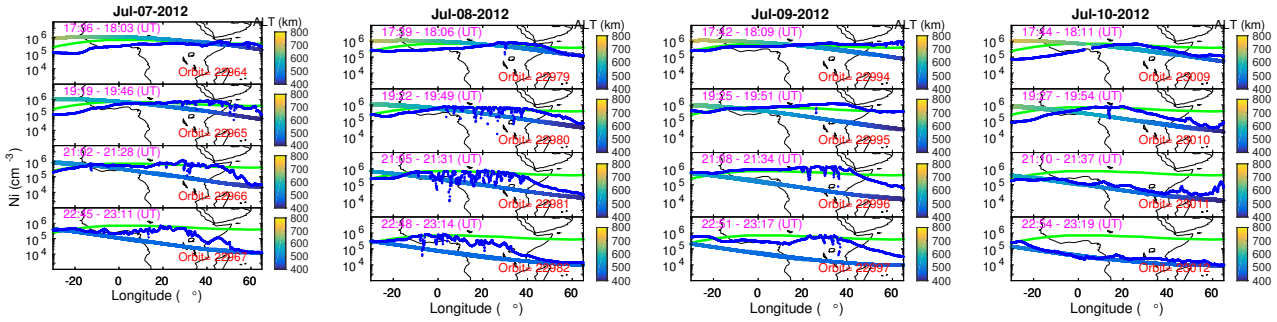

(d) C/NOFS EPBs observations

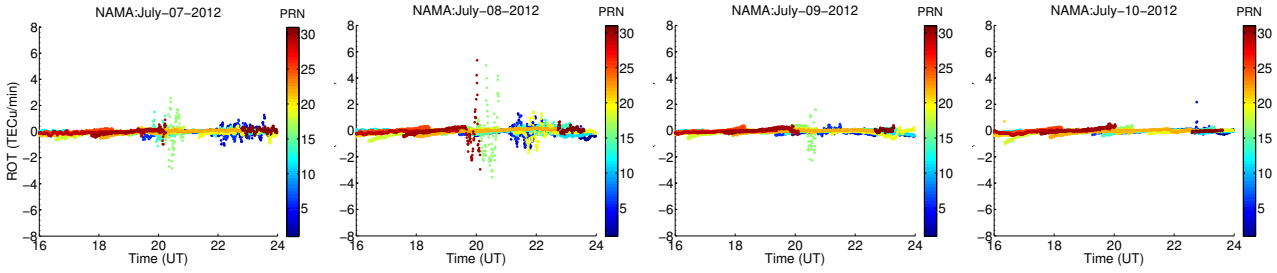

(e) ROT fluctuations at NAMA station

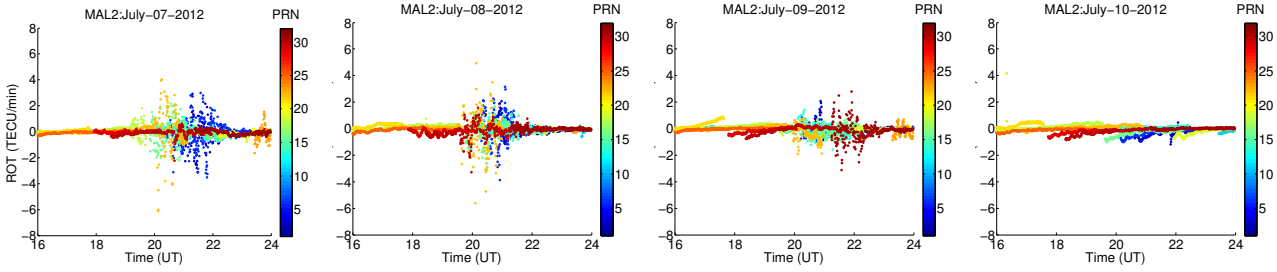

(f) ROT fluctuations at MAL2 station

Figure 8.5: Caption found on next page.

Figure 8.5: Presented in these figures are: (a) one-minute averaged solar wind conditions and geomagnetic indices, (b) (i) diurnal and latitudinal vTEC variations and (ii) Δ H values along with the IEEJ values (scaled on the right hand side of Y axis in blue line) as well as IEF Ey (scaled on the left hand side of Y axis in black line), (c) VTEC cross-section around 18:00 UT for each day smoothed with Savitzky-Golay filter of one degree, (d) PLP plasma density (blue), the satellite path (colour coded as a function of ascending flight altitude) and the geomagnetic dip equator (green) on the African map background, and (e) and (f) the computed ROT fluctuations for NAMA and MAL2 GPS stations, respectively, during 7-10 July 2012. The two red vertical dashed lines in (a) and (b) show the period of IMF Bz southward turnings. The two white horizontal dashed lines in panel (b) depict the geographical locations of NAMA (north) and MAL2 (south) GPS stations on the TEC maps (EIA profiles).

Figure 8.5(b)(i) reveals the poorly-formed equatorial ionization anomaly during 7-10 July 2012. In agreement, vTEC in Figure 8.5(c) shows no large peak-to-trough gradients, but rather slightly higher vTEC values toward the south. The EIA crests, in particular, the EIA crests were suppressed despite the positive daytime EEJ currents on 7 and 8 July 2012. However, there was TEC enhancement that extended to both the northern and southern hemispheres during the geomagnetically disturbed day (i.e. on 9 July). During the course of the main phase of the geomagnetic storm day on 9 July 2012, the EEJ switched westward between approximately 03:00-07:00 UT (05:30-09:30 LT) and in the post-noon hours between approximately 12:00-16:00 UT (14:30-18:30 LT) (Figure 8.5(b)(ii)). The daytime EEJ strength on 10 July 2012 was diminished for the entire day, in addition to the predominant westward electric

field approximately between 03:00-10:00 UT (05:30-12.30 LT). Moreover, the EEJ decreased from $\sim$ 40 nT, around 08:00 UT (i.e $\sim$ 11:00 LT), on 8 July to slightly less 20 nT on 9 July and even decreased to negative values on 10 July. Diminished EEJ and the predominantly westward electric field could be related to the reduction in EPBs on 9 and 10 July 2012.

8.2 Discussion

The results of this study reveal that the day-to-day pattern of the EPB occurrence was disrupted/interrupted following the incursion of moderate geomagnetic storms. The most consistent feature is the reduction in ionospheric irregularity (i.e. ROT and/or EPBs) with the decrease of EEJ strength, although a range of other variables also played a role. For example, on 13 April there were fewer/no EPBs observed compared to 12 April, which coincided with a decrease in EEJ strength from 103 nT on 12 April to 45 nT on 13 April. Again the same trend was seen when fewer/no EPBs were observed on 5 April and 9 July compared to 3 April and 8 July, respectively, and these coincided with a daytime EEJ decrease of 111 nT on 3 April compared to 52 nT on 5 April April and of 70 nT on 8 July compared to -76 nT 9 July, respectively. Similar observations have been reported by Dabas (2003), Ray et al. (2006), Muella et al. (2010), Carter et al. (2014), Venkatesh et al. (2015) and Seba and Nigussie (2016).

In this study the inhibition of the post-sunset plasma bubbles coincided with a decrease in the daytime EEJ strength (ΔH) following the incursion of geomagnetic storms associated with the IMF Bz southward turning. The EEJ decreased and at times turned westward (see Figures 8.2(b)(ii)- 8.3(b)(ii) and 8.5(b)(ii)) during the

southward turning of the IMF Bz (see Figures 8.2(a)- 8.3(a) and 8.5(a)), lasting between 12 and 24 hours. This observation agrees with findings by Rastogi (2006) who reported that when magnetic storms are associated with IMF Bz southward turning, the dayside electrojet s tations experience an enhancement in the decrease of the H-fields. The decrease in daytime EEJ strength led to a decrease in the upward $\mathbf{E}\times\mathbf{B}$ drift, which was evident from the absence of (poorly-formed) EIA crests, during the main and part of the recovery phase of the geomagnetic storm days in particular (see Figures 8.2(b)(i), (ii)- 8.3(b)(i), (ii) and 8.5(b)(i), (ii)). This confirms previous studies (e.g. Fejer et al., 1999; Ngwira et al., 2013a). Ray et al. (2006) showed that the daytime equatorial electrojet controls the development of the equatorial anomaly and plays a crucial role in the subsequent development of F region irregularities during the post-sunset hours. Carter et al. (2014) reported the decrease in PRE strength in response to geomagnetic activity several hours prior to PRE observations, which subsequently led to the inhibition of EPBs specifically during their season of occurrence.

Furthermore, Dabas (2003) reported that the local daytime EEJ strength (11:00 LT in a study over the Indian sector) showed a positive correlation with intensity of ionospheric scintillation at low latitudes and concluded that the EEJ strength is a useful parameter for the prediction of the subsequent growth and evolution of plasma bubbles. Moreover, Dabas (2003) and the references therein, reported that, despite the strong correlation between the daytime EEJ strength and the evening hour h'F and $\mathbf{E}\times\mathbf{B}$ variations, the exact relationship is difficult to understand. However, the author suggested that the $\mathbf{E}\times\mathbf{B}$ drift, due to EEJ, mainly controls the distribution of the background electron density and the subsequent formation of EIA at the equatorial and low latitudes. Therefore, the relative strength of the EIA and background electron density around the post-noon hours depend on the strength

of the daytime EEJ. In particular, stronger (weaker) up to the day maximum EEJ results in pronounced (poor/weak) EIA and residue ionization at later hours. The relatively stronger local background plasma density and EIA crests around the post-sunset hours enriches/strengthens the bottomside F-layer which further establishes a favourable condition for the initiation of the R-T instability that may give rise to ionospheric irregularity. Inversely, weak local residual background plasma density and poorly-formed EIA crests, due to weak daytime EEJ, may result in conditions insufficient for initiation of the R-T instability. In a similar case, Rajesh et al. (2017) reported that the weakening of the zonal electric field during the 2015 St. Patrick's Day storm, resulted in smaller $\mathbf{E}\times\mathbf{B}$ drifts and less bottomside electron density gradients, which were insufficient for substantial growth.

In the present study, the daytime strength of the EEJ decreased substantially, and most importantly, the integrated daytime EEJ strength up to the day maximum was reduced during the geomagnetically disturbed days in particular. For instance, the hourly integrated EEJ strength (i.e. IEEJ) from 04:00 - 09:00 UT (07:00 - 12:00 LT) decreased from ∼229.3 nT on 4 April to ∼52.6 nT on 5 April. Similarly, the IEEJ decreased from ∼103.12 nT on 12 April to ∼21.43 nT on 13 April. The IEEJ value of ∼70.48 on 8 July significantly decreased to ∼-76.10 nT on 9 July, which further declined/decreased to ∼-128.20 nT on 10 July 2012. Venkatesh et al. (2015) indicated that the role of the strength of EEJ up to the day maximum (i.e. integrated EEJ up to day maximum level) was more significant than the influence of EEJ after day maximum for the formation of the EIA crest. The conclusions of that study agree with earlier work by Rastogi and Klobuchar (1990) who reported that past history of electrojet variation in the earlier hours determines the development of the anomaly in the evening hours. The results of the study presented in this chapter therefore agree with those of Rastogi and Klobuchar (1990) and Venkatesh

et al. (2015) as they show that the reduced daytime EEJ strength, up to the day maximum in particular, correlated with the either full or partial inhibition of EPBs following the geomagnetic storms. The results in this study also showed that the strength of EEJ correlated to the EIA formation in agreement with previous studies (e.g. Muella et al., 2010; Venkatesh et al., 2015).

The strength of TEC peak-to-trough gradients (as shown in panels (c) of Figures 8.2, 8.3 and 8.5) around 18:00 UT, i.e. around the time of the EPB activity/TEC fluctuations, seems to play a role in the existence of the latter. It is evident that the presence of more intense TEC fluctuations (i.e. large ROT values) corresponded well with the steeper TEC peak-to-trough gradients, and agrees with findings by Basu et al. (1999). For example, during the 3-5 April period the TEC gradients were less steep (for example the peak-to-trough were $\sim$ 1.8 TECU/deg (north) and $\sim$3.2 TECU/deg (south) on 3 April, $\sim$ 1.2 TECU/deg (north) and $\sim$2.2 TECU/deg (south) on 4 April and $\sim$ 1.0 TECU/deg (north) and $\sim$2.0 TECU/deg (south) on 5 April) and ROT values near zero compared to the steep TEC gradient and large ROT values observed on 6 April (i.e. peak-to-trough value of $\sim$ 2.3 TECU/deg (north) and $\sim$3.5 TECU/deg (south) and maximum ROT of $\sim$6 TECU/min) as shown in Figures 8.2(e), 8.2(f) and 8.2(c) respectively.

The differences in the hemispheric TEC peak-to-trough gradient strength is reflected on the differences in the level of TEC fluctuations. For instance, during 13-15 April (see Figure 8.3c) relatively intense TEC fluctuations were observed at the southern crest (i.e. near MAL2, see Figure 8.3(f)), compared to the TEC fluctuations on the northern crest (i.e. near NAMA, see Figure 8.3(e)). This observation is in consonance with findings by Mendillo et al. (2001) who reported that high peak-to-trough ratio values (i.e. higher density gradient) were associated with strong

electrodynamical vertical drift which in turn led to dramatic EIA, thereby controlling the evolution/development of irregularities around sunset. It has also been shown that higher TEC gradient and strong background plasma density around sunset creates favourable conditions for the formation of ionospheric irregularities (Dabas, 2003; Muella et al., 2010). Furthermore, Ray et al. (2006) observed that a steep gradient in the latitudinal variation of TEC in the region between the magnetic equator and ionization crests, associated with a developed EIA in the afternoon hours, may be taken as a precursor to the occurrence of scintillation.

The observed asymmetries in the post-sunset ionospheric irregularity and the insignificant EPB activity despite the presence of strong EEJ during the April geomagnetic storms (e.g. fewer EPBs on 15 April compared to 11-12 April) could be due to the intervention of meridional winds. Muella et al. (2010) and the references therein, showed that the thermospheric meridional/transequatorial winds can also affect the evolution of small scale-length irregularities associated with plasma bubbles in the equatorial ionosphere. Similarly, Abdu et al. (2009) suggested that thermospheric meridional winds resulted in the asymmetric spatial distribution of smaller-scale irregularities at magnetic conjugate points, due to modifications of the ambient densities and the electron density spatial gradients. Mendillo et al. (1992) reported that the net effect of transequatorial winds was the inhibition of EPB development. However, this could not be investigated in the present study, due to the absence of thermospheric wind and/or ionosonde measurements for these periods in this region.

The absence of (or poorly-formed) EIA crests during 7-10 July (see Figure 8.5(b)(i)), even though the EEJ strength was comparable to the EEJ strength of the April cases, could be due to the seasonal variation of the background ionosphere. This seasonal

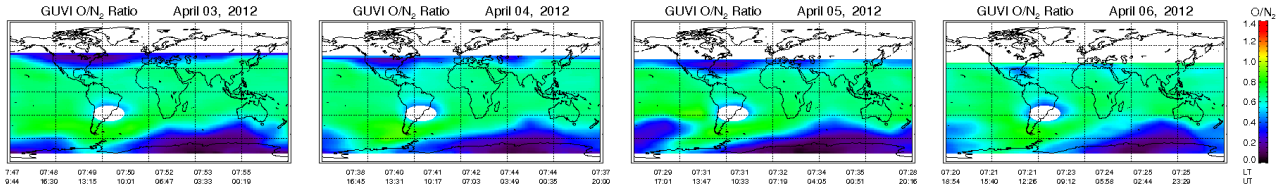

(a) O/N_2 ratio during 03-06 April 2012

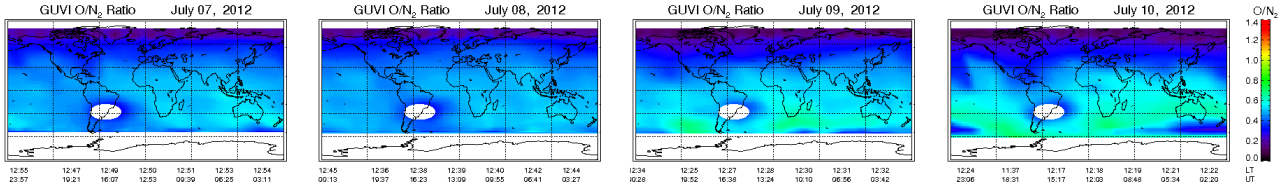

(b) O/N_2 ratio during 07-10 July 2012

Figure 8.6: O/N_2 ratio from GUVI measurements for (a) 3 - 6 April and (b) 7-10 July 2012.

variation in the ionization level of the background ionosphere is also supported by the International Reference Ionosphere (IRI) model maps (not shown here), which for July showed a background ionosphere which was more diminished than for the April days. Venkatesh et al. (2015) showed that the EEJ strength (hence the EIA) was weak around July and November and strong around the equinox over the Indian sector (75°E), depicting the seasonal variations. In addition, the low-level O/N_2 ratio in Figure 8.6(b), shows the neutral molecular rich ionosphere during July as opposed to the high O/N_2 ratio in April (Figure 8.6(a)). The presence of a low O/N_2 ratio during July indicates that the recombination process is dominant and could lead to weak EIA crests (Tesema et al., 2015).

Overall, the observations of this study revealed that the evolution of EPBs depends on the strength of the daytime EEJ and not necessarily the presence/strength of EIA; the latter is particularly evident during the July storm case. Moreover, the background electron density, the strength of the TEC gradient around post-sunset

hours and the thermospheric meridional/transequatorial winds played roles by either favouring or disrupting the R-T instabilities, thereby affecting the evolution of post-sunset EPB activity and/or ionospheric irregularities during/after geomagnetic storms. Unlike the other longitude sectors, few such studies have been done for the African longitude sector. In line with this, Kassa and Damtie (2017) pointed out that the study of the generation or inhibition of ionospheric irregularities during geomagnetic storms may not be explained by the characterization of the occurrence time of the minimum Dst, orientation of IMF Bz, neutral winds or electric fields individually.

8.3 Conclusions

In this study the effects of three moderate geomagnetic storms that occurred during April and July 2012, on the evolution of EPBs and/or ionospheric irregularities were investigated. The cases considered were during the occurrence season of EPB activity (i.e. when EPB activity was prevalent during the quiet days before and/or after the disturbed day(s) considered), over the east African equatorial ionosphere. C/NOFS observations, TEC fluctuation measurements (i.e. ROT fluctuations) from two low-latitude GPS stations and latitudinal and temporal variation of GPS-TEC from an array of GPS stations located along the east African longitude (i.e. $\sim$35°E) were used for the analysis. The results of this study showed that the daytime EEJ strength, the steepness of the TEC gradient and/or meridional/transequatorial thermospheric winds sometimes have collective/interwoven effects, while at other times one mechanism dominates. The decrease in the daytime EEJ currents during geomagnetic storms associated with the IMF Bz southward turning in particular,

subsequently led to either partial or full inhibition/interruption of ionospheric irregularities (i.e. EPBs and TEC fluctuations (ROT values)). In addition, it was found that the hemispheric plasma density gradient (TEC gradient) also played a role in the evolution of large-scale ionospheric irregularity (ROT). Thus, the study suggests these parameters as possible prediction indicators over the region of study, as suggested by previous studies at other longitude sectors. In conclusion, this chapter contains the first report, based on multiple cases on the effects of decrease in the daytime EEJ currents on equatorial ionospheric irregularities during moderate geomagnetic storms over the African longitudes.

Chapter 9

Conclusions and future work

9.1 Conclusions

The objectives of this research were to assess the possibilities of imaging ionospheric structures of different scale sizes by means of an inversion technique, and to investigate the effects of geomagnetic storms on the evolution of post-sunset EPBs and/or ionospheric irregularities over the East African longitude sector. Therefore, the ability of the inversion algorithm called MIDAS to image ionospheric structures of different scale sizes was assessed during both quiet and disturbed conditions and the results validated against the results of independent global ionospheric models and observations. The results obtained from the optimised MIDAS algorithm for a selected region of the well-populated East African longitude sector, are reported in Chapters 5 and 6. It was found that the number of available GPS ground receivers and their spatial distribution on the African sector was too limited to investigate the full ability of MIDAS to image small-scale structures, (see Chapter 7 in particular). Therefore, the evolution and electrodynamics of ionospheric irregularities during geomagnetically disturbed periods, by means of measurements by ground- and space-based instruments, was studied.

In Chapter 5 the results of the MIDAS reconstruction is compared with the IRI and GIM models for the East African longitude sector. In a case study of the period 04-14 March 2012, during which storm conditions were moderate to strong, MIDAS with a minimum RMSE results were more in line with VTEC observations (minimum RMSE was 2.91 TECU) than the results produced by the IRI and GIM models (minimum RMSEs of 13.03 TECU and 6.52 TECU respectively), for all the test stations and the validation days. This showed that with good GPS coverage the optimised MIDAS algorithm, as presented in Chapter 4, can offer an accurate ionospheric specification for the African region in general, and for the East African longitudes, in particular (Giday and Katamzi-Joseph, 2017).

Chapter 6 reports on a comparison between MIDAS and ANN to reconstruct storm-time TEC for the African low- and mid-latitude regions. MIDAS performed very well compared to ANN in capturing TEC enhancements and depletions as well as short term features as observed during the selected storm periods. This study proved that the accuracy of MIDAS does not deteriorate with increasing storm intensity. In fact, based on the storms studied, MIDAS reconstructed storm-time TEC more accurately for severe storms (16 - 22 March 2015) than it did for strong storms (18 - 24 February 2014). On average, MIDAS performed 13.44 % better than ANN for the African mid-latitudes while the ANN model performed 24.37 % better than MIDAS for the low latitudes (Uwamahoro et al., 2017). The fountain effect and the resulting higher TEC gradients over the low latitude ionosphere are likely the causes of the difficulty in reconstructing TEC for this region. This was also reported by Muella et al. (2011). Yet, MIDAS estimations of the storm-time TEC are more accurate than those of IRI-2016 for the region of study.

In Chapter 7, the challenges of imaging small-scale ionospheric irregularities and EPBs with the MIDAS algorithm is addressed. Kinrade (2013) reported that, in regions with good data coverage, while a loosely constrained MIDAS inversion may image finer spatial structures, the solution might as well eventually become unstable leading to potential false artefacts. While the imaging of small-scale ionospheric structures and/or EPBs was not possible with MIDAS, partly due to the paucity of data over the region and its' inherent horizontal smoothing regularization factor, a large-scale ionospheric structure, the EIA, was imaged with good accuracy (see Chapter 5).

Chapter 8 addresses the effects of moderate geomagnetic storms on the evolution of EPBs and/or ionospheric irregularities, during their season of occurrence over the East African equatorial ionosphere. Plasma densities from PLP C/NOFS observations, TEC fluctuations (i.e. ROT fluctuations) from two low-latitude GPS stations and latitudinal and temporal variations of GPS-TEC from an array of GPS stations located along the East African longitude were used for the analysis. The results of this study showed that the daytime EEJ strength, or/and the steepness of the TEC peak-to-trough gradient sometimes have a collective effect, while at other times one mechanism dominates. This was also reported by Kassa and Damtie (2017). The decrease in the daytime EEJ currents during geomagnetic storms associated with the IMF Bz southward turnings in particular, subsequently led to either partial or full inhibition/interruption of the ionospheric irregularities (i.e. EPBs and TEC fluctuations (ROT values)). This agrees with reports by Dabas (2003), Ray et al. (2006), Muella et al. (2010), Carter et al. (2014), Venkatesh et al. (2015) and Seba and Nigussie (2016).

9.2 Future work

MIDAS reconstructed TEC for the East African longitude sector with better accuracy than the recent IRI (i.e. IRI-2012 and IRI-2016) and GIM models during both quiet and disturbed geomagnetic conditions. However, imaging of smaller-scale ionospheric structures was not possible with the current MIDAS version. Although the scarcity of GPS receivers in the African sector was factor that limited the full investigation of the MIDAS inversion's ability, the nature of constraining basis functions within MIDAS are also not well suited for small-scale imaging, as pointed out by Kinrade (2013) and Panicciari et al. (2015). Panicciari et al. (2015) upgraded the MIDAS version to use wavelet basis functions that allows sparse regularization in regions of unevenly distributed GPS receivers in order to capture small-scale ionospheric structures. Therefore, this version of the software could be tested in the equatorial regions in an effort to image EPBs and equatorial irregularities.

The region of study has a shortage of sounding instruments which handicaps the study of the electrodynamics of the equatorial ionosphere. Of importance to fully understanding the evolution of post-sunset EPBs would be ionosonde and neutral wind measurements that provide nighttime plasma drift velocities to supplement the daytime ΔH proxy. Due to lack of concurrent measurements by space- and ground-based instruments and due to time constraints, the study of the evolution of EPBs was limited to only three moderate storm conditions in the East African longitude sector. However, the study could be extended by using datasets of longer periods (i.e. include more moderate storms) by incorporating different storm strengths (e.g. comparing the effects of storms of different magnitudes) and including data for other longitude sectors (e.g. comparing behaviour at different longitudes), particularly in regions where simultaneous recording of data by different instruments is available.

References

Aarons, J.: The role of the ring current in the generation or inhibition of equatorial F layer irregularities during magnetic storms, Radio Science, 26, 1131–1149, doi: 10.1029/91RS00473, 1991.

Abdu, M. A., Batista, I. S., Reinisch, B. W., De Souza, J. R., Sobral, J. H. A., Pedersen, T. R., Medeiros, A. F., Schuch, N. J., De Paula, E. R., and Groves, K. M.: Conjugate Point Equatorial Experiment (COPEX) campaign in Brazil: Electrodynamics highlights on spread F development conditions and day-to-day variability, Journal of Geophysical Research: Space Physics, 114, doi:10.1029/ 2008JA013749, 2009.

Abdu, M. A.: Equatorial spread F/plasma bubble irregularities under storm time disturbance electric fields, Journal of Atmospheric and Solar-Terrestrial Physics, 75-76, doi:10.1016/j.jastp.2011.04.024, 2012.

Abdu, M. A.: Electrodynamics of ionospheric weather over low latitudes, Geoscience Letters, 3, 11, doi:10.1186/s40562-016-0043-6, 2016.

Acharya, R., Roy, B., Sivaraman, M., and Dasgupta, A.: Prediction of ionospheric total electron content using adaptive neural network with in-situ learning algorithm, Advances in Space Research, 47, 115–123, 2011.

Adewale, A., Oyeyemi, E., Adeniyi, J., Adeloye, A., and Oladipo, O.: Comparison of

total electron content predicted using the IRI-2007 model with GPS observations over Lagos, Nigeria, Indian Journal of Radio & Space Physics, 40, 21–25, 2011.

Alken, P. and Maus, S.: Spatio-temporal characterization of the equatorial electrojet from CHAMP, Ørsted, and SAC-C satellite magnetic measurements, Journal of Geophysical Research: Space Physics, 112, doi:10.1029/2007JA012524, 2007.

Allain, D. and Mitchell, C. N.: Ionospheric delay corrections for single-frequency GPS receivers over Europe using tomographic mapping, GPS Solutions, 13, 141–151, 2009.

Amabayo, E. B., Jurua, E., and Cilliers, P. J.: Validating the use of scintillation proxies to study ionospheric scintillation over the Ugandan region, Journal of Atmospheric and Solar-Terrestrial Physics, 128, 84–91, doi:10.1016/j.jastp.2015.03.006, 2015.

Anderson, D., Anghel, A., Chau, J., and Veliz, O.: Daytime vertical E × B drift velocities inferred from ground-based magnetometer observations at low latitudes, Space Weather, 2, doi:10.1029/2004SW000095, 2004.

Anderson, D., Araujo-Pradere, E., and Scherliess, L.: Comparing daytime, equatorial ExB drift velocities and TOPEX/TEC observations associated with the 4-cell, non-migrating tidal structure, Annales Geophysicae, 27, 2861–2867, doi:10.5194/angeo-27-2861-2009, 2009.

Austen, J., Franke, S., Liu, C., and Yeh, K.: Application of Computerized tomography techniques to ionospheric research, pp. 25–35, International Beacon Satellite Syposium; Oulu, Finland, 1986.

Austen, J. R., Franke, S. J., and Liu, C. H.: Ionospheric imaging using computerized tomography, Radio Science, 23, 299–307, 1988.

Bagiya, M. S., Iyer, K., Joshi, H., Thampi, S. V., Tsugawa, T., Ravindran, S., Sridharan, R., and Pathan, B.: Low-latitude ionospheric-thermospheric response to storm time electrodynamical coupling between high and low latitudes, Journal of Geophysical Research: Space Physics, 116, 2011.

Bartels, J., Heck, N., , and Johnston, H.: The three-hour-range index measuring geomagnetic activity, Journal of Geophysical Research, 44, 411–454, 1939.

Basu, Sa., Basu, Su., Aarons, J., McClure, J. P., and Cousins, M. D.: On the coexistence of kilometer- and meter-scale irregularities in the nighttime equatorial F region, Journal of Geophysical Research: Space Physics, 83, 4219–4226, doi: 10.1029/JA083iA09p04219, 1978.

Basu, Sa., Basu, Su., and Hanson, W.: The role of in-situ measurements in scintillation modelling, in: In: Symposium on the Effect of the Ionosphere on Radiowave Systems, Washington, DC, April 14-16, 1981, Preprints.(A82-18051 06-32) Washington, DC, US Naval Research Laboratory, 1981, 1981.

Basu, Sa., Kudeki, E., Basu, Su., Valladares, C. E., Weber, E. J., Zengingonul, H. P., Bhattacharyya, S., Sheehan, R., Meriwether, J. W., a. Biondi, M., Kuenzler, H., and Espinoza, J.: Scintillations, plasma drifts, and neutral winds in the equatorial ionosphere after sunset, Journal of Geophysical Research, 101, 26 795, doi:10.1029/96JA00760, 1996.

Basu, Sa., Groves, K. M., Quinn, J. M., and Doherty, P.: A comparison of TEC fluctuations and scintillations at Ascension Island, Journal of Atmospheric and Solar-Terrestrial Physics, 61, 1219–1226, doi:10.1016/S1364-6826(99)00052-8, 1999.

Baumjohann, W. and Treumann, R.: Basic space plasma physics, Imperial college Press, London, 1997.

Bilitza, D.: International reference ionosphere: Recent developments, Radio Science, 21, 343–346, 1986.

Bilitza, D.: International Reference Ionosphere 2000, Radio Science, 36, 261–275, 2001.

Bilitza, D. and Reinisch, B. W.: International Reference Ionosphere 2007: Improvements and new parameters, Advances in Space Research, 42, 599–609, doi: 10.1016/j.asr.2007.07.048, 2008.

Bilitza, D., McKinnell, L. A., Reinisch, B., and Fuller-Rowell, T.: The international reference ionosphere today and in the future, Journal of Geodesy, 85, 909–920, doi:10.1007/s00190-010-0427-x, 2011.

Bilitza, D., Altadill, D., Zhang, Y., Mertens, C., Truhlik, V., Richards, P., McKinnell, L.-A., and Reinisch, B.: The International Reference Ionosphere 2012 – a model of international collaboration, Journal of Space Weather and Space Climate, 4, doi:10.1051/swsc, 2014.

Blanc, M. and Richmond, A.: The ionospheric disturbance dynamo, Journal of Geophysical Research: Space Physics, 85, 1669–1686, doi:10.1029/JA085iA04p01669, 1980.

Bracewell, R.: Strip Integration in Radio Astronomy, Australian Journal of Physics, 9, 198, 1956.

Burke, W. J., de La Beaujardière, O., Gentile, L. C., Hunton, D. E., Pfaff, R. F., Roddy, P. A., Su, Y.-J., and Wilson, G. R.: C/NOFS observations of plasma density and electric field irregularities at post-midnight local times, Geophysical Research Letters, 36, doi:10.1029/2009GL038879, 2009.

Bust, G. S. and Mitchell, C. N.: Review of the Current Status of Four-Dimensional

Ionospheric Imaging, in: In Characterising the Ionosphere ., vol. 46 of *Meeting Proceedings RTO-MP-IST-056, Paper 31*, pp. 31–1–31–18, Neuilly-sur-Seine, France: RTO., 2006.

Bust, G. S. and Mitchell, C. N.: History, current state, and future directions of ionospheric imaging, Reviews of Geophysics, 46, 2008.

Campbell, W. H.: Introduction to geomagnetic fields, Cambridge University Press, 2003.

Cander, L. R.: Artificial neural network applications in ionospheric studies, Annals of Geophysics, 41, 1998.

Carter, B. A., Retterer, J. M., Yizengaw, E., Groves, K., Caton, R., McNamara, L., Bridgwood, C., Francis, M., Terkildsen, M., Norman, R., and Zhang, K.: Geomagnetic control of equatorial plasma bubble activity modeled by the TIEGCM with Kp, Geophysical Research Letters, 41, doi:10.1002/2014GL060953, 2014.

Censor, Y.: Finite series-expansion reconstruction methods, Proceedings of the IEEE, 71, 409–419, 1983.

Chartier, A. T., Mitchell, C. N., and Jackson, D. R.: A 12 year comparison of MIDAS and IRI 2007 ionospheric Total Electron Content, Advances in Space Research, 49, 1348–1355, doi:10.1016/j.asr.2012.02.014, 2012.

Chartier, A.: Ionospheric Specification and Forecasting, Ph.D. thesis, University of Bath, 2013.

Chartier, A. T., Kinrade, J., Mitchell, C. N., Rose, J. A. R., Jackson, D. R., Cilliers, P., Habarulema, J.-B., Katamzi, Z., Mckinnell, L.-A., Matamba, T., Opperman, B., Ssessanga, N., Giday, N. M., Tyalimpi, V., Franceschi, G. D., Romano, V., Scotto, C., Notarpietro, R., Dovis, F., Avenant, E., Wonnacott, R., Oyeyemi, E.,

Mahrous, A., Tsidu, G. M., Lekamisy, H., Olwendo, J. O., Sibanda, P., Gogie, T. K., Rabiu, B., Jong, K. D., and Adewale, A.: Ionospheric imaging in Africa, Radio Science, 49, 19–27, doi:10.1002/2013RS005238, 2013RS005238, 2014.

Cilliers, P. J., Opperman, B. D., Mitchell, C. N., and Spencer, P. J.: Electron density profiles determined fromtomographic reconstruction of total electron content obtained from GPS dual frequency data: First results from the South African network of dual frequency GPS receiver stations, Advances in Space Research, 34, 2049–2055, 2004.

Ciraolo, L. and Spalla, P.: Comparison of ionospheric total electron content from Navy Navigation Satellite System and the GPS, Radio Science, 32, 1071–1080, doi:10.1029/97RS00425, 1997.

Crowley, G. and Meier, R. R.: p. 221–234, American Geophysical Union, doi:10.1029/181GM20, 2013.

Dabas, R. S.: Evolution and dynamics of equatorial plasma bubbles: Relationships to ExB drift, postsunset total electron content enhancements, and equatorial electrojet strength, Radio Science, 38, 1–11, doi:10.1029/2001RS002586, 2003.

Dao, E., Kelley, M. C., Roddy, P., Retterer, J., Ballenthin, J. O., de La Beaujardiere, O., and Su, Y.-J.: Longitudinal and seasonal dependence of nighttime equatorial plasma density irregularities during solar minimum detected on the C/NOFS satellite, Geophysical Research Letters, 38, doi:10.1029/2011GL047046, 2011.

Davies, K.: Ionospheric radio, IEEE Electromagnetic Waves Series, Peter Peregrinus, London, 1990.

Davis, T. N. and Sugiura, M.: Auroral electrojet activity index AE and its' universal time variations, Journal of Geophysical Research, 71, 785–801, 1966.

de Abreu, A. J., Fagundes, P. R., Gende, M., Bolaji, O. S., de Jesus, R., and Brunini, C.: Investigation of ionospheric response to two moderate geomagnetic storms using GPS-TEC measurements in the South American and African sectors during the ascending phase of solar cycle 24, Advances in Space Research, 53, doi: 10.1016/j.asr.2014.02.011, 2014.

de La Beaujardière, O., Jeong, L., Basu, B., Basu, S., Beach, T., Bernhardt, P., Burke, W., Groves, K., Heelis, R., Holzworth, R., Huang, C., Hunton, D., Kelley, M., Pfaff, R., Retterer, J., Rich, F., Starks, M., Straus, P., and Valladares, C.: C/NOFS: A mission to forecast scintillations, Journal of Atmospheric and Solar-Terrestrial Physics, 66, 1573–1591, doi:10.1016/j.jastp.2004.07.030, 2004.

de Siqueira, P. M., de Paula, E. R., Muella, M. T. A. H., Rezende, L. F. C., Abdu, M. A., and Gonzalez, W. D.: Storm-time total electron content and its response to penetration electric fields over South America, Annales Geophysicae, 29, 1765–1778, doi:10.5194/angeo-29-1765-2011, 2011.

Fausett, L.: Fundamentals of Neural Networks: Architectures, Algorithms, and Applications, Prentice-Hall, Inc., New Jersey, 1994.

Fehmers, G.: Tomography of the Ionosphere, Technische Universiteit Eindhoven, 1996.

Fejer, B. G.: Low latitude storm time ionospheric electrodynamics, Journal of atmospheric and solar-terrestrial physics, 64, 1401–1408, 2002.

Fejer, B. G. and Scherliess, L.: Empirical models of storm time equatorial zonal electric fields, Journal of Geophysical Research, 102, doi:10.1029/97JA02164, 1997.

Fejer, B. G., Scherliess, L., and de Paula, E. R.: Effects of the vertical plasma drift velocity on the generation and evolution of equatorial spread F, Journal of Geophysical Research, 104, doi:10.1029/1999JA900271, 1999.

Fremouw, E. J., Secan, J. A., and Howe, B. M.: Application of stochastic inverse theory to ionospheric tomography, Radio Science, 27, 721–732, 1992.

Fridman, S. V., Nickisch, L. J., and Hausman, M.: Personal-computer-based system for real-time reconstruction of the three-dimensional ionosphere using data from diverse sources, Radio Science, 44, 2009.

Garcia-Fernandez, M., Desai, S. D., Butala, M. D., and Komjathy, A.: Evaluation of different approaches to modeling the second-order ionospheric delay on GPS measurements, Journal of Geophysical Research: Space Physics, 118, 7864–7873, doi:10.1002/2013JA019356, 2013.

Giday, N. M.: Optimizing MIDAS III Over South Africa, Master's thesis, Rhodes University, 2014.

Giday, N. M., Katamzi, Z. T., and McKinnell, L.-A.: Ionospheric tomography over South Africa: Comparison of MIDAS and ionosondes measurements, Advances in Space Research, doi:10.1016/j.asr.2015.08.017, 2015.

Giday, N. M. and Katamzi-Joseph, Z. T.: Performance of MIDAS over East African longitude sector: Case study during 04-14 March 2012 quiet to disturbed geomagnetic conditions, Space Weather, doi:10.1002/2017sw001732, 2018.

Gopalswamy, N.: Halo coronal mass ejections and geomagnetic storms, Earth Planets Space, 61, 1–3, 2009.

Gopalswamy, N., Yashiro, S., Michalek, G., Xie, H., Lepping, R., and Howard, R.: Solar source of the largest geomagnetic storm of cycle 23, Geophysical research letters, 32, 2005.

Habarulema, J. B., McKinnell, L.-A., and Cilliers, P. J.: Prediction of global positioning system total electron content using neural networks over South Africa,

Journal of Atmospheric and solar-terrestrial physics, 69, 1842–1850, 2007.

Habarulema, J. B., McKinnell, L.-A., Cilliers, P. J., and Opperman, B. D.: Application of neural networks to South African GPS TEC modelling, Advances in Space Research, 43, 1711–1720, 2009.

Habarulema, J.: A contribution to TEC modelling over Southern Africa using GPS data, Ph.D. thesis, Rhodes University, Grahamstown, South Africa, 2010.

Habarulema, J. B., McKinnell, L.-A., and Opperman, B. D.: TEC measurements and modelling over Southern Africa during magnetic storms; a comparative analysis, Journal of Atmospheric and Solar-Terrestrial Physics, 72, 509–520, 2010.

Habarulema, J. B., Katamzi, Z. T., and Yizengaw, E.: First observations of poleward large-scale traveling ionospheric disturbances over the African sector during geomagnetic storm conditions, Journal of Geophysical Research: Space Physics, 120, doi:10.1002/2015JA021066, 2015JA021066, 2015.

Habarulema, J. B. and Ssessanga, N.: Adapting a climatology model to improve estimation of ionosphere parameters and subsequent validation with radio occultation and ionosonde data, Space Weather, 15, 84–98, 2017.

Habarulema, J. B., Katamzi, Z. T., Sibanda, P., and Matamba, T. M.: Assessing ionospheric response during some strong storms in solar cycle 24 using various data sources, Journal of Geophysical Research: Space Physics, 122, 1064–1082, doi:10.1002/2016JA023066, 2016JA023066, 2017.

Hargreaves, J. K.: The upper atmosphere and solar-terrestrial relations-An introduction to the aerospace environment, 1979.

Haykin, S.: Neural Networks. A Comprehensive Foundation, Macmillan College Publishing Company, New York, USA, 1994.

Heelis, R.: Electrodynamics in the low and middle latitude ionosphere: A tutorial, Journal of Atmospheric and Solar-Terrestrial Physics, 66, 825–838, 2004.

Heelis, R. and Hanson, W.: Measurements of thermal ion drift velocity and temperature using planar sensors, Measurement techniques in space plasmas: particles, pp. 61–71, 1998.

Hofmann-Wellenhof, B., Lichtenegger, H., and Collins, J.: Global Positioning System: theory and practice, Springer-Verlag, Wien, New York, 4th edition, 1997.

Hoque, M. M. and Jakowski, N.: Ionospheric Propagation Effects on GNSS Signals and New Correction Approaches, 2012.

Howe, B. M., Runciman, K., and Secan, J. A.: Tomography of the ionosphere: Four-dimensional simulations, Radio Science, 33, 109–128, 1998.

Hsu, K.-l., Gupta, H. V., and Sorooshian, S.: Artificial Neural Network Modeling of the Rainfall-Runoff Process, Water Resources Research, 31, 1995.

Huang, C. S.: Occurrence of equatorial plasma bubbles during intense magnetic storms, International Journal of Geophysics, 2011, doi:10.1155/2011, 2011.

Huang, C.-S., Foster, J. C., and Sahai, Y.: Significant depletions of the ionospheric plasma density at middle latitudes: A possible signature of equatorial spread F bubbles near the plasmapause, Journal of Geophysical Research: Space Physics, 112, 2007.

Huang, Z. and Yuan, H.: Ionospheric single-station TEC short-term forecast using RBF neural network, Radio Science, 49, 283–292, 2014.

Hunsucker, R. D. and Hargreaves, J. K.: The high-latitude ionosphere and its effects on radio propagation, Cambridge University Press, 2003.

Jacobsen, K. S.: The impact of different sampling rates and calculation time intervals on ROTI values, Journal of Space Weather and Space Climate, 4, A33, 2014.

Jayawardena, P., Talini, S., Chartier, A. T., Spencer, P., and Mitchell, C. N.: Imaging the topside ionosphere and plasmasphere with ionospheric tomography using COSMIC GPS TEC, Journal of Geophysical Research: Space Physics, 121, 817–831, 2016.

Kassa, T. and Damtie, B.: Ionospheric irregularities over Bahir Dar, Ethiopia during selected geomagnetic storms, Advances in Space Research, doi:10.1016/j.asr.2017.03.036, 2017.

Kassa, T., Damtie, B., a. Bires, Yizengaw, E., and Cilliers, P.: Storm-time characteristics of the equatorial ionization anomaly in the East African sector, Advances in Space Research, 56, doi:10.1016/j.asr.2015.04.002, 2015.

Katamzi, Z. T.: Verification of Ionospheric tomography using MIDAS over Grahamstown, South Africa, Master's thesis, Rhodes University, 2008.

Kelley, M. C.: Penetration of the solar wind electric field into the magnetosphere/ionosphere system, Geophysical Research Letters, 30, 23–25, doi:10.1029/2002GL016321, 2003.

Kenpankho, P., Watthanasangmechai, K., Supnithi, P., Tsugawa, T., and Maruyama, T.: Comparison of GPS TEC measurements with IRI TEC prediction at the equatorial latitude station, Chumphon, Thailand, Earth, planets and space, 63, 365–370, 2011.

King, J. and Papitashvili, N.: The 40-year OMNI 2 Data Set: Challenges in Building Virtual Multi-source Data Products, in: AGU Fall Meeting Abstracts, 2003.

King, J. H. and Papitashvili, N. E.: Solar wind spatial scales in and comparisons of

hourly Wind and ACE plasma and magnetic field data, Journal of Geophysical Research: Space Physics, doi:10.1029/2004JA010649, 2005.

Kinrade, J.: Ionospheric Imaging and Scintillation Monitoring in the Antarctic and Arctic, Ph.D. thesis, University of Bath, 2013.

Kinrade, J., Mitchell, C. N., Yin, P., Smith, N., Maxfield, M. J., Rose, D. J., Bust, M. C., S., G., and Weatherwax, A. T.: Ionospheric scintillation over Antractica during the storm of 5-6 April 2010, Journal of Geophysical Research, 117, 2012.

Kumar, S., Tan, E. L., and Murti, D. S.: Impacts of solar activity on performance of the IRI-2012 model predictions from low to mid latitudes, Earth, Planets and Space, 67, 1–17, 2015.

Kunitsyn, V. and Tereshchenko, E.: Ionospheric Tomography, Physics of Earth and Space environment, Springer-Verlag, Berlin, 2003.

Leandro, R. and Santos, M.: A neural network approach for regional vertical total electron content modelling, Studia Geophysica et Geodaetica, 51, 279–292, 2007.

Liu, Z., Skone, S., Gao, Y., and Komjathy, A.: Ionospheric modeling using GPS data, GPS Solutions, 9, 63–66, 2005.

Loewe, C. A. and Prölss, G. W.: Classification and mean behavior of magnetic storms, Journal of Geophysical Research: Space Physics, 102, 14 209–14 213, 1997.

Lopez, R., Wiltberger, M., Hernandez, S., and Lyon, J.: Solar wind density control of energy transfer to the magnetosphere, Geophysical research letters, 31, 2004.

Mannucci, A., Iijima, B., Lindqwister, U., Pi, X., Sparks, L., and Wilson, B.: GPS and Ionosphere : Revised edition to URSI reviews of Radio Science, 1999.

Mannucci, A., Tsurutani, B., Iijima, B., Komjathy, A., Saito, A., Gonzalez, W., Guarnieri, F., Kozyra, J., and Skoug, R.: Dayside global ionospheric response

to the major interplanetary events of October 29–30, 2003 “Halloween Storms”, Geophysical Research Letters, 32, 2005.

Maruyama, T.: Regional reference total electron content model over Japan based on neural network mapping techniques, Annales Geophysicae, 25, 2609–2614, 2008.

Materassi, M. and Mitchell, C. N.: Imaging of the equatorial ionosphere, Annals of Geophysics, 48, 477–482, 2005.

McKinnell, L.-A. and Poole, A. W.: Predicting the ionospheric F layer using neural networks, Journal of Geophysical Research: Space Physics, 109, A08 308, 2004.

McNamara, L.: The ionosphere: communications, surveillance, and direction finding, Orbit, a foundation series, Krieger Pub. Co., 1991.

Meggs, R. W., Mitchell, C. N., and Howells, V.: Simultaneous observations of the main trough using GPS imaging and the EISCAT radar, Annales Geophysicae, 23, 753–757, 2005.

Mendillo, M., Baumgardner, J., Pi, X., Sultan, P. J., and Tsunoda, R.: Onset conditions for equatorial spread F, Journal of Geophysical Research: Space Physics, 97, doi:10.1029/92JA00647, 1992.

Mendillo, M., Meriwether, J. W., and a Biondi, M.: Testing the thermospheric neutral wind suppression mechanism for day-to-day variability of equatorial spread F, Journal of Geophysical Research, 106, 3655–3663, doi:10.1029/2000JA000148, 2001.

Misra, P. and Enge, P.: Global positioning system: signals, measurements, and performance, Ganga-Jamuna Press, Massachusetts, 2006.

Mitchell, C. N. and Spencer, P. S. J.: A three-dimensional time-dependent algorithm for ionospheric imaging using GPS, Annals of Geophysics, 46, 687–696, 2003.

Moeketsi, D. M.: Solar cycle effects on GNSS-derived ionospheric total electron content observed over southern Africa, Ph.D. thesis, Rhodes University, 2008.

Moldwin, M.: An introduction to space weather, Cambridge University Press, 2008.

Muella, M. T. A. H., de Paula, E. R., Fagundes, P. R., Bittencourt, J. A., and Sahai, Y.: Thermospheric Meridional Wind Control on Equatorial Scintillations and the Role of the Evening F-Region Height Rise, E × B Drift Velocities and F2-Peak Density Gradients, Surveys in Geophysics, 31, 509–530, doi:10.1007/s10712-010-9101-3, 2010.

Muella, M. T. A. H., de Paula, E. R., Mitchell, C. N., Kintner, P. M., Paes, R. R., and Batista, I. S.: Tomographic imaging of the equatorial and low-latitude ionosphere over central-eastern Brazil, Earth Planets and Space, 63, 129–138, 2011.

Mungufeni, P., Jurua, E., Bosco Habarulema, J., and Anguma Katrini, S.: Modelling the probability of ionospheric irregularity occurrence over African low latitude region, Journal of Atmospheric and Solar-Terrestrial Physics, 128, doi:10.1016/j.jastp.2015.03.010, 2015.

Mungufeni, P., Habarulema, J. B., and Jurua, E.: Trends of ionospheric irregularities over African low latitude region during quiet geomagnetic conditions, Journal of Atmospheric and Solar-Terrestrial Physics, 138-139, doi:10.1016/j.jastp.2016.01.015, 2016.

Muslim, B., Haralambous, H., Oikonomou, C., and Anggarani, S.: Evaluation of a global model of ionospheric slab thickness for foF2 estimation during geomagnetic storm, Annals of Geophysics, 58, A0551, 2015.

Na, H. and Lee, H.: Resolution analysis of tomographic reconstruction of electron density profiles in the ionosphere, International Journal of Imaging Systems and Technology, 2, 209–218, 1990.

NAVSTARGPS: NAVSTARGPS , Navigation Signal Timing and Ranging (NAVSTAR) GPS user eqipment introduction (Public Release Version), URL http://www.navcen.uscg.gov/pubs/gps/gpsuser/gpsuser.pdf, 1996.

Ngwira, C.: An analysis of ionospheric response to geomagnetic disturbances over South Africa and Antarctica., Ph.D. thesis, Rhodes University, 2012.

Ngwira, C. M., Klenzing, J., Olwendo, J., D'Ujanga, F. M., Stoneback, R., Baki, P., Seemala, G. K., and Bosco Habarulema, J.: A study of intense ionospheric scintillation observed during a quiet day in the East African low-latitude region, Radio Science, 48, doi:10.1002/rds.20045, 2013a.

Ngwira, C. M., Seemala, G. K., and Bosco Habarulema, J.: Simultaneous observations of ionospheric irregularities in the African low-latitude region, Journal of Atmospheric and Solar-Terrestrial Physics, doi:10.1016/j.jastp.2013.02.014, 2013b.

Nishioka, M., a. Saito, and Tsugawa, T.: Occurrence characteristics of plasma bubble derived from global ground-based GPS receiver networks, Journal of Geophysical Research: Space Physics, 113, 1–12, doi:10.1029/2007JA012605, 2008.

Okoh, D., Owolabi, O., Ekechukwu, C., Folarin, O., Arhiwo, G., Agbo, J., Bolaji, S., and Rabiu, B.: A regional GNSS-VTEC model over Nigeria using neural networks: A novel approach, Geodesy and Geodynamics, 7, 19–31, 2016.

Olwendo, O. J., Baluku, T., Baki, P., Cilliers, P. J., Mito, C., and Doherty, P.: Low latitude ionospheric scintillation and zonal irregularity drifts observed with GPS-SCINDA system and closely spaced VHF receivers in Kenya, Advances in Space Research, doi:10.1016/j.asr.2012.12.017, 2013.

Ondoh, T. and Marubashi, K.: Science of space environment, IOS Press, 2001.

Oyeyemi, E. O., McKinnell, L., and Poole, A.: Near-real time foF2 predictions

using neural networks, Journal of Atmospheric and Solar-Terrestrial Physics, 68, 1807–1818, 2006.

Panda, S., Gedam, S., and Rajaram, G.: Study of Ionospheric TEC from GPS observations and comparisons with IRI and SPIM model predictions in the low latitude anomaly Indian subcontinental region, Advances in Space Research, 55, 1948–1964, 2015.

Panicciari, T., Smith, N., Mitchell, C., Da Dalt, F., and Spencer, P.: Using sparse regularization for multi-resolution tomography of the ionosphere, Nonlinear Processes in Geophysics, 2015.

Parkinson, B. and Spilker, J.: Global Positioning System: Theory and Applications (volume One), Progress in astronautics and aeronautics, American Institute of Aeronautics and Astronautics, Inc., The University of Michigan, 5 edn., 1996.

Paxton, J. L., Christensen, A. B., Humm, D. C., Ogorzalek, B. B., Pardoe, C. T., Morrison, D., Weiss, M. B., Crain, W., Lew, P. H., Mabry, D. J., Goldsten, J. O.,Gary, S. A., Persons, D. F., Harold, M. J., Alvarez, E. B., Ercol, C. J., Strickl, D. J., and Meng, C. I.: Global ultraviolet imager (GUVI): measuring composition and energy inputs for the NASA Thermosphere Ionosphere Mesosphere Energetics and Dynamics (TIMED) mission, vol. 3756, pp. 3756 – 3756, 1999.

Paznukhov, V. V., Carrano, C. S., Doherty, P. H., Groves, K. M., Caton, R. G., Valladares, C. E., Seemala, G. K., Bridgwood, C. T., Adeniyi, J., Amaeshi, L. L. N., Damtie, B., D'Ujanga Mutonyi, F., Ndeda, J. O. H., Baki, P., Obrou, O. K., Okere, B., and Tsidu, G. M.: Equatorial plasma bubbles and L-band scintillations in Africa during solar minimum, Annales Geophysicae, 30, 675–682, doi:10.5194/angeo-30-675-2012, 2012.

Phiri, T.-J.: Correlation between SQUID and fluxgate magnetometer data for geomagnetic storms, Master's thesis, Stellenbosch: Stellenbosch University, 2013.

Pi, X., Mannucci, a. J., Lindqwister, U. J., and Ho, C. M.: Monitoring of global ionospheric irregularities using the Worldwide GPS Network, Geophysical Research Letters, 24, 2283, doi:10.1029/97GL02273, 1997.

Poole, A. W. and McKinnell, L.-A.: On the predictability of foF2 using neural networks, Radio Science, 35, 225–234, 2000.

Portillo, Herraiz, M., Radicella, S. M., and Ciraolo, L.: Equatorial plasma bubbles studied using African slant total electron content observations, Journal of Atmospheric and Solar-Terrestrial Physics, 70, 907–917, doi:10.1016/j.jastp.2007.05.019, 2008.

Prolss, G. W.: Physics of the Earth's Space Environment: An Introduction, Springer Berlin Heidelberg, Berlin, Heidelberg, 2004.

Rajesh, P. K., Lin, C. H., Chen, C. H., Lin, J. T., Matsuo, T., Chou, M. Y., Chen, W. H., Chang, M. T., and You, C. F.: Equatorial plasma bubble generation/inhibition during 2015 St. Patrick's Day storm, Space Weather, doi:10.1002/2017SW001641, 2017.

Rastogi, R. G.: Magnetic storm effects at equatorial electrojet stations, Earth, Planets and Space, 58, 645–657, 2006.

Rastogi, R. G. and Klobuchar, J. A.: Ionospheric electron content within the equatorial F2 layer anomaly belt, J. Geophys. Res., 95, 19 045, doi:10.1029/JA095iA11p19045, 1990.

Ratnam, D. V., Dinesh, B. V., Tejaswi, B., Kumar, D. P., Ritesh, T., Brahmanadam, P., and Vindhya, G.: TEC prediction model using neural networks over a low

latitude GPS station, International Journal of Soft Computing and Engineering (IJDCE), 2, 517–521, 2012.

Ray, S., Paul, A., and DasGupta, A.: Equatorial scintillations in relation to the development of ionization anomaly, in: Annales Geophysicae, vol. 24, pp. 1429–1442, Copernicus GmbH, 2006.

Raymund, T.: Ionospheric tomography algorithms, International Journal of Imaging Systems and Technology, 5, 75–85, 1994.

Rezende, L. F. C. D., de, P. E. R., Staciarini, B. I., Jelinek, K. I., and Rezende, M. M. T. d. A. H.: Study of ionospheric irregularities during intense magnetic storms, Revista Brasileira de GeofÃsica, 25, 151–158, 2007.

Richardson, I., Cliver, E., and Cane, H.: Sources of geomagnetic activity over the solar cycle: Relative importance of coronal mass ejections, high-speed streams, and slow solar wind, Journal of Geophysical Research: Space Physics, 105, 18 203–18 213, 2000.

Richardson, I. G., Cliver, E. W., and Cane, H. V.: Sources of geomagnetic storms for solar minimum and maximum conditions during 1972–2000, Geophysical Research Letters, 28, 2001.

Richmond, B. G. and Jungers, W. L.: Size variation and sexual dimorphism in Australopithecus afarensis and living hominoids, Journal of Human Evolution, 29, 229–245, 1995.

Rishbeth, H. and Garriott, O.: Introduction to ionospheric physics, vol. 14 of *International geophysics series*, Academic Press, New York, 1969.

Rishbeth, H. and Hanson, W.: A comment on plasma 'pile-up'in the F-region, Journal of Atmospheric and Terrestrial Physics, 36, 703–706, 1974.

Rishbeth, H. and Müller-Wodarg, I.: Why is there more ionosphere in January than in July? The annual asymmetry in the F2-layer, in: Annales Geophysicae, vol. 24, pp. 3293–3311, 2006.

Robbrecht, E., Berghmans, D., and Van der Linden, R. A. M.: Automated LASCO CME Catalog for Solar Cycle 23: Are CMEs Scale Invariant?, apj, 691, 1222–1234, doi:10.1088/0004-637X, 2009.

Rose, J.: Ionospheric Imaging to Improve GPS Timing, Ph.D. thesis, University of Bath, 2011.

Rosenqvist, L., Opgenoorth, H., Buchert, S., McCrea, I., Amm, O., and Lathuillere, C.: Extreme solar-terrestrial events of October 2003: High-latitude and Cluster observations of the large geomagnetic disturbances on 30 October, Journal of Geophysical Research: Space Physics, 110, 2005.

Sardón, E. and Zarraoa, N.: Estimation of total electron content using GPS data: How stable are the differential satellite and receiver instrumental biases?, Radio Science, 32, 1899–1910, doi:10.1029/97RS01457, 1997.

Schaer, S., Gurtner, W., and Feltens, J.: IONEX: The ionosphere map exchange format version 1, in: Proceedings of the IGS AC workshop, Darmstadt, Germany, vol. 9, 1998.

Seba, E. B. and Nigussie, M.: Investigating the effect of geomagnetic storm and equatorial electrojet on equatorial ionospheric irregularity over East African sector, Advances in Space Research, 58, doi:10.1016/j.asr.2016.06.037, 2016.

Seemala, G. K. and Valladares, C. E.: Statistics of total electron content depletions observed over the South American continent for the year 2008, Radio Science, 46, 2011.

Selcher, C.: Three-dimensional, High Resolution, Computerized Ionospheric Tomographic Imaging and Computational Modeling of an Artificial Ionospheric Cavity, West Virginia University, 2007.

Sibanda, P.: Challenges in Topside Ionospheric Modelling Over South Africa, Ph.D. thesis, Rhodes University, 2010.

Spencer, P. S. J. and Mitchell, C. N.: Imaging of fast moving electron-density structures in the polar cap, Annals of Geophysics, 50, 427–434, 2007.

Ssessanga, N.: Development of an ionospheric map for Africa., Ph.D. thesis, Rhodes University, 2014.

Ssessanga, N., Mckinnell, L.-a., and Habarulema, J. B.: Introduction of new data into the South African Ionospheric Map to improve the estimation of F2 layer parameters, doi:10.4401/ag-6704, 2015.

Stone, E. C., Frandsen, A., Mewaldt, R., Christian, E., Margolies, D., Ormes, J., and Snow, F.: The advanced composition explorer, Space Science Reviews, 86, 1–22, 1998.

Stoneback, R. A., Heelis, R. A., Burrell, A. G., Coley, W. R., Fejer, B. G., and Pacheco, E.: Observations of quiet time vertical ion drift in the equatorial ionosphere during the solar minimum period of 2009, Journal of Geophysical Research: Space Physics, 116, doi:10.1029/2011JA016712, 2011.

Stoneback, R. A., Davidson, R. L., and Heelis, R. A.: Ion drift meter calibration and photoemission correction for the C/NOFS satellite, Journal of Geophysical Research: Space Physics, 117, doi:10.1029/2012JA017636, 2012.

Sugiura, M. and Wilson, C. R.: Oscillation of the geomagnetic field lines and associated magnetic perturbations at conjugate points, Journal of Geophysical Research,

69, 1211–1216, 1964.

Tanna, H., Karia, S., and Pathak, K.: A study of L band scintillations during the initial phase of rising solar activity at an Indian low latitude station, Advances in Space Research, 52, 412–421, 2013.

Tarpley, J.: The ionospheric wind dynamo—I: Lunar tide, Planetary and Space Science, 18, 1075–1090, 1970.

Tesema, F., Damtie, B., and Nigussie, M.: The response of the ionosphere to intense geomagnetic storms in 2012 using GPS-TEC data from East Africa longitudinal sector, Journal of Atmospheric and Solar-Terrestrial Physics, doi:10.1016/j.jastp.2015.10.021, 2015.

Tsunoda, R. T.: On seeding equatorial spread F during solstices, Geophysical Research Letters, 37, doi:10.1029/2010GL042576, 2010.

Tsurutani, B., Echer, E., Shibata, K., Verkhoglyadova, O., Mannucci, A., Gonzalez, W., Kozyra, J., and Pätzold, M.: The interplanetary causes of geomagnetic activity during the 7-17 March 2012 interval: A CAWSES II overview, Journal of Space Weather and Space Climate, 4, doi:10.1051/swsc, 2014.

Tulunay, E., Senalp, E. T., Cander, L. R., Tulunay, Y. K., Bilge, A. H., Mizrahi, E., Kouris, S. S., and Jakowski, N.: Development of algorithms and software for forecasting, nowcasting and variability of TEC, Annals of Geophysics, 47, 1201–1214, 2004.

Uwamahoro, J. C. and Habarulema, J. B.: Modelling total electron content during geomagnetic storm conditions using empirical orthogonal functions and neural networks, Journal of Geophysical Research: Space Physics, 120, 11 000 –11 012, 2015.

Uwamahoro, J. C., Giday, N. M., Habarulema, J. B., and Katamzi-Joseph, Z. T.: Reconstruction of storm-time total electron content using ionospheric tomography and artificial neural networks; A comparative study over the African region., Radio Science, under review, 2017.

Venkatesh, K., Fagundes, P. R., Prasad, D. S. V. V. D., Denardini, C. M., de Abreu, A. J., de Jesus, R., and Gende, M.: Day-to-day variability of EEJ and its role on EIA over the Indian and Brazilian sectors, Jgr, pp. 1–14, doi: 10.1002/2014JA020649, 2015.

Wanliss, J.: When is it alright to use SYM-H as a storm index?, AGU Fall Meeting Abstracts, 2007.

Watthanasangmechai, K., Supnithi, P., Lerkvaranyu, S., Tsugawa, T., Nagatsuma, T., and Maruyama, T.: TEC prediction with neural network for equatorial latitude station in Thailand, Earth, Planets and Space, 64, 473–483, 2012.

Willmott, C. J. and Matsuura, K.: Advantages of the mean absolute error (MAE) over the root mean square error (RMSE) in assessing average model performance, Climate research, 30, 79–82, 2005.

Yamazaki, Y. and Kosch, M. J.: Journal of Geophysical Research : Space Physics The equatorial electrojet during geomagnetic storms and substorms, pp. 2276–2287, doi:10.1002/2014JA020773.Abstract, 2015.

Yao, Y. B., Chen, P., Zhang, S., and Chen, J. J.: Temporal and spatial variations in ionospheric electron density profiles over South Africa during strong magnetic storms, Natural Hazards and Earth System Sciences, 13, 375–384, 2013.

Yeh, K. and Raymund, T.: Limitations of ionospheric imaging by tomography, Radio Science, 26, 1361–1380, 1991.

Yin, P., Mitchell, C., Spencer, P., and Foster, J.: Ionospheric electron concentration imaging using GPS over the USA during the storm of July 2000, Geophysical Research Letters, 31, L12 806, 2004.

Yin, P., Zheng, Y.-N., Mitchell, C. N., and Li, B.: A multiresolution inversion for imaging the ionosphere, Journal of Geophysical Research: Space Physics, doi: 10.1002/2016JA023728, 2017.

Yizengaw, E.: Imaging the ionosphere, Ph.D. thesis, La Trobe University, 2004.

Yizengaw, E. and Moldwin, M. B.: African meridian b-field education and research (amber) array, Earth, Moon and Planets, 104, 237–246, doi:10.1007/s11038-008-9287-2, 2009.

Yizengaw, E., Retterer, J., Pacheco, E. E., Roddy, P., Groves, K., Caton, R., and Baki, P.: Postmidnight bubbles and scintillations in the quiet-time June solstice, 40, 1–6, doi:10.1002/2013GL058307, 2013.

Zapfe, B. D., Materassi, M., Mitchell, C. N., and Spalla, P.: Imaging of the equatorial ionospheric anomaly over South America - A simulation study of total electron content, Journal of Atmospheric and Solar-Terrestrial Physics, 68, 1819–1833, 2006.

Zhang, Y., Paxton, L. J., Morrison, D., Wolven, B., Kil, H., Meng, C.-I., Mende, S. B., and Immel, T. J.: O/N2 changes during 1–4 October 2002 storms: IMAGE SI-13 and TIMED/GUVI observations, Journal of Geophysical Research: Space Physics, doi:10.1029/2004JA010441, 2004.

Zheng, D., Hu, W., and Nie, W.: Multiscale ionospheric tomography, GPS Solutions, doi:10.1007/s10291-014-0418-0, 2015.

Zolesi, B. and Cander, L. R.: Ionospheric prediction and forecasting, Springer, 2014.

Zou, Y. and Wang, D.: A study of GPS ionospheric scintillations observed at Guilin, Journal of Atmospheric and Solar-Terrestrial Physics, 71, 1948–1958, 2009.